

ESTABLISHING GOVERNING EQUATIONS FOR 3D  
CELL CULTURE IN PERFUSION BIOREACTORS

By

JAGDEEP THIRIBHUVAN PODICHETTY

Bachelor of Technology in Chemical Engineering  
Jawaharlal Nehru Technological University  
Anantapur, Andhra Pradesh, India  
2009

Master of Science in Chemical Engineering  
Oklahoma State University  
Stillwater, Oklahoma  
2011

Submitted to the Faculty of the  
Graduate College of the  
Oklahoma State University  
in partial fulfillment of  
the requirements for  
the Degree of  
DOCTOR OF PHILOSOPHY  
May, 2014

ESTABLISHING GOVERNING EQUATIONS FOR 3D  
CELL CULTURE IN PERFUSION BIOREACTORS

Dissertation Approved:

Dr. Sundar Madihally

---

Dissertation Adviser

Dr. AJ Johannes

---

Dr. Gary Foutch

---

Dr. Hasan Atiyeh

---

## ACKNOWLEDGEMENTS

It's my pleasure to thank each and every one who helped make this dissertation possible. I would like to express my deepest gratitude to my family for their love and support throughout my life. I would like to thank my advisor Dr. Sundar Madihally for his guidance and support throughout my research, studies and time at Oklahoma State University. His passion and enthusiasm for research has been a great motivator, he has been a good mentor and role-model. I really appreciate his time and effort in reviewing and providing input to not only improve this dissertation but countless other manuscripts and abstracts.

Additionally, I would like to extend my thanks to my colleagues Jimmy Walker, Abdu Kalf, Kumar Singarapu, Christian Tormos, Swapneel Deshpande, Carrie German, Kevin Roehm, Leigh Krause, Lukasz Witek, and Yang Shi for their direct and indirect help with this research and reviewing the many versions of this dissertation. Thanks to my committee members, Dr. AJ Johannes, Dr. Gary Foutch and Dr. Hasan Atiyeh for their guidance, assistance, and feedback. I would like to thank my friends for the wonderful graduate school experience. Lastly, I would like to thank Oklahoma State University and the School of Chemical Engineering for providing a great learning opportunity.

Name: JAGDEEP PODICHETTY THIRIBHUVAN

Date of Degree: MAY, 2014

Title of Study: ESTABLISHING GOVERNING EQUATIONS FOR 3D CELL CULTURE IN  
PERFUSION BIOREACTORS

Major Field: CHEMICAL ENGINEERING

Abstract: Culturing cells and regenerating tissues *in vitro* on 3D scaffolds involves several challenges, such as efficient nutrient transportation, uniform stress distribution, and the removal of wastes. Bioreactors not only allow reproducibility but also provide a controlled environment for production of tissues. The objective of this study was to establish fundamental governing equations for the design of tissue engineering bioreactors and scaffolds. The governing equations related to nutrient permeability, mechanical and structural properties of the scaffolds, as well as nutrient consumption kinetics were tested. Large scaffolds with a high aspect ratio were utilized so that the obtained experimental measurements have high signal-to-noise ratio. This allowed the validation of the governing equations used in the computational models with high fidelity. Three different scaffold preparation techniques, freeze drying, salt leaching, and electrospinning were used to fabricate scaffolds with different microarchitecture. Chitosan, gelatin, and polycaprolactone polymers were used to prepare scaffolds. Two types of bioreactor configurations, flow-through and axial-flow, were used in this study. Both were designed to hold same sized scaffolds, but differ in flow configuration, which made them suitable for evaluating and validating the equations. Bioreactors of appropriate flow configuration were constructed in-house for experimental analysis. Computational Fluid Dynamics (CFD) simulations were performed to predict pressure drop, shear stress, deformation, nutrient distribution profile and exit concentration at various operating conditions. Additionally, non-ideal distribution models such as segregation and dispersion were combined with residence time distribution to predict the exit concentration. The model predictions were validated using an experimental setup with metabolically active liver cells. The results show that the scaffold permeability can be calculated using scaffold pore characteristics and deformation could be predicted using simulation. The axial-flow bioreactor performed better than flow-through bioreactor with superior nutrient distribution, lower shear stress, and deformation. Comparison of the outlet oxygen concentrations between the simulation and experimental results showed good agreement with the dispersion model. However, outlet oxygen concentrations from segregation model were lower. These insights help monitor *in vitro* tissue regeneration, understand the effect of mechanical stimulus on 3D cell culture, and improve quality of the regenerated tissue.

## TABLE OF CONTENTS

Chapter	Page
1. INTRODUCTION .....	1
Aim1: To model porous scaffold deformation induced by medium perfusion.....	3
Aim 2: To modeling pressure drop using generalized scaffold characteristics in an axial-flow bioreactor for soft tissue regeneration. ....	4
Aim 3: To evaluate nutrient consumption profile and validate consumption predictions with cell culture experiments .....	5
Summary .....	6
2. BACKGROUND .....	7
2.1 The field of tissue engineering.....	7
2.2 Biomaterials and bioscaffolds.....	8
2.2.1 Scaffold preparation techniques.....	11
2.2.2 Biomaterial and scaffold properties .....	12
2.3 Bioreactors in tissue engineering.....	15
2.4 Flow through porous media .....	20
2.5 Nutrient consumption in porous media.....	22
2.6 Non-ideal fluid distribution models for predicting exit concentration .....	23
2.7 Computational fluid dynamics in bioreactor design .....	26
2.8 Three-dimensional cell culture in perfusion bioreactors .....	26
3. MODELING MEDIA INDUCED POROUS SCAFFOLD DEFORMATION.....	29
3.1 Introduction.....	29
3.2 Materials and methods .....	31
3.2.1 Sources of materials.....	31
3.2.2 Preparation of porous scaffolds. ....	31
3.2.3 Estimation of pore size and porosity of scaffolds.....	32
3.2.4. Estimation of elastic modulus and Poisson ratio .....	32
3.2.5. Pressure drop measurement .....	34
3.3. Computational modeling.....	35
3.4. Results and discussion .....	41
3.4.1 Scaffold characterization .....	41

Chapter	Page
3.4.2. Poisson's ratio measurement.....	42
3.4.3. Darcy to Brinkman transition in the flow-through bioreactor .....	43
3.4.4. Validation of permeability equation .....	44
3.4.5. Validation of fluid flow-structural mechanics coupling approach .....	47
3.4.6. Effect of scaffold deformation on shear stress.....	50
3.4.7. Effect of permeability on pressure drop and deformation. ....	52
3.4.8. Effect of scaffold mechanical properties on structural deformation.....	54
3.5 Acknowledgements.....	56
<b>4. MODELING PRESSURE DROP IN AXIAL-FLOW BIOREACTOR FOR SOFT TISSUE ENGINEERING.....</b>	<b>57</b>
4.1 Introduction.....	57
4.2. Materials and methods .....	58
4.2.1 Preparation of porous scaffolds .....	58
4.2.2 Evaluation of mechanical properties.....	60
4.2.3 Estimation of scaffold permeability.....	60
4.2.4 Pressure drop measurement .....	62
4.3. Computational fluid dynamics modeling.....	63
4.4. Results.....	66
4.4.1 Scaffold characterization .....	66
4.4.2 Mechanical Properties of Scaffolds .....	68
4.4.3 Validation of permeability equation .....	68
4.4.4 Effect of axial-flow configuration on shear stress and pressure drop.....	70
4.4.5. Analysis of scaffold deformation.....	73
4.4.6 Effect of permeability on pressure drop.....	74
4.4.7 Effect of scaffold mechanical properties on pressure drop and scaffold deformation .....	75
4.5 Discussion.....	78
4.6 Acknowledgements.....	80
<b>5. RESIDENCE TIME DISTRIBUTION ANALYSIS AND EVALUATION OF EXIT CONCENTRATION IN AXIAL-FLOW BIOREACTOR.....</b>	<b>81</b>
5.1 Introduction.....	81
5.2 Materials and methods .....	82
5.2.1 Preparation of porous scaffolds .....	82
5.2.2 Obtaining RTD function using step-input of a tracer .....	83
5.2.3 Determining nutrient exit concentration using segregation and dispersion models .....	86

Chapter	Page
5.2.4 Determining nutrient concentration by HepG2 cell seeded scaffolds ....	88
5.3 CFD simulation of nutrient consumption .....	91
5.4. Results and discussion .....	93
5.4.1 Simulated fluid flow characteristics.....	93
5.4.2 Concentration profile of nutrients.....	95
5.4.3 Residence time distribution analysis.....	96
5.4.4 CFD exit nutrient concentration compared to Segregation Model. ....	99
5.4.5 Characterizing non-ideal fluid distribution using Dispersion Model ...	101
5.4.6 Exit nutrient concentration compared to experiments .....	102
5.4.7 Effect of varying cell density on concentration profile .....	104
5.5 Acknowledgements.....	106
6. CONCLUSION AND RECOMMENDATIONS .....	107
6.1 Conclusions.....	107
6.1.1 Modeling media induced porous scaffold deformation .....	107
6.1.2 Modeling pressure drop in axial-flow bioreactor.....	109
6.1.3 Residence time distribution analysis and evaluation of exit concentration .....	110
6.2 Recommendations.....	112
REFERENCES .....	115
APPENDIX A: Structural mechanics simulation using COMSOL MULTIPHYSICS version 4.2a .....	125
APPENDIX B: Pressure transducer calibration using MLA1052 pressure gauge and accessories.....	142
APPENDIX C: 16-730 O2 Microelectrodes calibration and operating instructions .	146

## LIST OF TABLES

Table	Page
1.1 Parameters and their applications in tissue engineering .....	3
2.1. Properties of biopolymers used in tissue engineering.....	13
2.2. Mechanical properties of human tissues .....	14
3.1 Density and Poisson's ratio of CG and PCL.....	34
3.2 Modeling data for CFD simulations .....	39
3.3 Reynolds number calculations in the porous scaffold .....	39
4.1 Scaffold pore characteristics and mechanical properties and modeling data .....	67
4.2 Reynolds number calculations in the porous scaffold .....	70
4.3 Comparison between flow-through and axial-flow bioreactor configurations .....	72
5.1. Rate constant of oxygen and glucose for hepatocytes with varying cell density..	92
5.2 Comparison of nutrient distribution by RTD at 15mL/min .....	98
5.3. Peclet number calculations in the porous scaffold.....	101



## LIST OF FIGURES

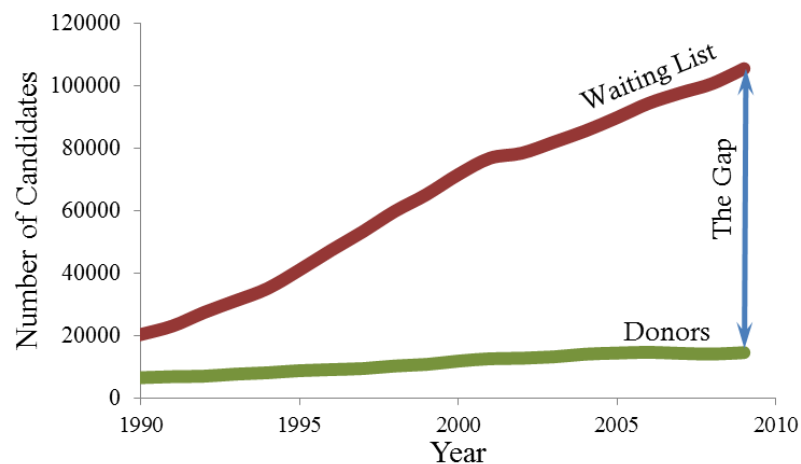
Figure	Page
1.1 The gap between organ donors and patients waiting to receive lifesaving transplants .....	1
2.1 <i>In vivo</i> and <i>in vitro</i> techniques in tissue engineering .....	7
2.2 Chemical structures of naturally derived chitosan and gelatin polymers .....	9
2.3 Chemical structures of synthetic polymers. ....	10
2.4 Scanning electron micrographs of scaffolds .....	12
2.5 Perfusion bioreactor systems used for 3D cell culture.....	16
2.6 Perfusion bioreactor designs .....	19
2.7 Schematic of a system with flow-through porous media.....	22
2.8. Perfusion bioreactor system with peristaltic pump from 3D Biotek LLC.....	28
3.1 Experimental setup used for determining Poisson’s ratio of scaffolds in hydrated condition .....	33
3.2 Modeling and bioreactor schematic .....	36
3.3 Macroscopic and microscopic appearance of scaffolds.....	42
3.4 Comparison of experimental pressure drop to simulated pressure drop across the flow-through bioreactor .....	46
3.5 Comparison of scaffold deformation profiles between experiment and simulation .....	49
3.6 Altered hydrodynamic shear stress (a-b) and pressure drop (c-d) profiles in CG scaffold due to deformation .....	50

Figure	Page
3.7 Effect of scaffold permeability and elastic modulus on pressure drop at various flow rates.....	53
3.8 Effect of Poisson’s ratio on pressure drop and deformation.....	55
4.1 Axial-flow bioreactor flow pattern .....	62
4.2 Micrographs of scaffold surfaces orthogonal to the flow direction.....	66
4.3 Pressure drop validation across the bioreactor.....	69
4.4 Hydrodynamic shear stress profile for PCL-CA scaffold at 25mL/min inlet flow rate.....	71
4.5 Pressure drop profile at 25mL/min flow rate across the scaffold thickness from the center.....	73
4.6 Deformation profile across the scaffold thickness from the center at 25mL/min inlet flow rate .....	74
4.7 Simulation results of pressure drop across the axial-flow bioreactor showing for various permeabilities and elastic moduli at various flow rate.....	77
5.1. Schematic of the flow system used to determine the residence time distribution the axial-flow bioreactor .....	84
5.2 Schematic of cell culture experimental setup with axial-flow bioreactor.....	90
5.3 Cross sectional profiles of the scaffold from the central axis showing .....	94
5.4 Oxygen concentration profiles across the scaffold thickness from the central symmetric axis with $1.2 \times 10^6$ cells/cm <sup>3</sup> .....	96
5.5. C(t)/C0 curve at different time steps at 15mL/min.....	97
5.6 Nutrient outlet concentration comparison.....	100
5.7. Micrograph showing HepG2 cells in the CG scaffolds .....	103
5.8 Effect of cell density on oxygen consumption in CG scaffold. ....	105

## CHAPTER 1

### INTRODUCTION

There are more than 100,000 patients currently waiting for a life-saving organ transplant. About 18 people die each day due to lack of organs available for transplant (OPTN 2012). **Figure 1.1** shows an increasing trend in number of patients waiting for a transplant compared to the number of donors available. An alternative is engineering three-dimensional (3D) tissues *in vitro* by seeding cells (autologous or allogeneic) within porous biodegradable scaffolds, which would act as template for tissue regeneration (Martin, Wendt et al. 2004; Chen and Hu 2006). Significant developments have occurred in preparation of biodegradable scaffolds and understanding of cell behavior in 3D environments.



**Figure 1.1** The gap between organ donors and patients waiting to receive lifesaving transplants. (OPTN 2012)

However, culturing cells on 3D scaffolds involves several challenges, such as efficient nutrient transportation, uniform stress distribution, and removal of wastes. Bioreactors allow a reproducible and controlled environment for production of tissues using 3D porous biodegradable scaffolds. Bioreactors also provide flexibility to manipulate the *in vitro* conditions such as fluid flow and application of mechanical shear stresses (Hidalgo-Bastida, Thirunavukkarasu et al. 2012). Many bioreactor configurations such as rotating wall, micro-gravity, and perfusion have been proposed and used at various flow rates using scaffolds i) to seed cells, ii) constantly replenish nutrients and iii) to provide physical forces required by the developing tissue (Huang, Onyeri et al. 2005; Martin and Vermette 2005). Flow bioreactors systems are more advantageous than static culture as they provide continuous nutrient nourishment and distribution (Vunjak-Novakovic, Obradovic et al. 1998; Bancroft, Sikavitsas et al. 2003; Cartmell, Porter et al. 2003). However, fundamental engineering aspects in tissue regeneration, such as nutrient permeability, structural integrity of scaffolds, and nutrient consumption models, must to be established. These are critical in designing bioreactors to improve quality of engineered tissues and generate complex organs, such as liver and kidney.

The objective of this study was to establish fundamental governing equations for design of tissue engineering bioreactors and scaffolds. The governing equations related to nutrient permeability, scaffold mechanical and structural properties, and nutrient consumption kinetics were tested. These relationships could potentially be used in monitoring cell growth and tissue regeneration as shown in the **Table 1.1**. Large scaffolds with high aspect ratio (0.2-cm thick and 10-cm diameter) were utilized so that the obtained experimental measurements have high signal to noise ratio (Lawrence, Devarapalli et al. 2009). This permits the validation of the governing equations used in the computational models with high dependability.

**Table 1.1** Parameters and their applications in tissue engineering

<b>Parameter</b>	<b>Application</b>
Deformation	Tissue Quality and Bioreactor Design
Pressure Drop	Tissue Growth
Oxygen Consumption	Cell Growth

Two bioreactor configurations flow-through and axial-flow were used in this study. These bioreactors were designed to hold same sized scaffold, but differ in flow configuration. This makes them suitable for evaluating and validating the equations. The flow-through configuration involves positioning the scaffold in the path of fluid flow with maximum resistance; hence, this configuration was appropriate for analyzing structural deformation in the scaffold. Further, the flow-through configuration was used to establish relationship between pressure drop, permeability, and structural and mechanical properties of the scaffold. In axial-flow configuration, effects of mechanical properties of scaffold and pressure drop are relatively lower in comparison to flow-through configuration and nutrient transport may depend on convection and diffusion. Therefore, axial-flow configuration was used to validate permeability equations and nutrient consumption kinetics. The strategy was to utilize an integrated approach of computational fluid dynamic modeling (CFD) and experimental analysis to accomplish these objectives. These were grouped into three specific aims:

**Aim 1: To model porous scaffold deformation induced by medium perfusion.**

The possibility of calculating permeability of porous scaffolds using pore size and shape was evaluated. The results were validated using experimental measured pressure drop and simulations performed with the inclusion of structural deformation due to medium perfusion. Polycaprolactone (PCL) and Chitosan-Gelatin (CG) scaffolds were prepared by salt leaching and freeze drying technique respectively. Scanning Electron Micrographs were assessed for pore characteristics and mechanical properties. Porosity for both scaffolds was nearly same but the permeability varied ten-

fold. Elastic moduli were 600kPa and 9.14kPa for PCL and CG scaffolds respectively, while Poisson's ratio was 0.3 for PCL scaffolds and  $\sim 1.0$  for CG scaffolds. A flow-through bioreactor accommodating a 10cm diameter and 0.2cm thick scaffold was used to determine the pressure-drop at various flow rates. Additionally, CFD simulations were performed by coupling fluid flow, described by Brinkman equation, with structural mechanics using a dynamic mesh. The experimentally obtained pressure drop matched the simulation results of PCL scaffolds. Simulations were extended to a broad range of permeabilities ( $10^{-10}\text{m}^2$  to  $10^{-14}\text{m}^2$ ), elastic moduli (0.01MPa to 100MPa) and Poisson's ratio (0.1 to 0.49). The results showed significant deviation in pressure drop due to scaffold deformation compared to the rigid scaffold at permeabilities near healthy tissues. Also, considering the scaffold as a non-rigid structure altered the shear stress profile. In summary, scaffold permeability can be calculated using scaffold pore characteristics and deformation could be predicted using CFD simulation.

**Aim 2: To modeling pressure drop using generalized scaffold characteristics in an axial-flow bioreactor for soft tissue regeneration.**

In this aim, fluid dynamics was analyzed in an axial-bioreactor that could accommodate a 10cm diameter 0.2cm thick scaffold and validated microarchitecture-based permeability equation via pressure drop measurements. Polycaprolactone–cellulose acetate (PCL-CA) co-axial electrospun randomly oriented fibrous scaffolds and CG scaffolds prepared using freeze drying techniques were utilized. Analyses of scaffolds via scanning electron microscopy indicated that fiber size in PCL-CA scaffolds was  $8.63(\pm 0.901)\mu\text{m}$  and the porosity was  $70(\pm 9)\%$  while CG scaffolds were  $85(\pm 4)\%$ . Scaffold mechanical properties in Phosphate Buffered Saline (PBS) maintained at  $37^\circ\text{C}$  indicated that the elastic modulus of PCL-CA scaffolds was 80kPa while CG scaffolds had 9kPa. Also, PCL-CA scaffolds had Poisson's ratio, 0.39 while CG had a higher than 1. Since electrospun scaffolds had fibrous architecture, the permeability of the scaffolds was calculated based on their fiber size. Axial-flow bioreactor accommodating a 10cm diameter 0.2cm thick scaffold was constructed in-house and

utilized to determine the pressure-drop at various flow rates using corresponding scaffolds. Additionally, CFD simulations were performed by coupling fluid flow, described by Brinkman equation, with structural mechanics using a moving mesh. The experimentally obtained pressure drop results agreed with simulation results for both PCL-CA and CG scaffolds at various flow rates. The CFD predictions were extended to a broad range of permeabilities ( $5 \times 10^{-10} \text{m}^2$  to  $1 \times 10^{-15} \text{m}^2$ ), elastic modulus (0.001MPa to 1GPa), and Poisson's ratio (0.1 to 0.49). Results showed increase in pressure drop with permeability. Scaffolds with higher elastic modulus performed better and the effect of Poisson's ratio was insignificant. In summary, scaffold permeabilities can be calculated using scaffold microarchitecture. These relationships could be used in monitoring tissue regeneration via pressure drop across a deformable porous scaffold.

**Aim 3: To evaluate nutrient consumption profile and validate consumption predictions with cell culture experiments.**

To obtain uniform nutrient distribution in an axial-flow bioreactor, growth medium entering the bioreactor from a small inlet has to be spread over a large area. This necessitates analyses of nutrient distribution coupled with consumption by the cells present within the porous scaffold. In this study, the distribution of oxygen and glucose were evaluated along with consumption by hepatocytes by three approaches using 100mm diameter and 2mm thick CG porous scaffolds prepared by freeze-drying: i) CFD simulation, ii) experimentally determined residence time distribution (RTD) coupled with segregation model, iii) Dispersion model, and iv) experimentally determined consumption by HepG2 cells. For the CFD simulation, Brinkman's equation was used to model flow-through porous medium, structural mechanics to determine fluid induced deformation of the scaffolds, and convection-diffusion equation coupled with Michaelis-Menten rate expression for nutrient consumption. Using CFD, axial-flow bioreactor was designed to operate with low hold-up volume while providing maximum nutrient distribution in the entire scaffold using flow rates up to 25 mL/min. In addition to CG scaffolds, hydrophobic PCL scaffolds prepared by salt leaching technique

were utilized for performing RTD analyses. The pore size, porosity, elastic modulus and Poisson's ratio values of scaffolds were characterized. With the assumption that each hepatocyte within the scaffold behaves like a small batch reactor, segregation model was combined with RTD to determine exit concentration. The dispersion model was also used to predict the exit concentrations. Experiments were also performed using HepG2 cells on CG scaffolds with a cell density of  $1.2 \times 10^{12}$  cells/m<sup>3</sup>. Oxygen probes at the inlet and outlet of the bioreactor provided oxygen consumption readings in real time. In addition, glucose in the spent growth medium was also analyzed. Comparisons of oxygen of the outlet oxygen concentrations between the simulation results, and experimental results showed good agreement with the dispersion model. Outlet oxygen concentrations from segregation model predictions were lower. Doubling the cell density showed a need for increasing the flow rate in CFD simulations. Measurement of cell volume to account for changes in scaffold porosity indicated that the contributions of cell volume towards porosity were negligible at the concentrations tested.

**Summary:** Culturing cells and regenerating tissues *in vitro* on 3D scaffolds involves several challenges, such as efficient nutrient transportation, uniform stress distribution, and removal of wastes. Bioreactors allow a reproducible and controlled environment for production of tissues using 3D porous biodegradable scaffolds. The fundamental governing equations from designing tissue engineering bioreactors were established. A model to simulate the tissue regeneration process, including fluid dynamics, scaffold deformation, and nutrient consumption, has been provided. This study can be used as a guideline for selection of scaffold, bioreactor design, and cell type in *in vitro* 3D cell culture and tissue regeneration. In addition, these insights can help monitoring *in vitro* tissue regeneration and understanding the effect of mechanical stimulus on 3D cell culture.

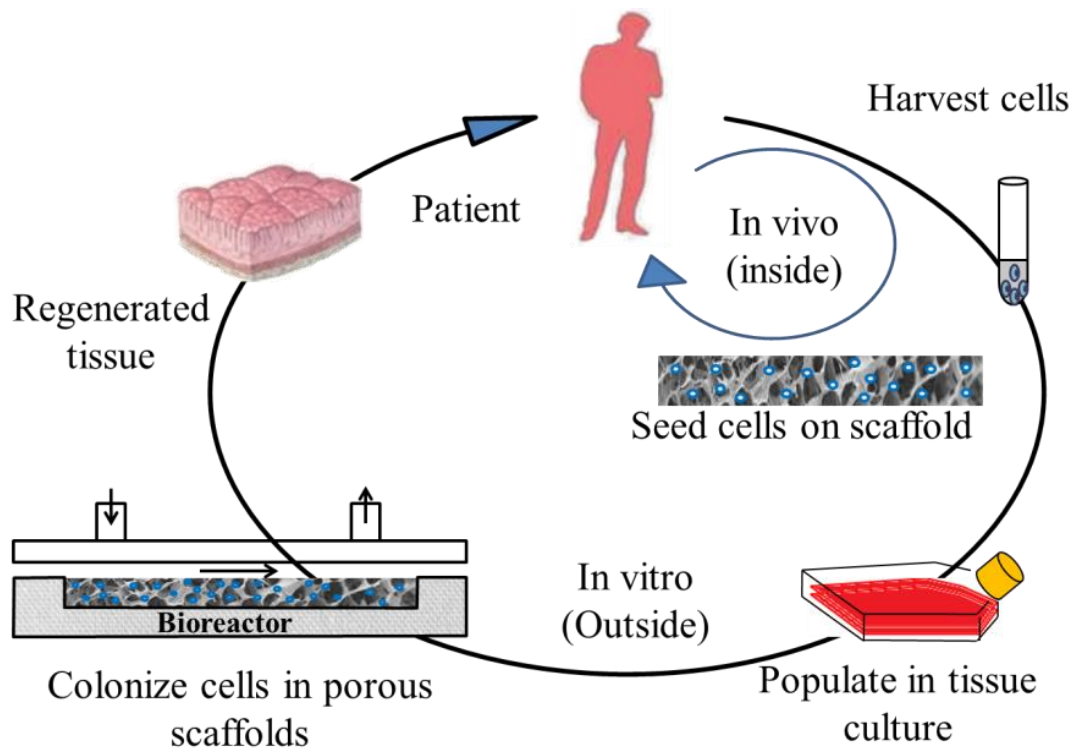


## CHAPTER 2

### BACKGROUND

#### 2.1 The field of tissue engineering

The study of tissue engineering involves replacing or repairing a damaged tissue, such as the bladder, liver, or skin using naturally or synthetic engineered biomaterials. **Figure 2.1** shows two approaches in tissue engineering, *in vivo* and *in vitro*.



**Figure 2.1** *In vivo* and *in vitro* techniques in tissue engineering.

The tissue engineering process can essentially be divided into three elements, sources of cells, scaffolds, and tissue regeneration processes. Cells are harvested from the patient or a donor and populated depending on the size of the tissue. The populated cells are seeded on biodegradable porous scaffolds, which provide support and structure for cell growth and extra cellular matrix production. The scaffold with seeded cells is either implanted back to the injured region (*in vivo*) or placed in a bioreactor for tissue growth (*in vitro*). During *in vivo*, the scaffold is introduced at the injured region in the patient's body to provide surrounding cells with a 3D environment to proliferate. The cells attach onto the scaffold, multiply and subsequently produce extracellular matrix (ECM). The *in vitro* tissue regeneration process involves use of a bioreactor system. The design of these bioreactor systems is critical as they must provide both biomechanical and biochemical controls, such as uniform nutrient and stress distribution, to mimic physiological environment.

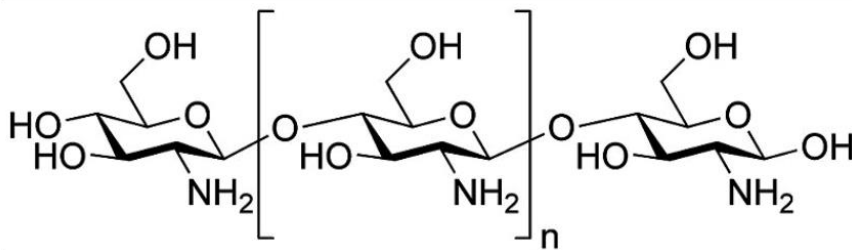
## **2.2 Biomaterials and bioscaffolds**

Varieties of natural and synthetic polymers have been utilized in tissue engineering applications. A scaffold should be biodegradable, biocompatible, mechanically strong, and be able to form a 3D structure of desired shape. The structural and mechanical properties of the scaffold mainly depend on the properties of the biomaterial and fabrication technique. Biomaterials can be broadly classified into inert or degradable materials. Inert materials, for example poly(methylmethacrylate), are used in medical device such as sutures and catheters (Wise 1995). Biodegradable materials, for example polycaprolactone, are commonly used for fabricating scaffold utilized in tissue engineering (Seal, Otero et al. 2001).

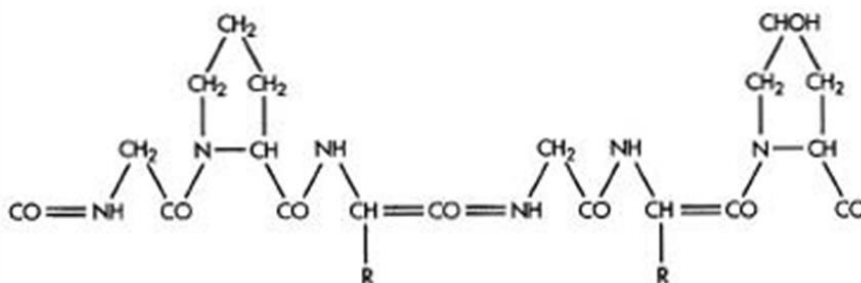
The polymers used for scaffold fabrication can be derived from natural sources or synthesized based on the application. Natural polymers such as chitosan and gelatin have shown potential for their use as bioscaffolds. Chitosan is derived from deacetylation of chitin, commonly found in

exoskeleton of crustaceans. Chitosan is biocompatible, available in a large quantity, and can be made available at low cost (Khor and Lim 2003). To improve the mechanical and biological properties of chitosan, it has been used in a blend with other polymers such as fibroin (Ruan, Lin et al. 2011) and gelatin (Pulieri, Chiono et al. 2008). This study used a chitosan-gelatin polymer for scaffold fabrication. Gelatin is a protein based polymer derived from collagen. It is biocompatible, biodegradable, and its chemical properties can be manipulated easily compared to typically used collagen, in addition it's relatively cheaper than collagen (Kuijpers, Engbers et al. 1999). The blending of chitosan and gelatin improves the biological activity by promoting cell adhesion and migration. **Figure 2.2** shows chemical structure of chitosan and gelatin polymers.

a) Chitosan



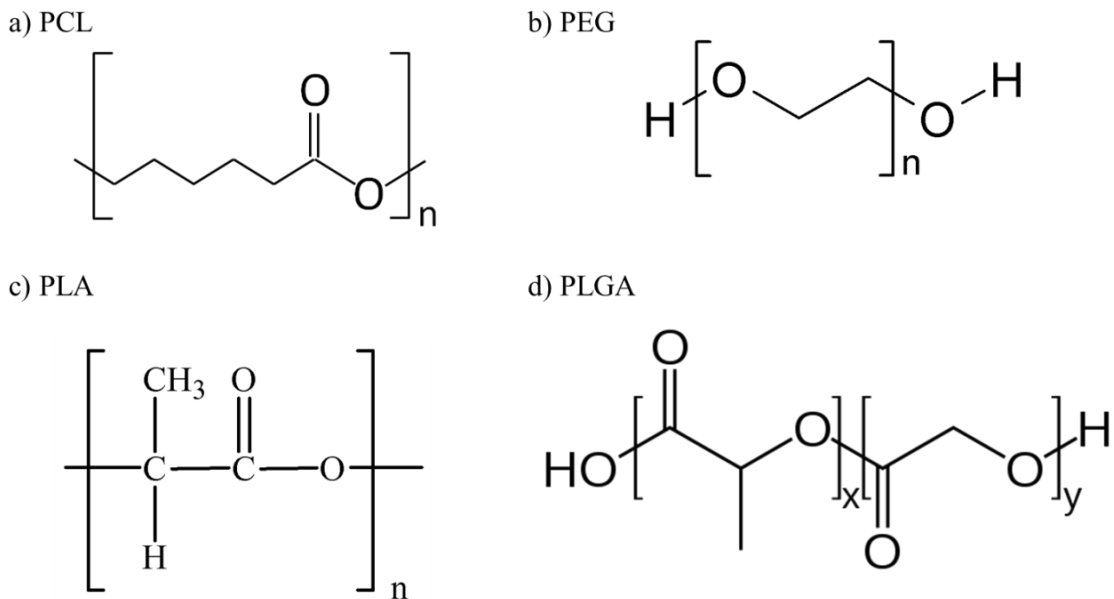
b) Gelatin



**Figure 2.2** Chemical structures of naturally derived chitosan and gelatin polymers (Mahapatro and Singh 2011; Chakraborty, Roy et al. 2012).

Synthetic polymers unlike natural polymers are more flexible, their mechanical and chemical properties can be altered as desired. Nontoxic synthetic polymers, such as polyethylene glycol

(PEG), poly (caprolactone) (PCL), poly (lactic acid) (PLA), and their copolymer such as poly(lactic-co-glycolic acid) (PLGA), are widely used for constructing scaffolds. **Figure 2.3** shows chemical structure of various synthetic polymers used in tissue engineering. However, chemical modifications, such as introduction of ester linking, are typically required to avoid any complication after implantation. Among synthetic polymers PCL is one of the most flexible and can be easily produced or combined with other polymers (Wiseman, Domb et al. 1998). It is non-toxic, non-inflammatory and has been approved by Food and Drug Administration (FDA). However, PCL has a low biodegradation rate. This limitation can be overcome by blending PCL with a water-soluble polymer such as poly(N-vinyl-2-pyrrolidone) to increase its degradation rate (Kim, Le et al. 2013). Scaffolds fabricated from PCL and its copolymers were also used in this study.

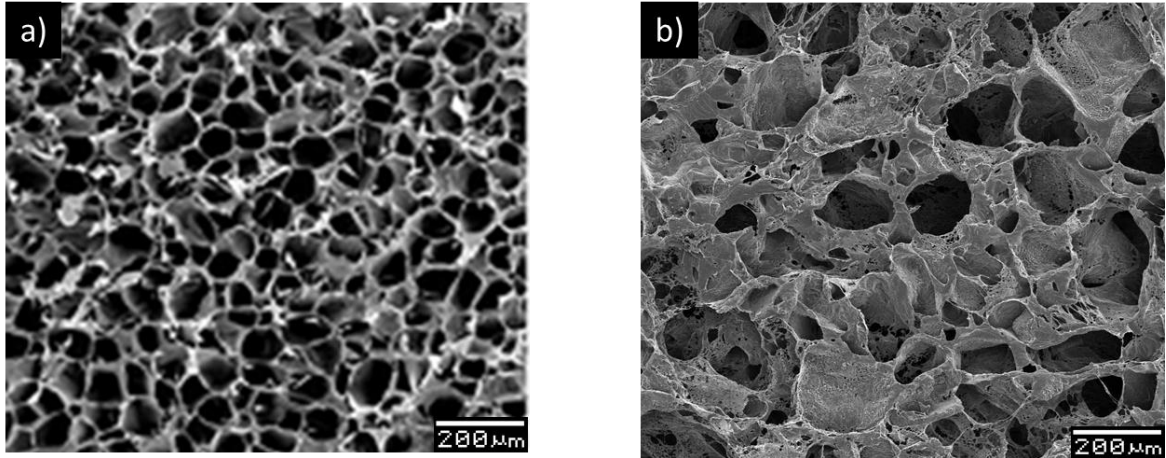


**Figure 2.3** Chemical structures of synthetic polymers a) PCL b) PEG c) PLA and copolymer d) PLGA (Taluja, Youn et al. 2007).

### 2.2.1 Scaffold preparation techniques

Scaffolds used in tissue engineering are fabricated using different techniques such as 3D printing, electrospinning, salt leaching, freeze drying, phase separation, gas foaming, and fiber extrusion (Whang, Thomas et al. 1995; Mooney, Baldwin et al. 1996; Schugens, Maquet et al. 1996; Park, Nam et al. 1997; Harris, Kim et al. 1998; Nam and Park 1999; Chen, Ushida et al. 2000; Han 2000; Chen, Ushida et al. 2001; Ma, Wang et al. 2001; Raghunath, Rollo et al. 2007; Salerno, Oliviero et al. 2007; Blan and Birla 2008). The scaffolds were fabricated using freeze drying, salt leaching and electrospinning methods. The freeze drying technique produces a continuous network of ice crystals surrounded by chitosan-gelatin fibers. The sublimation of ice crystals during the drying phase results in formation of a highly porous chitosan-gelatin scaffold. The pore structure of the scaffold mimics the ice crystal structure. Hence, the pore structure can be effectively controlled by altering solvents or manipulating the freezing process (Schoof, Apel et al. 2001; Haugh, Murphy et al. 2010). For example dissolving PLGA in benzene produces scaffolds with smaller pores compared to chloroform or freezing the solution at lower temperature of  $-196^{\circ}\text{C}$  showed similar effects (Moshfeghian, Tillman et al. 2006). **Figure 2.4a** show scanning electron micrograph (SEM) of a freeze dried scaffold. **Figure 2.4b** show scanning electron micrograph (SEM) of a salt leached scaffold. The salt leaching technique involves casting the polymer solution and salt in a mold, followed by drying the mixture and leaching out the salt with water to create pores (Chen, Ushida et al. 2002). The pore structure can be controlled by altering size of the salt crystals.

The electrospinning technique creates fiber meshes with individual fibers either woven or knitted into a 3D pattern of variable pore size (Chen, Ushida et al. 2002). Hence, the scaffold fabrication technique greatly influences the characteristics of the scaffold, one such characteristic is permeability which mainly depends on pore structure (Madhally 2010).



**Figure 2.4** Scanning electron micrographs of scaffolds prepared from a) freeze drying b) salt leaching techniques (Podichetty, Dhane et al. 2012).

### **2.2.2 Biomaterial and scaffold properties**

The structural and mechanical properties of the scaffolds have a significant effect on the tissue regeneration process. These properties mainly depend on the biomaterials used and the fabrication techniques. The scaffold should have sufficient mechanical strength to retain its structure during the tissue regeneration process. Natural polymers such as chitosan, have limited mechanical properties. The chitosan films in dry state have a tensile strength of 30MPa with 3-5% strain (Singh and Ray 1997). In the hydrated state the elongation of chitosan increases from 5 to 70% similar to other hydrophilic materials. The modulus reduces to 6MPa (Cheng, Deng et al. 2003). However, the tensile strength of chitosan in hydrated conditions can be increased to 23MPa by increasing its molecular weight from 240 to 410kD (Rong Huei and Hwa 1996). Natural polymers are often blended with synthetic polymers to improve their mechanical strength. For example, chitosan can be blended with PLGA to fabricate a multi composite scaffold.

Synthetic polymers have superior mechanical strength compared to naturally derived polymers. For example, PCL due to the high olefinic content has mechanical properties similar to polyolefins (Wiseman, Domb et al. 1998). PCL with molecular weight 44kD has a tensile

strength of 16MPa and tensile modulus of 400MPa (Ratner, A. S. Hoffman et al. 1996). Compared to other synthetic polymers, such as PLGA, PCL has lower modulus and stress values (**Table 2.1**). However, PCL has relatively higher extensions. The mechanical properties of PCL can be controlled by adjusting its molecular weight and crystallinity. In addition, blending and copolymerization reduces the crystallinity increasing accessibility to the ester linkage and enhancing the rate of degradation (Wiseman, Domb et al. 1998). Hence, the mechanical and structural properties and degradation rate of PCL polymer can be controlled by creating polymeric blends/copolymers. Properties of various polymers used in tissue engineering are summarized in **Table 2.1**. For tissue regeneration, the scaffold should have mechanical strength comparable to the native tissue. **Table 2.2** shows the mechanical properties of various human tissues.

**Table 2.1** Properties of biopolymers used in tissue engineering. (Li, Garreau et al. 1990; Maquet and Jerome 1997; Perrin and English 1997; Middleton and Tipton 1998; Yang S, Leong KF et al. 2004).

Polymer type	Degradation time (months)*	Density (g/cm <sup>3</sup> )	Tensile strength (MPa)	Elongation %	Young's Modulus (GPa)
PLGA	Adjustable	1.27-1.34	41.4-55.2	3-10	1.4-2.8
PGA	6-12	1.53	>68.9	15-20	>6.9
PCL	>24	1.11	20.7-34.5	300-500	0.21-0.34

\*Time to completely degrade. Also depends on pore geometry.

**Table 2.2** Mechanical properties of human tissues. (Woo, Gomez M.A. et al. 1985; Silver, Christiansen et al. 1989; Fung 1993; Parsons 1998; Woo and Levine 1998; Yang 1999).

	Tensile strength (MPa)	Compressive strength (MPa)	Young's modulus (GPa)	Fracture toughness (MPa.m <sup>1/2</sup> )
Cancellous bone	NA	4-12	0.02-0.5	NA
Cortical bone	60-160	130-180	3-30	2-12
Cartilage	3.7-10.5	NA	0.7-15.3 (MPa)	NA
Ligaments	13-46	NA	0.065-0.541	NA
Tendon	24-112	NA	0.143-2.31	NA
Skin	9-40	NA	NA	NA
Aorta	0.3-0.8	NA	NA	NA

The structural configuration of the scaffold such as pore shape and size, porosity, pore interconnectivity, and permeability effect the cell behavior as these factors promote tissue growth from surrounding host tissue. For example, a large surface area to volume ratio is preferred to maximize the cell density in the scaffold (Kim B.S., C.E. et al. 2000). To control these factors scaffolds must be designed with specific architecture which is possible by using a controlled fabrication technique. The pore size of the scaffold has a significant effect on the initial network formation and cell spreading. For example, the endothelial cells (ECACC) are larger in size than 3T3 fibroblast cells. The fibroblast cells can expand in spaces up to 200µm, while endothelial cells can only span to 80 µm (Salem, Stevens et al. 2002). The porosity of the scaffold regulates cell-matrix interactions. To provide sufficient space for cell growth and Extracellular matrix (ECM) production scaffold must be highly porous (~90%). The permeability of a porous medium is dictated by the morphology and topology of the pore space structure. Some studies did not account for porosity or fluid transport through the porous structure (Williams, Saini et al. 2002;



Yeatts and Fisher 2011). For a porous material, permeability is a geometric characteristic of the porous structure orthogonal to the flow direction (Truskey, Yuan et al. 2004). Therefore, the permeability should reflect the physical characteristics such as porosity ( $\epsilon_p$ ) and the shape of the pores in the porous scaffolds. In 1927, Kozeny proposed a relationship using a capillary model, which represents a porous material as solid material containing parallel tubes of fixed cross-sectional shape

$$K = K_c \frac{\epsilon_p^3}{S^2} \quad (2.1)$$

where  $K_C$  is a dimensionless Kozeny constant and  $S$  is the specific surface area, the ratio of total interstitial surface area to the bulk volume of the porous medium.

### **2.3 Bioreactors in tissue engineering**

Bioreactors are devices used for biochemical processes under strictly monitored and controlled operating parameters, such as pH, pressure, temperature, and nutrient concentration (Martin, Wendt et al. 2004). Conventional large bioreactors are engaged in the industry for fermentation, waste water treatment, food processing, pharmaceutical, and other similar applications. For engineering tissues, bioreactors are used to provide nutrients across a biodegradable porous scaffold and provide appropriate stress necessary for tissue regeneration (Huang, Onyeri et al. 2005; Martin and Vermette 2005). Apart from creating tissue grafts, bioreactors can also be used as standalone organ support device (Mazariegos, Patzer et al. 2002). The tissues obtained from bioreactors can be used as model system to study fundamental structure-function relationships under both normal and pathological conditions (Griffith and Naughton 2002). As cells behave differently in 2D and 3D environments, the techniques used in 2D cell culture on petri dishes cannot be applied in growing 3D tissue in scaffolds (Cukierman, Pankov et al. 2001). Additionally, different cells require a unique set of condition to thrive. Hence, it is required to

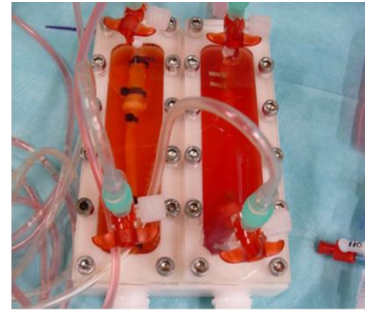
tailor the bioreactor to suit the needs of that cell line. **Figure 2.5** shows bioreactor systems used for various applications. Therefore, growing 3D tissues *in vitro* not only requires new biological models, but also poses several technical challenges related to physiochemical requirements.



Perfusion-heart valve,  
Deutsches Herzzentrum  
Berlin®



Hollow fiber -heart valve,  
University of Chicago, IL



Pulsatile flow- vascular graft,  
Aachen University and Hospital



LumeGen-vascular graft,  
Instron TGT, Norwood, MA



P3D chamber -cell  
culture, EBERS,  
Zaragoza, Spain



RCMW-Rotary Culture,  
Synthecon, Houston, TX

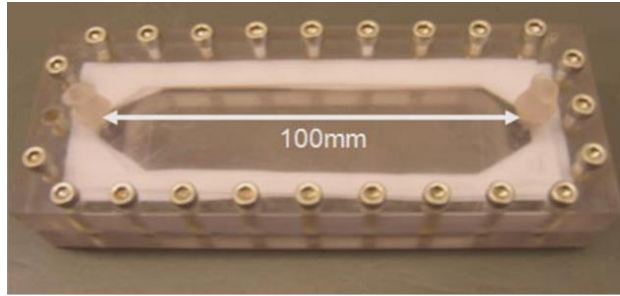
**Figure 2.5** Perfusion bioreactor systems used for 3D cell culture.

In *in vitro* cell culture, the goal is to create functional tissues from individual cells mimicking the native tissue. Hence, the native growth conditions such as uniform nutrient and stress distribution, extra cellular matrix production, and multiple cell layers must be maintained. Traditional tissue flasks and culture plates cannot support three dimensional scaffolds and high density of cells due to limitations in mass transfer. Moreover, the 3D architecture of the scaffold makes transporting nutrients and debris difficult. Specialized bioreactor devices are used to facilitate transport of nutrients necessary to culture cells at the density specific to the tissues (Ko, Milthorpe et al. 2007)

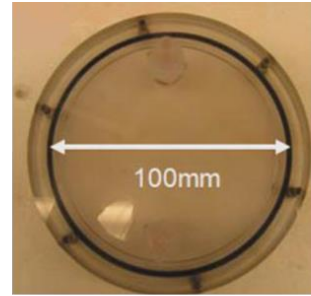
One method to sufficiently transport nutrients throughout the scaffold is by using spinner flask as described in previous publications (Upton M.T. and Flickinger T.J. 2006). The nutrients from the liquid medium are transported into the scaffold through convection. However, the main drawback of this method is that the scaffolds are not uniformly perfused. Moreover, it is difficult to obtain consistent result when 8 or more sample is cultured in one flask. An appealing alternative is bioreactor devices that allow perfusion of medium through porous scaffolds. Scaffolds are placed at the bottom of the culture rack and liquid medium is directed across the scaffold continuously (Bancroft, Sikavitsas et al. 2003; Cartmell, Porter et al. 2003). In such devices, the scaffold is subjected to the bulk forces supplied by the fluid flow, while the cells experience shear stresses (the force exerted over the cells due to media flow) within the porous scaffold. A very important parameter in designing these devices is shear stresses the cells experience in addition to scaffold deformation. Different cell types have different sensitivities to shear stress; high shear stress is deleterious to some cells while other cells need shear stress for improved function. An optimal fluid velocity promoting the proper shear stresses for the cell type being cultured is crucial. In addition, fluid stresses could deform the soft porous scaffold.

Mechanical stimulation of the cell seeded scaffolds in a manner similar to the stimuli in a normal *in vivo* environment has been demonstrated to enhance tissue growth in some bioreactor devices. In patent CA2543374A (Schulz and Augustinus 2005), mechanical stimulus is created by application of pressure on the cell-laden carrier materials using an actuator or a centrifuge. Recent designs have focused on developing bioreactors with split chambers to accommodate placement of the scaffold and cells, and facilitating internal cleaning and sterilization. However, none of the currently used perfusion bioreactors are designed with systematic analyses to improve quality of the tissue regenerated and cost-cutting measures by reducing the volume of expensive nutrient medium. Other perfusion based bioreactors are described in (Sittinger and Bujia 1999; Bancroft, Sikavitsas et al. 2003; Singh 2003; Timmins, Scherberich et al. 2007; Frerich 2011; Ma

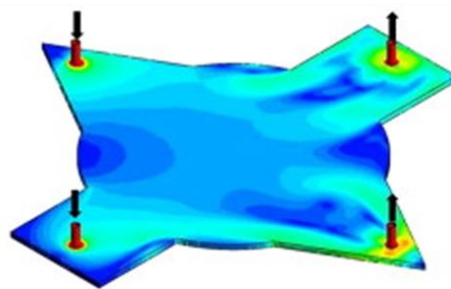
2011; Weathers and Towler 2012). However, in these bioreactor systems the stress distribution and/or pressure distribution in the scaffold is not uniform. Moreover, these methods are limited to producing smaller sized tissues. Patents US20110111504A1 (Knebel and Muehlfriedel 2011) and EP1697494B1 (Cohen, Dvir et al. 2012) describe bioreactors for producing high aspect tissues. These bioreactors systems use distributors with circular openings to improve nutrient distribution. In patent US20110111504A1 the bioreactor is setup to allow either medium overflow along with application of mechanical stimulation. In patents EP1697494B1 the scaffold is positioned between two identical nets, where each net comprise of an array of pyramidal elements protruding from the face of the net, and the vertex of each pyramid element has a circular opening. However, the aspect of uniform stress distribution across the scaffold and deformation of scaffold by fluid stress and mechanical stimulation has not been addressed. **Figure 2.6** shows bioreactor configurations developed at the Laboratory of Molecular Bioengineering at Oklahoma State University, Stillwater, OK. These bioreactors are designed to enhance mass transport of a desired medium into a developing tissue. The successful transfer of tissue engineering technology and cellular products into widespread clinical applications needs to address issues of cost, standardized monitoring, and generation of clinically-relevant tissue sizes of high quality. The axial-flow bioreactor addresses these issues while designing the bioreactors for various scaffold materials known in the art. Novelty of the axial-flow bioreactor device is that it's designed with the intent of using minimum amount of expensive nutrient medium used for growing tissues. The fundamentals of engineering were utilized to incorporate nutrient permeability, scaffold mechanical properties, and shear stress levels. A split chamber design was adapted for easy loading of scaffolds and cells.



Rectangular bioreactor (2008)



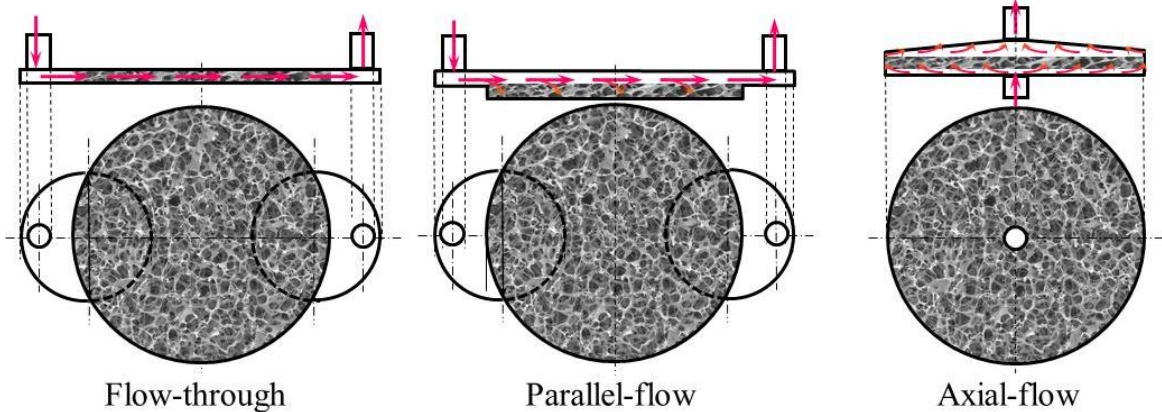
Circular bioreactor (2008)



Circular bioreactor – multiple channels (2008)



Spherical bioreactor (2009)



**Figure 2.6** Perfusion bioreactor designs, Laboratory of Molecular Bioengineering, Oklahoma State University, OK. Red arrows indicate the fluid flow path.

Beside 3D cell culture, the axial-flow allows growth of high aspect ratio tissues such as liver, kidney, and bladder. Many aspects of nutrient transport to accommodate growth of cells were thoroughly modeled, which can also be used in monitoring. Some of the unique features

1. Bioreactor allows uniform distribution of hydrodynamic stresses in the region of porous scaffolds.
2. Bioreactor size can be varied to accommodate scaffolds ranging from 1cm to 10cm diameter.
3. Flow rates are selected with the intent of providing optimal nutrient distribution, while mechanical stimulation could be incorporated using concepts known in the art independent of flow rate.
4. Residence time distribution showed uniform nutrient distribution in the scaffold.
5. Tissue growth monitoring parameters such as pressure drop and oxygen consumption are established up to the range of many healthy tissues. Devices detecting pressure drop and oxygen consumption can be mounted on the bioreactor facilitating real time monitoring.
6. The bioreactor is constructed from transparent materials, which allows easy observation of fluid flow. Also, materials such as polypropylene or polycarbonate can be used to produce low cost disposable bioreactors.

#### **2.4 Flow through porous media**

To achieve uniform nutrient and stress distribution it is critical to maintain uniform nutrient flow profile inside the flow system. These factors influence assembly of ECM and cellular colonization which determines the overall quality of the regenerated tissue. Therefore, it is vital to understand the flow distribution inside bioreactor. Several studies have been performed to examine the flow profile and shear stress within spinner flasks, rotating bioreactors and other bioreactors with small scaffolds (Williams, Saini et al. 2002; Yeatts and Fisher 2011). Most studies on the effect of shear stress on cellular activity and growth were limited to 2D culture (Kelly 2008). Parallel plate bioreactors have been used to investigate shear stress both through

computationally and experimentally analysis using micron scale surface topography.(Capuani, Frenkel et al. 2003) .

The fluid flow and concentration distribution inside the bioreactor by integrating the Navier Stokes equation (Equation 2.2) with the convective diffusion equation (Equation 2.3) (Palsson 1996) . However, these equations does not account for flow in porous scaffolds.

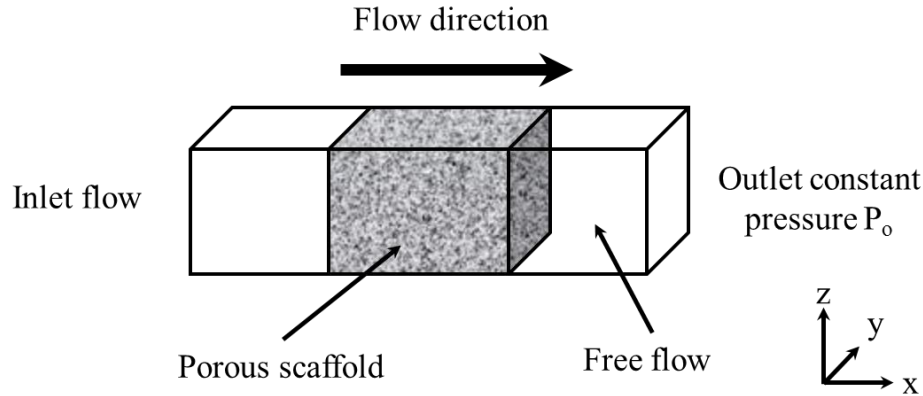
$$-\nabla \cdot \tau + \rho_f u \cdot \nabla u + \nabla p = 0 \quad (2.2)$$

where  $\tau$  is the shear stress tensor,  $\rho_f$  is the fluid density,  $p$  is the pressure and  $u$  is the velocity vector in 3D. The shear stress tensor is calculated using the velocity vector (Lawrence, Devarapalli et al. 2009). For fluid flow through a porous medium at low Reynolds number the fluid flow is governed by Darcy's law. According to Darcy's law the flux  $q$  (discharge rate per unit area) of the fluid is proportional to the pressure gradient  $\Delta P$ . To analyze flow through porous media, several studies have used small cylindrical or discoid scaffolds (15mm diameter and few mm thick) and have focused on wall shear stress (Palsson 1996). Typically, flow is characterized by either Darcy's equation (Stephens, Cooper et al. 2007) or the Brinkman equation.(Raimondi, Moretti et al. 2006) The Brinkman equation is an extension of Darcy's Law that accounts for viscous effects at the boundary surface (Chung, Chen et al. 2007)

$$\mu \nabla^2 u_s - \frac{\mu}{\kappa} u_s = \nabla p \quad (2.3)$$

where,  $\kappa$  is the permeability of the porous medium,  $u_s$  is fluid superficial velocity vector,  $p$  is the fluid pressure, and  $\mu$  the effective viscosity in the porous medium. When combining free flow and flow in porous media Brinkman equation is recommended as it allows continuity of velocity, normal stress, and shear stress at the interface (Podichetty and Madihally 2014) . **Figure 2.7** shows a simple perfusion system with flow through porous media. For flow through an open

channel where  $\kappa$  becomes infinite, and Equation (2.4) reduces to incompressible Navier-Stokes equation.



**Figure 2.7** Schematic of a system with flow through porous media.

A general idea of the typical operating range for design parameters such as pressure drop and flow rate can be useful in predicting their optimum values. For Mesenchymal stem cells (MSCs) cells in perfusion bioreactor it was found that higher flow rate increased ECM formation, improved nutrient delivery inside the scaffold, and stimulated the seeded cells by fluid shear forces. (Bancroft, Sikavitsas et al. 2002; Sikavitsas, Bancroft et al. 2003; Gomes, Bossano et al. 2006). However, increased flow rate could result in scaffold deformation and cell and ECM wash away. For hepatocytes in perfusion system a flow rate of 1mL/min was found to be just sufficient for the survival of initial cell mass , and 1.5mL/min provided sufficient oxygen delivery (Kim, Sundback et al. 2000). Computational fluid dynamics (CFD) can help predict optimal flow conditions for a bioreactor system. The shear stress, mass transport, and flow regimes can also be examined.

## 2.5 Nutrient consumption in porous media

Bioreactors are primarily used to replenish nutrients constantly to maintain optimum conditions throughout the development process. In flow systems such as perfusion bioreactors, the mass



transport of nutrient species is typically defined using the convection-diffusion equation. This process involves both nutrient transports through diffusion and velocity variations that lead to concentration gradients.

$$\nabla \cdot (-D\nabla c) + u \cdot \nabla c = r_A \quad (2.4)$$

where  $c_A$  is the concentration of the species,  $r_A$  is the rate of reaction,  $D$  is the diffusivity of the species, and  $u$  is velocity. The rate of reaction in Equation (2.5) represents the rate of nutrient consumption. The reaction rate for oxygen and glucose is typically obtained using the Michaelis-Menten equation (Patrachari, Podichetty et al. 2012).

$$-r_A = \frac{V_m C_A}{K_m + C_A} \quad (2.5)$$

where,  $V_m$  is the maximum reaction rate, and  $K_m$  is the Michaelis constant. The value of the parameters depends on the cell type and must be obtained through experiments.

## 2.6 Non-ideal fluid distribution models for predicting exit concentration

One of the widely used non-ideal fluid distribution model is the segregation flow model. According to this model the each fluid element entering the reactor resides for a unique period of time before it exits the reactor. The fluid elements spend different amount of time in the reactor. The age distribution function describes the time spent by the fluid elements in the reactor. The reaction in the fluid element begins when the fluid element enters the reactor and the reaction stops when the fluid element exits the reactor. As the fluid elements have different residence time, the compositions of the fluid elements exiting the reactor are different. However, since the fluid element is perfectly mixed, the exit composition of the fluid element can be calculates from the initial fluid composition and the residence time of that fluid element. This can be done by combining batch reactor equation with resident time of the fluid element. As the design equation

is solved on an arbitrary basis, the final composition must be expressed as an intensive variable such as concentration or conversion.

The segregation model can be applied to evaluate the exit concentration in a bioreactor, based on the assumption that cells present on scaffold are surrounded by a nutrients film and behave like micro batch reactors. The average conversion,  $\bar{X}_A$ , can be obtained using the equation

$$\bar{X}_A = \int_0^{\infty} (X_A(t))_{batch} E(t) dt \quad (2.6)$$

where  $(X_A)_{batch}$  is the conversion obtained in a batch reactor for time t. Since the reaction is in liquid phase, a constant volume was assumed. The batch conversion at any time, t, is obtained using the rate of reaction equation

$$r_A = \frac{-C_{A0} d(X_A)_{batch}}{dt} = -\frac{V_m [1 - (X_A)_{batch}]}{[K_m + C_{A0} [1 - (X_A)_{batch}]]} \quad (2.7)$$

Equation (2.7) is rearranged and integrated to obtain  $X_A(t)_{batch}$  function as

$$C_{A0} * (X_A)_{batch} - K_m * \ln(1 - (X_A)_{batch}) - t * V_m = 0 \quad (2.8)$$

Obtained  $X_{batch}$  for each time point was multiplied with the E(t) function and integrated numerically to obtain the average conversion.

Another model to describe non-ideal flow distribution in reactor systems is the dispersion model. Typically, in plug flow reactor model, the concentration varies in the axial direction as a result of convection plus reaction. The model is governed by an analogy to Fick's law of diffusion, which is superimposed on the flow. Apart from the bulk transport, every component is transported through the cross section at a rate  $-DA \frac{dC}{dz}$ , where D is diffusivity, A is cross section area, C is the concentration, and z is the length, as a result of molecular and convection diffusion. The

dispersion model can be applied to flow systems such as laminar flow in long tubes, packed beds, turbulent flow in pipes, and long channels. However, this model is not applicable to laminar flow of viscous materials as the parabolic velocity profile will cause deviation from plug flow. Based on the assumption that much of the changes happen within the scaffold region i.e., a closed vessel with large deviations ( $1/Pe_D > 0.01$ ) from plug flow reactor dispersion number can be calculated using the equation

$$\frac{\sigma^2}{t_m^2} = \frac{2}{Pe_D} \left[ 1 - \frac{1}{Pe_D} (1 - e^{-Pe_D}) \right] \quad (2.9)$$

The modified Peclet number ( $Pe_D$ ) is calculated using experimentally determined  $\frac{\sigma^2}{t_m^2}$  values.

This model involves dispersion of the material in the axial direction. Based on Michaelis-Menten consumption kinetic equation for oxygen and glucose, outlet concentration of oxygen and glucose is calculated based on the shell balance

$$\frac{1}{Pe_D} \frac{d^2 C_A}{dz^2} - \frac{dC_A}{dz} - \frac{v_{\max} C_A}{K_M + C_A} = 0 \quad (2.10)$$

with the Danckwerts (originally derived by Langmuir) boundary conditions (BC)

$$\text{BC at the entrance, } C_A + \frac{1}{Pe_D} \frac{dC_A}{dz} = C_{A0}$$

$$\text{BC at the exit, } \frac{dC_A}{dz} = 0$$

The above PDE can be solved numerically for various flow rates using partial differential equations tool to obtain the exit concentration.

## **2.7 Computational fluid dynamics in bioreactor design**

CFD is useful in evaluating flow patterns inside bioreactors (Porter, Zauel et al. 2005; Cioffi, Boschetti et al. 2006; Hutmacher and Singh 2008; Wendt, Riboldi et al. 2011). CFD analysis can be used to understand the influence of nutrient transport on cell growth and effect of dynamics of cell proliferation in a bioreactor. In addition, CFD can help characterize fluid flow, provide initial estimates, and supplement experimental results. Hence, CFD offers several advantages in the development of tissue engineering.

Typically, structural mechanics involves estimation of deformation, deflection, and stresses within a structure to design or evaluate performance of the structure. Fluid-structure interaction problems are often too complex to solve analytically and require experimental or numerical simulation. CFD can be used to perform structural mechanics simulations on porous scaffolds. The fluid exerts viscous and pressure forces on the scaffold resulting in deformation. When the scaffold undergoes large deformation, the fluid flow region also changes accordingly. CFD can be used to account for these changes by computing fluid flow and changes in the porous structure on a moving mesh. The structural deformations are computed using an elastic formulation and a nonlinear geometry formulation that allow large deformation. In addition, it is possible to couple fluid flow, structural mechanics, and consumption kinetic to analyze structural deformation and nutrient consumption profile in porous scaffolds.

## **2.8 Three-dimensional cell culture in perfusion bioreactors**

Culturing cells in a 3D scaffold by mimicking the cells native environment is valuable in developing physiological *in vitro* models to examine cell growth mechanism, differentiation, and tissue development (Timmins, Scherberich et al. 2007). As discussed earlier, various types bioscaffolds and bioreactors have being employed for the purposes mentioned above. However,

there are several limitations with these methodologies, particularly when the scaffold sizes are smaller with few millimeters in thickness.

There are several challenges associated with culturing cells under static conditions including non-uniform cell distribution and inadequate nutrient supply to support cell growth and function, ECM production, and viability in the entire scaffold (Ishaug, Crane et al. 1997; Ishaug-Riley, Crane-Kruger et al. 1998; Kim, Putnam et al. 1998; Burg, Delnomdedieu et al. 2002; Martin and Vermette 2005; Zhao and Ma 2005). Dynamic cultures such as stirred system are superior to static cultures (Kim, Putnam et al. 1998; Wendt, Riboldi et al. 2011). However uniform cell distribution and nutrient transport through the thickness of the scaffold remains a challenge (Ishaug-Riley, Crane-Kruger et al. 1998). Perfusing media through the scaffold can overcome limitations associated with static and stirred cell culture. Perfusion of media through scaffold pore has shown to facilitate high cell seeding efficiency with uniform distribution and while maintaining cell viability with large scaffolds for long durations (Kim, Sundback et al. 2000; Wendt, Marsano et al. 2003; Martin, Wendt et al. 2004). In addition, the flow induced shear stress helps in cell proliferation, differentiation and ECM production (Hosseinkhani, Inatsugu et al. 2005). Perfusion bioreactor can also be used to study the fundamentals of tissue regeneration process *in vitro* under controlled operating conditions (Gomes, Bossano et al. 2006). **Figure 2.8** shows a 3D perfusion bioreactor system with pump (3D Biotek LLC, North Brunswick, NJ ) that can be purchased from Sigma-Aldrich.



**Figure 2.8** Perfusion bioreactor system with peristaltic pump from 3D Biotek LLC, North Brunswick, NJ.

This bioreactor consists of multiple polycarbonate chamber that can house 3D scaffold with sizes ranging from 96-well to 6-well. This bioreactor is suitable for stem cell research. However, unlike static culture perfusion systems involve several components such as pump, tubing, connector, and fittings. Additionally, these systems are relatively expensive and typically need a skilled operator to reduce the risk of leakage and contamination. These limitations can be overcome by developing perfusion systems that are compact, inexpensive, and easy to use.

## CHAPTER 3

### MODELING MEDIA INDUCED POROUS SCAFFOLD DEFORMATION

#### 3.1 Introduction

Tissue regeneration is a dynamic process where the porous characteristics change due to proliferation of cells, de novo deposition of matrix components, and degradation of the porous architecture. These changes affect the transport characteristics. The medium perfusion through the scaffold helps dictate the hydrodynamic shear stress that leads to altered gene expression profiles and functional changes (Haga, Li et al. 2007; Trepap, Deng et al. 2007). Cells respond to mechanical stress either inherent in the scaffold or externally applied by stretching the scaffolds (Discher, Mooney et al. 2009). The medium perfusion through cell seeded scaffold affects the production of ECM components and differentiation of stem cells (Niklason, Gao et al. 1999; Kim and Ma 2012); shear stress induces increased ECM release (Gooch, Kwon et al. 2001; Heydarkhan-Hagvall, Esguerra et al. 2006). Different flow regimes have been used to stimulate cellular activity, while ensuring nutrient sufficiency (McCoy and O'Brien 2010). However, perfusion may cause deformation in the scaffold depending on its porous architecture, mechanical properties, flow configuration in the bioreactor, and medium flow rate. Although calculating the scaffold extension for use as a pre-conditioning in the bioreactor has been studied (Butler, Hunter et al. 2009), the mechanical deformation caused by perfusion through scaffolds of varying pore characteristics and mechanical properties and flow rate is not well understood.

Understanding the dynamic changes during the regenerative process needs further investigation. In particular, the effect of hydrodynamic force on soft scaffolds dimensionality is not investigated when performing simulations to understand shear stress distribution. One has to understand the influence of fluid flow on structural changes and its impact on fluid distribution patterns (Heydarkhan-Hagvall, Esguerra et al. 2006).

The medium exerts pressure forces on the scaffold resulting in deformation and volumetric changes in the pores. The theory of poroelasticity is used for analysis of a porous media deformation consisting of an elastic matrix containing interconnected fluid-saturated pores (Cowin 1999). Poroelasticity theory has been applied to study soil consolidation and bone biomechanics (Sengers, Oomens et al. 2004; Hellmich and Ulm 2005). Also, structural mechanics is used to evaluate deformation, deflection, and stresses based on structural loads, material properties, and geometric configuration.

Advances in computational fluid dynamics (CFD) allows performing simulations on porous scaffolds (Patrachari, Podichetty et al. 2012), with the inclusion of many factors including the effects of medium perfusion by coupling structural mechanics. In this study, the effect of medium perfusion on scaffold deformation was tested by combining structural mechanics and fluid mechanics. Polycaprolactone (PCL) and chitosan – gelatin (CG) scaffolds were utilized as they encompass a wide range of properties. A well characterized flow-through bioreactor designed for uniform hydrodynamic stress in the scaffold region was used to study deformation (Devarapalli, Lawrence et al. 2009). Since some experimental results in the previous study with CG scaffolds showed deformation, mechanical properties of scaffolds were included in simulations. Further, the effects of change in scaffold permeability, elastic modulus, and Poisson's ratio on structural deformation were studied. These results showed significant dependency of deformation on scaffold permeability and mechanical properties.



## **3.2 Materials and methods**

### **3.2.1 Sources of materials**

PCL of molecular weight 80,000Da (referred as 80kDa), chitosan of 190-310kDa molecular weight (Low molecular weight and 85% degree of deacetylation), gelatin Type-A (Bloom 300) from porcine skin, and glacial acetic acid were obtained from Sigma Aldrich Chemical Co. (St. Louis, MO). Chloroform and ethanol (200 proof) was obtained from Aaper Alcohol and Chemical Company (Shelbyville, KY). All other reagents were purchased from Fisher Scientific (Waltham, MA) and used as received without further purification.

### **3.2.2 Preparation of porous scaffolds.**

Scaffolds with a thickness of 0.2cm were prepared using a circular mold with a diameter of 10cm on a Teflon sheet (US Plastics Co). PCL solution was prepared by dissolving 2.7g of PCL in 16mL of chloroform. To obtain 85% porosity scaffold, 29g of common salt with a crystal size between 74  $\mu\text{m}$  -246 $\mu\text{m}$  was added to the PCL solution. Common salt was milled using a mortar and pestle and sieved using trays with sieve 74 $\mu\text{m}$  and 246 $\mu\text{m}$  sizes. The mixture was poured in the well, air dried for 8 hours in a ventilated hood to evaporate chloroform. The scaffold was removed and placed in distilled water for 36 hours to dissolve the salt. Distilled water was replaced every 3 h.

CG scaffolds were prepared following the procedure previously described (Podichetty, Dhane et al. 2012). In brief, 2% (wt/v)-2% (wt/v) chitosan-gelatin solution was prepared in 0.5M acetic acid and 25mL of the solution was poured in the wells. Solution was frozen overnight at -80°C and freeze dried overnight in a VirTis freeze dryer (SP Scientific Gardiner, NY). Prior to hydration, all scaffolds were immersed in absolute ethanol until they were completely saturated without any air pockets, and then washed in phosphate buffered saline (PBS, pH=7.4) solution prior to further use.

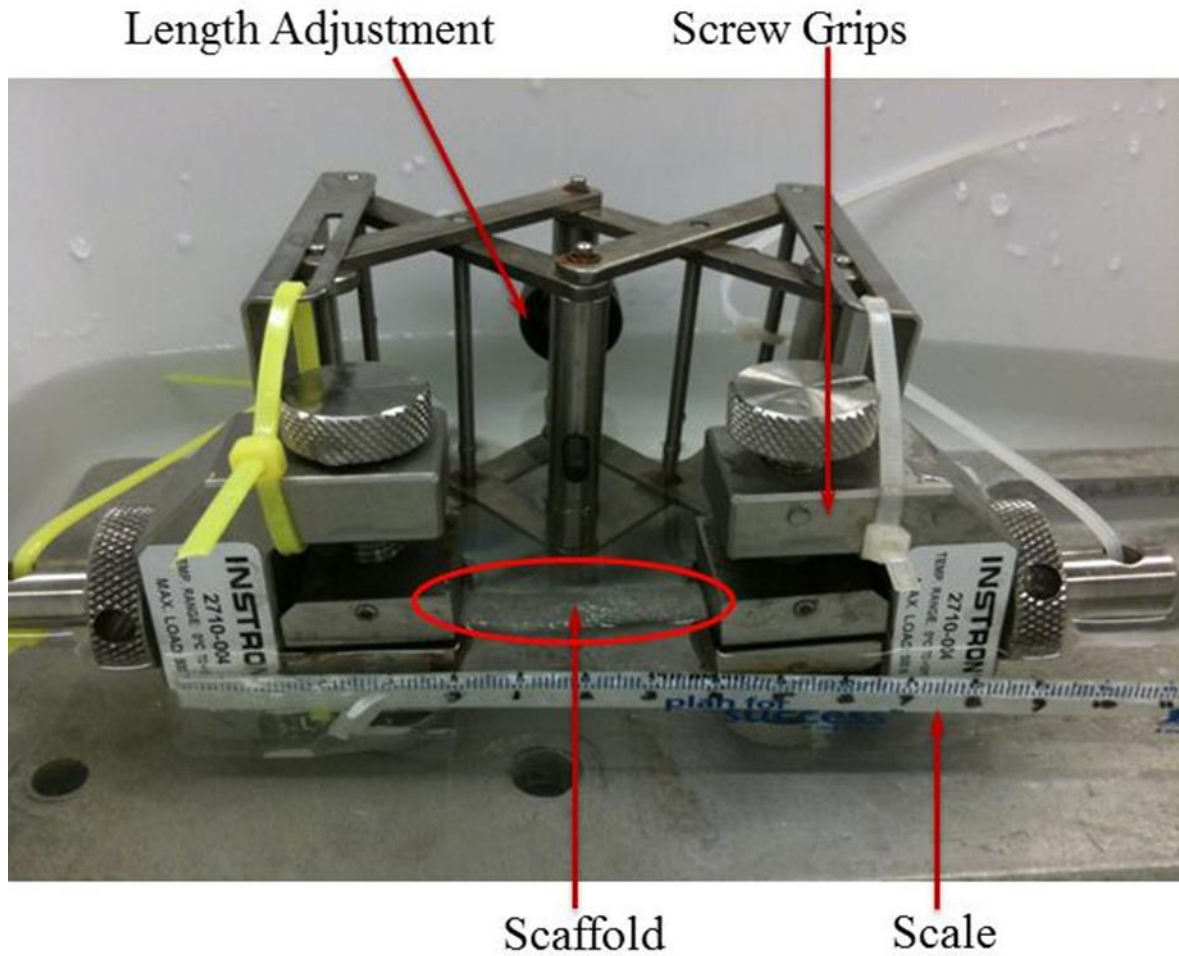
### **3.2.3 Estimation of pore size and porosity of scaffolds.**

Dry scaffolds with thickness 0.2cm were examined using a scanning electron microscope (SEM, Joel JSM 6360) at an accelerating voltage of 10kV after gold sputter coating at 40mA(Lawrence, Maase et al. 2009). Hydrated scaffolds were characterized for pore area, size, and number using thin strips mounted to view the thickness on an inverted microscope (Nikon TE2000, Melville, NY) and obtained digital micrographs were analyzed for open pore area using Sigma Scan Pro 5 (SPSS Science, Chicago, IL) software. Assuming isotropic distribution of pores in the plane of view, porosity was calculated as the ratio of open pore area to the total image area. At least 3 to 4 images per sample and more than 50 pores were analyzed to calculate the porosity for each condition.

### **3.2.4 Estimation of elastic modulus and Poisson ratio.**

The scaffolds were cut into 5cm×1cm×0.2cm rectangular strips. Similar to previous publication(Lawrence, Maase et al. 2009), tensile tests were performed under physiological conditions (PBS at pH 7.4 and 37°C) using Instron 5542 (INSTRON, Canton, MA) equipped with a 100N load cell and a custom-built environmental chamber. Scaffolds were strained to break at a cross head of 10mm/min. Data collected using Merlin (INSTRON, Canton, MA) software was exported to Microsoft® Excel and analyzed for elastic modulus from the slope of stress (MPa) vs strain in the linear region. Experiments were repeated four times and the average and standard deviations were calculated.

Poisson's ratio of scaffolds under hydrated conditions was determined using a customized apparatus built in-house (**Figure 3.1**) by measuring the transverse strains at various axial strains under physiological conditions.



**Figure 3.1** Experimental setup used for determining Poisson's ratio of scaffolds in hydrated condition.

Two INSTRON® screw grips were attached to an adjustable steel frame and scaffolds of  $7\text{cm} \times 1\text{cm} \times 0.2\text{cm}$  were used. A scale was attached to one of the screw grips. The setup was placed inside a plastic container, which was filled with PBS maintained at  $37^\circ\text{C}$ . Each sample was stretched along its length in increments of predetermined longitudinal extensions using an adjustable knob located in the back of the frame. At those extensions, changes in width were recorded using a digital vernier caliper. Knowing the initial length and width, strains in both longitudinal ( $\epsilon_{\text{long}}$ ) and transverse ( $\epsilon_{\text{trans}}$ ) directions were calculated and plotted. The strain limits

were chosen to be within the linear region based on the prior tensile testing. Poisson's ratio was determined as the slope of the line, with the line passing through the origin (**Table 3.1**). Experiments were repeated three times and the average and standard deviations were calculated.

**Table 3.1** Density and Poisson's ratio of CG and PCL

Scaffold	Freezing Temp (°C)	Density (kg/m <sup>3</sup> ) <sup>#</sup>	Poisson's ratio(v) <sup>#</sup>
CG (1%-1%)	-20	32±3	1.1 ± 0.21
CG(1%-1%)	-80	50±2	0.80 ± 0.12
CG (2%-2%)	-20	65±2	1.2 ± 0.13
PCL	NA	124.5±5.5	0.3±0.02

# measured

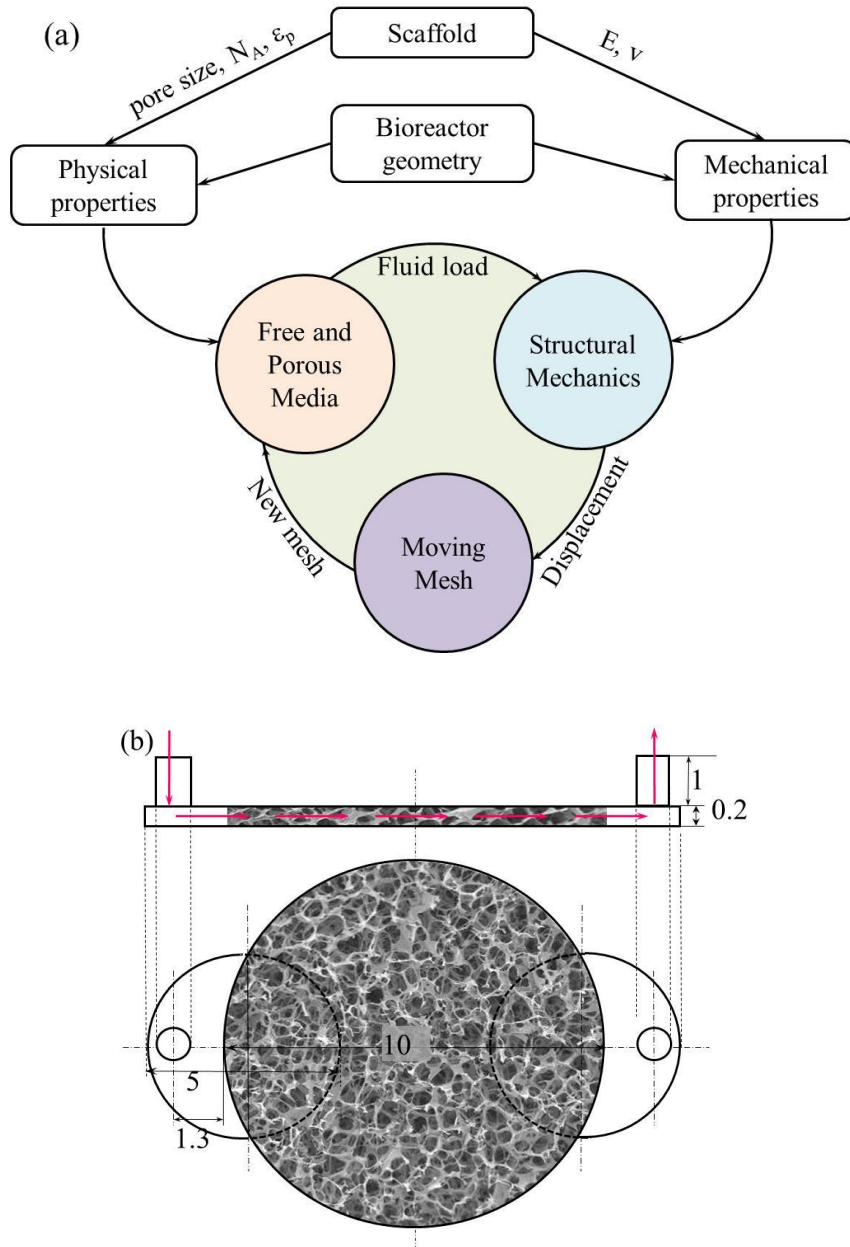
### 3.2.5 Pressure drop measurement.

Experiments were performed at flow rates from 5mL/min to 25mL/min with 5mL/min increments using 10cm diameter and 0.2cm thick scaffolds following the procedure described previously (Podichetty, Dhane et al. 2012). In brief, a flow-through bioreactor which allows housing the 0.2cm thick and 10cm diameter scaffold was constructed in-house using polycarbonate plastic. Scaffold was placed in the flow-through bioreactor and attached to a flow system consisting of a fluid reservoir, a variable speed Masterflex L/S peristaltic pump (Cole-Parmer, Vernon Hills, IL), an in-line physiological pressure transducer (Capto SP844, Skoppum, Norway), and a waste reservoir. Data from the pressure transducer were retrieved using Chart™ 5 for Windows via Powerlab/4SP System (ADI Instruments, Inc., Colorado Springs, CO). Data were recorded after allowing the bioreactor to reach steady state for every flow rate, based on the output signal (and four times the space time). Experiments were performed with and without the scaffolds and the difference in pressure drop between those settings were considered as the pressure drop due to the scaffold. Experiments were repeated four times and the average and standard deviations were calculated.

### 3.3 Computational modeling

Two basic phenomena underlie fluid-porous media behavior: i) fluid-to-solid coupling occurs when a change in fluid pressure or fluid mass is responsible for a change in the volume of the porous material; ii) solid-to-fluid coupling occurs when a change in applied stress produces a change in fluid pressure or fluid mass (Suarez Arriaga 2012). The magnitude of the solid-fluid coupling depends on the compressibility of the solid, fluid, porous structure, and scaffold porosity. In addition, the type of coupling determines if the iteration scheme is linear or non-linear and indicates the extent of deformation that can be predicted. Therefore, the type of coupling directly influences the accuracy of model predictions. Studying the effects of fluid induced-stress on porous structures requires coupling flow equations with structural mechanics of the porous structure. The coupling is facilitated by creating a dynamic mesh that responds to the fluid induced stresses calculated based on the pore characteristics and mechanical properties. CFD simulations were performed by computing fluid flow and changes in the porous structure on a dynamic mesh to understand how fluid flow deforms the scaffold. Following conditions and equations were used while performing simulations (**Figure 3.2a**):

*Bioreactor geometry.* The bioreactor geometry was created using Computer Aided Design (CAD). A flow-through bioreactor configuration with a circular scaffold of 10cm diameter and 0.2cm thickness was used (**Figure 3.2b**). The bioreactor geometry was divided into two domains, porous and non-porous. The medium enters through the inlet into the non-porous domain, flows through porous domain, enters the second non-porous domain, and finally exits the bioreactor at the outlet. The effects of gravity were assumed to be negligible relative to the flow rate.



**Figure 3.2** Modeling and bioreactor schematic (a) fluid flow – structural mechanics coupling modeling approach. Flow through porous media is coupled with structural mechanics and dynamic mesh via load descriptions, and simulations performed until convergence. (b) Schematic of flow-through bioreactor showing the side view and the top view. All shown dimensions are in cm and location of the scaffold is also shown. Arrows indicate the direction of medium flow.

The meshing of the top layer (boundary) was performed using free mesh parameters with triangular mesh and maximum and minimum element size of 0.0225m and 0.0042m respectively. The swept mesh parameter was used to mesh the whole geometry. The scaffold thickness was divided into 7 layers. Overall, this created 40,662 nodes. Increasing the number of nodes altered the pressure drop predictions only by less than 0.2%. Hence, the number of nodes was considered to be optimum.

Permeability equations: The scaffold permeability is a key parameter that best represents geometrical features of a scaffold. Typically, when modeling fluid flow and permeability in regular scaffolds, analytical formula (Innocentini, Salvini et al. 1999; Truskey, Yuan et al. 2004) or homogenization techniques (Hollister and Lin 2007; Sanz-Herrera, Garcia-Aznar et al. 2009) are used to determine the permeability. An analytical approach such as the Kozeny-Carmen equation expresses the relation between permeability and pore properties. Based on Kozeny-Carmen relationship, equations derived for cylindrical and rectangular pores were used to estimate permeability. Based on the shape factor of the pores, the PCL scaffolds fabricated using salt leaching technique was considered to have rectangular pores. Similar to cylindrical pores, the permeability of PCL scaffold was calculated using the following equation assuming rectangular pores.

$$k = \frac{n_A L W^3}{12} \quad (3.1)$$

where  $n_A$  is the number of pores per unit area,  $L$  is the pore length, and  $W$  is the pore width. For freeze dried scaffold, the pores were considered cylindrical based on the shape factor (or circularity factor) of the pores, as described previously (Podichetty, Dhane et al. 2012). Hence for CG scaffolds the permeability ( $m^2$ ) of the porous medium ( $\kappa$ ) was calculated using the equation

$$k = \frac{\pi}{128} n_A d^4 \quad (3.2)$$

where  $d$  is the pore diameter and  $n_A$  is the number of pores per unit area.

Flow equations: The fluid velocity in the non-porous regions was described by continuity equation and Navier-Stokes equation

$$\nabla \cdot \mathbf{u} = 0 \quad (3.3)$$

$$-\nabla \cdot \boldsymbol{\tau} + \rho \mathbf{u} \cdot \nabla \mathbf{u} + \nabla p = \mathbf{0} \quad (3.4)$$

where  $\boldsymbol{\tau}$  is the shear stress tensor,  $\rho$  is the fluid density,  $p$  is the pressure and  $\mathbf{u}$  is the velocity vector in 3-D. The viscosity and density of the fluid was assumed to be constant. Shear stress tensor was calculated using the velocity vector (Lawrence, Devarapalli et al. 2009). Flow characteristics in the porous region were predicted using Brinkman equation

$$\frac{\eta}{k} \mathbf{u}_s = -\nabla \cdot \left[ \frac{-\boldsymbol{\tau}}{\varepsilon_p} + p \boldsymbol{\delta}_{ij} \right] \quad (3.5)$$

where  $\eta$  is the dynamic viscosity,  $\mathbf{u}_s$  is the superficial velocity vector,  $\varepsilon_p$  scaffold porosity,  $\boldsymbol{\delta}_{ij}$  is the Kronecker delta function and  $p$  is the fluid pressure. Density and viscosity of water were used in the calculation. Structural properties used in the simulation are shown in **Table 3.2**. Average and maximum Reynolds numbers (**Table 3.3**) were calculated using the average and maximum interstitial velocities within the scaffold region using the equation (Tilton 2007).

$$\text{Re} = \frac{u_i \Phi_s D_p}{\eta (1 - \varepsilon_p)} \quad (3.6)$$



where  $\Phi_s$  ( $\sim 1$  for short cylinders) is the sphericity,  $D_p$  is the pore diameter, and  $u_i$  is the interstitial velocity. Simulations were performed at flow rates from 0.1mL/min to 25mL/min. The average and maximum interstitial velocities in the porous domain were retrieved from the simulation.

**Table 3.2** Modeling data for CFD simulations

VARIABLE	SYMBOL	Value
Fluid density of medium (Podichetty, Dhane et al. 2012)	$\rho_f$	1000 kg/m <sup>3</sup>
Dynamic viscosity of medium (Podichetty, Dhane et al. 2012)	$\eta$	0.000615 Pa.s
Biot-Willis coefficient (assumed)	$\alpha$	0.95
PCL scaffold - Pore Length (measured)	L	53±9µm
PCL scaffold - Pore Width (measured)	W	27±4µm
PCL scaffold – Pore per unit mm <sup>2</sup> (measured)	$n_A$	128±37
Permeability of CG scaffolds (calculated)	$k$	7.27×10 <sup>-11</sup> m <sup>2</sup>
Permeability of PCL scaffolds (calculated)	$k$	7×10 <sup>-10</sup> m <sup>2</sup>
Porosity of CG scaffolds (measured)	$\epsilon_p$	0.85 (±0.04)
Porosity of PCL scaffolds (measured)	$\epsilon_p$	0.83 (±0.02)
Elastic modulus of CG scaffolds (Ratakonda, Sridhar et al. 2012)	E	9.14 (±0.4) kPa
Elastic modulus of PCL scaffolds (measured)	E	600 (±100) kPa

**Table 3.3** Reynolds number calculations in the porous scaffold

inlet flow rate(mL/min)	inlet velocity (mm/s)	Average Interstitial velocity <sup>#</sup> (mm/s)	Average Reynolds number <sup>†</sup>	Maximum Interstitial velocity <sup>#</sup> (mm/s)	Maximum Reynolds number <sup>†</sup>
5	2.9	0.372	0.20	1.78	0.94
10	5.8	0.747	0.40	3.56	1.89
15	8.7	1.12	0.59	5.33	2.83
20	11.6	1.49	0.79	7.11	3.77
25	14.58	1.88	1.00	8.94	4.74

<sup>#</sup> CFD <sup>†</sup>Calculated

**Structural mechanics:** The initial total load ( $F_T$ ) established by the Navier-Stokes equation simulated with the assumption of non-deformable objects was set as the load on the boundaries.

This fluid load is given by

$$F_T = -n \cdot (-pI + \tau) \quad (3.7)$$

where  $n$  is the normal vector to the boundary, and  $I$  is the identity matrix. The scaffold experiences stress from fluid pore pressure in addition to the stress due to the elastic nature, which was accounted by coupling the strain using the relationship

$$\sigma + \alpha_B p_f I = C \varepsilon \quad (3.8)$$

where  $C$  is the elasticity matrix,  $\sigma$  is the Cauchy stress tensor,  $\varepsilon$  is the strain tensor,  $\alpha_B$  is the *Biot-Willis coefficient*, (also referred as Skempton's  $A$  parameter), and  $p_f$  is the fluid pore pressure. The Biot-Willis coefficient is the ratio of the pore compressibility to the Elastic modulus. A soft porous material has a Biot-Willis Coefficient close to one, whereas a stiff porous material has a Biot-Willis Coefficient close to its porosity due to inhibition of pore compression. When Biot-Willis Coefficient is zero, the equation resembles Hooks Law used in solid mechanics. A Biot-Willis Coefficient of 0.95 was assumed for both scaffolds.

The linear elasticity matrix was obtained using the values of elastic modulus,  $E$  and the shear modulus,  $G$ . Poisson's ratio and elastic modulus were used to calculate the  $G$  using the linear elastic relationship

$$E = 2(1 + \nu) G \quad (3.9)$$

*Dynamic mesh:* To perform fluid flow-structural mechanics coupling, the fluid stress and strain calculated from flow equation was used to predict mesh displacement, which was used to move the mesh. The new mesh was used to predict the new pressure drop using the flow equations. The fluid pressure ( $p$ ) was evaluated from free and porous media physics. The pore pressure was calculated by multiplying the fluid pressure with *Biot-Willis coefficient* ( $\alpha$ ). The fluid load per unit volume or body load was obtained by dividing pore pressure with  $x$ ,  $y$ , and  $z$ , the lengths in three directions. The body load was used by the structural mechanics physics to calculate the

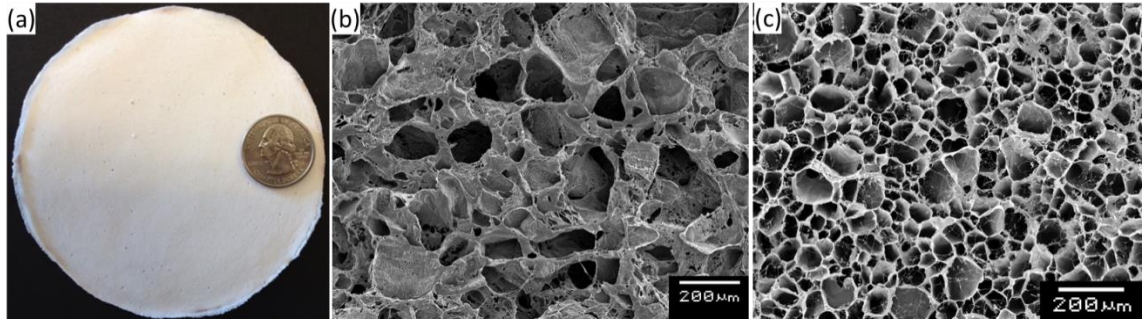
strain and displacement in the mesh. The new mesh was used by free and porous media physics to calculate the new pressure drop. This process was repeated until the solution converged. Finally, pressure drop profiles with deformation were examined in the scaffold.

*Numerical solvers:* The simulation was performed with stationary segregated solver using a three step process. A MULTifrontal Massively Parallel Sparse (MUMPS) direct solver was used for the first step to evaluate variables x, y, and z and Generalized Minimal Residual (GMRES) iterative solver was used for the second and third steps to evaluate fluid velocity and pressure for second step and mesh displacement for the third step. A maximum of 200 iterations was performed in the second and the third steps.

### **3.4. Results and discussion**

#### **3.4.1 Scaffold characterization.**

In this study, 10cm diameter and 0.2cm thick scaffolds made from PCL and CG were used to validate the simulation results. Using large-size scaffolds helps in detecting the effect of various factors with greater accuracy due to very high signal to noise ratio in data recording while making it possible to regenerate clinically relevant large tissues such as bladder, abdominal wall, skin, and cartilage. Formed scaffolds were observed for cracks and non-uniformity, and intact scaffolds were selected (**Figure 3.3a**) prior to use in experiments. Pores depicted the shape of the salt crystals throughout the PCL scaffold (**Figure 3.3b**). The size of the pores varied according to the crystal size. Pore interconnectivity was assessed by the phase contrast microscopy in hydrated condition by observing the samples at different elevations. The pore analysis of PCL scaffolds gave an average pore length (L) of  $53(\pm 9)\mu\text{m}$ , average pore width (W) of  $27(\pm 4)\mu\text{m}$ , and pore number ( $n_A$ ) of  $128(\pm 37)\text{pores}/\text{mm}^2$ . Using these values in Equation (3.1), permeability value of  $7 \times 10^{-10}\text{m}^2$  was obtained which was used in simulations.



**Figure 3.3** Macroscopic and microscopic appearance of scaffolds a) Photograph of a 10cm diameter scaffold. b) Micrograph showing PCL scaffold porous architecture. c) Micrograph showing CG scaffold porous architecture.

CG scaffolds have been characteristics based on freezing temperature and concentration (Podichetty, Dhane et al. 2012). Increased CG concentration, increased scaffold thickness, and reduced the pore size, the number of pores per unit area and the porosity. However, pore shape was not affected by the change in concentration as ice crystals define the pore shape. Pore analysis of 2%(wt/v) -2%(wt/v) CG scaffolds indicated an average pore diameter ( $d$ ) of  $55\mu\text{m}$  and pore number ( $n_A$ ) of  $318\text{pores}/\text{mm}^2$ . Typically, the shape factors of the pores in the flow direction were  $\sim 0.8$  in these scaffolds (circularity factor, defined as  $4\pi \times \text{area}/\text{perimeter}^2$  and when the number is closer to 1 the shape is closer to that of a circle). Hence, pores were considered to be circular shape while calculating the permeability using Equation (3.2), and obtained  $7.27 \times 10^{-11} \text{m}^2$ , which was used in simulations.

### 3.4.2 Poisson's ratio measurement.

When a material deforms, it experiences dimensional changes in both axial (along the direction of applied load) and transverse (orthogonal to the applied load). These changes in dimensions are characterized by Poisson's ratio. The plot of transverse strain vs axial strain showed a linear trend in the measured area and Poisson's ratio was calculated by the slope. The Poisson's ratio of PCL scaffold was found to be  $0.3(\pm 0.02)$ , which is within the typical range of -1 to 0.5 typical

isotropic materials. Using an optical approach others have shown similar range of Poisson's ratio for synthetic scaffolds (Moroni, de Wijn et al. 2006). However, Poisson's ratio for CG scaffolds was  $> 0.5$ , typically considered to follow non-linear elastic behavior (Ratakonda, Sridhar et al. 2012). ECM rich lateral facet of human patellar cartilage is shown to have similar Poisson ratio when tested under identical method (Elliott, Narmoneva et al. 2002), although others have shown values to be  $< 0.5$  (Moroni, de Wijn et al. 2006). To further confirm the behavior of CG scaffolds, three different sample preparations were utilized by varying freezing temperature and composition of the polymer (Moshfeghian, Tillman et al. 2006). Temperature at which CG solution was frozen moderately affected the Poisson's ratio. The scaffolds frozen at  $-80^{\circ}\text{C}$  had lower Poisson's ratio compared to scaffolds frozen at  $-20^{\circ}\text{C}$ . However, no significant changes in Poisson's ratio were observed when the polymer concentrations were increased, suggesting the influence of intrinsic property of the polymers rather than pore architecture.

### **3.4.3 Darcy to Brinkman transition in the flow-through bioreactor.**

Darcy's equation is widely utilized in tissue engineering and biomechanics to describe flow through porous scaffolds below a Reynolds number of one (Jacob 1988). Some have proposed using Darcy's equation for determining permeability and monitoring bone without defining the flow configurations within the bioreactors (Ochoa, Sanz-Herrera et al. 2009). Using Equation (3.6), the average Reynolds numbers were found to be less than one for all flow rates except at 25mL/min. However, the maximum Reynolds number exceeded one for an inlet flow rate of 10mL/min, indicating the need to test alternative equations to Darcy's. One has to consider the non-linear terms using Forchheimer equation when the local Reynolds numbers are in the order of 100 or greater. Quadratic Forchheimer term is used to account for the observation of eddies in those Reynolds numbers. Since the local Reynolds numbers were less than 100 but greater than one, the Brinkman equation was used to account for viscous effects at the boundary surface. Differences in predicted pressure drop were observed between the simulations performed using

Darcy's equation and Brinkman equation. Pressure drop with Brinkman equation were higher than that with Darcy's equation and the deviations increased with flow rate. The Laplacian form of the viscous term in the Brinkman equation accounts for the no-slip boundary condition. Increased pressure drop due to the consideration of frictional losses in the boundary suggest the need for using the additional viscous term. Hence, Brinkman equation was used for all the subsequent analyses in this study.

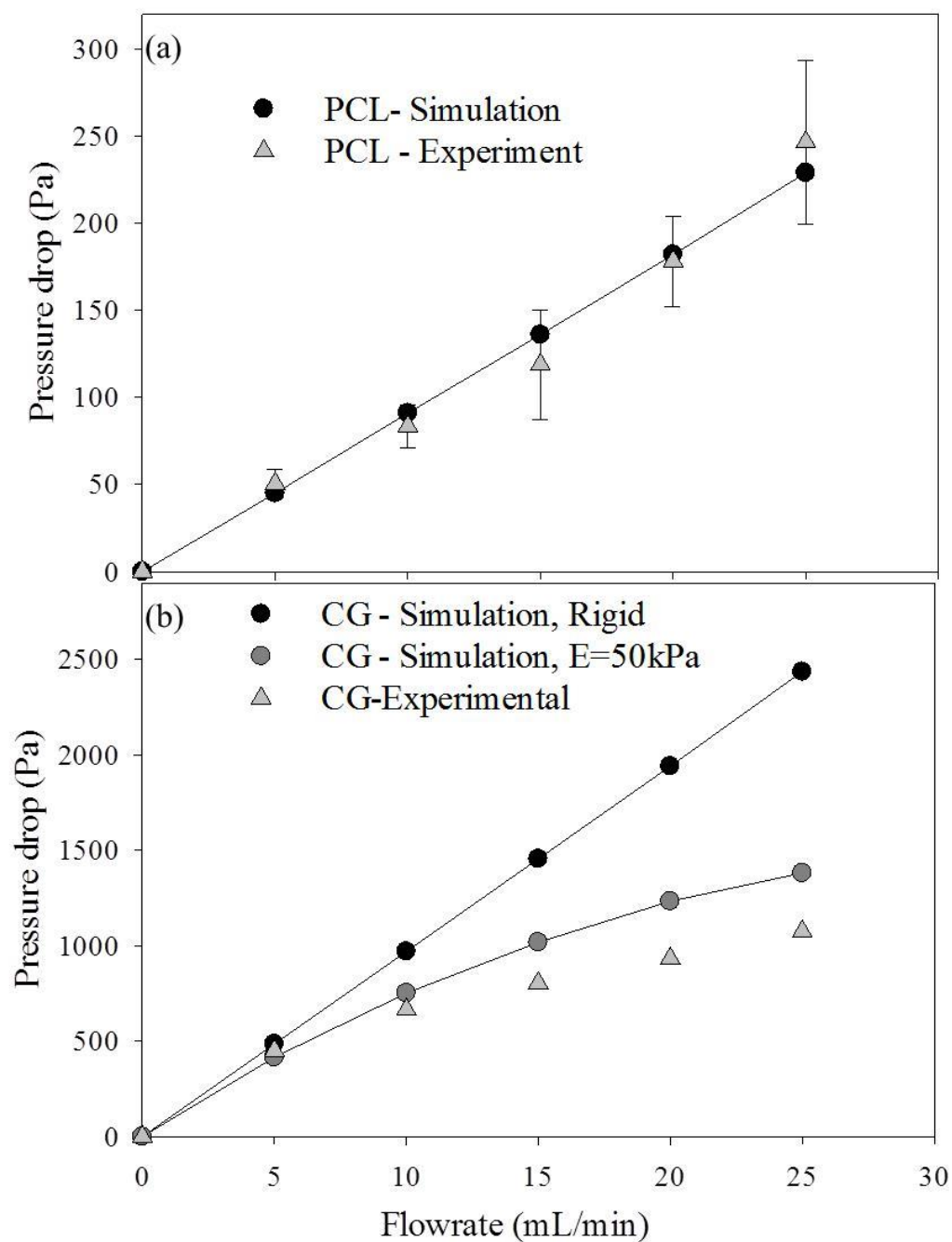
#### **3.4.4 Validation of permeability equation.**

The theory of poroelasticity is broadly used by implementing Darcy's equation in bone modeling (Sanz-Herrera, Garcia-Aznar et al. 2009; Dias, Fernandes et al. 2012) or biphasic mechanics of cartilage (Kim, Guilak et al. 2008). Based on the initial studies which showed deviations in pressure drop predicted by Brinkman equation to Darcy's equation in flow-through bioreactor, structural deformation studies were performed by combining Brinkman equation and structural mechanics in a coupling process. To configure and test the pressure transducer, pressure drop obtained across the bioreactor without the scaffold from experiments were compared to the simulation predictions. Experimental pressure drop across the bioreactor remained nearly constant without the scaffold, similar to simulation results with the exceptions of minor losses due to fittings.

Experiments were performed by placing the scaffolds in the bioreactor. Due to the increased resistance in the path of fluid flow, increased pressure drop was observed, which increased linearly with flow rate as expected by the Brinkman equation with the assumption of scaffold as a rigid structure. Pressure drop obtained for PCL scaffolds (**Figure 3.4a**) were consistent in magnitude and trend to that of the simulation results. This suggested the validity of the approach and the permeability equation for rectangular pores. Also, pressure drop observed in CG scaffolds (**Figure 3.4b**) were significantly higher than that in PCL scaffolds due to ten-fold

reduction in permeability. In addition, pressure drop values from experiments agreed with the simulation for CG scaffolds at flow rates less than 10 mL/min, demonstrating the applicability of the cylindrical pore assumption for freeze dried scaffolds (Podichetty, Dhane et al. 2012). However, for flow rates higher than 10 mL/min, pressure drop values were compared qualitatively by adjusting its mechanical properties as discussed below. Similar equation has to be validated for fibrous scaffolds formed by electrospinning (Hong and Madihally 2011) or other methods.

In this study, for the set of operating conditions average pore size and shape were used to calculate permeability, and approach was validated using experimental results obtained using PCL scaffold. Some have suggested a porosity-based estimation of permeability (Koponen, Kataja et al. 1997) using tortuosity relationship for porosity (Shimko, Shimko et al. 2005). Others have estimated the permeability using pore size distribution by coupling with imaging (Dias, Fernandes et al. 2012). Alternatively, permeability is expressed using Kozeny-Carman definition based on pore characteristics (Swartz, Kaipainen et al. 1999) and values for some soft tissues are also summarized (Wiig and Swartz 2012). Permeability is defined independent of the fluid viscosity so that it could be utilized for any fluid used in perfusion.



**Figure 3.4** Comparison of experimental pressure drop to simulated pressure drop across the flow-through bioreactor for a) PCL scaffolds and b) CG scaffolds. Experiments were performed by placing each type of scaffold of appropriate dimension in the flow-through bioreactor.



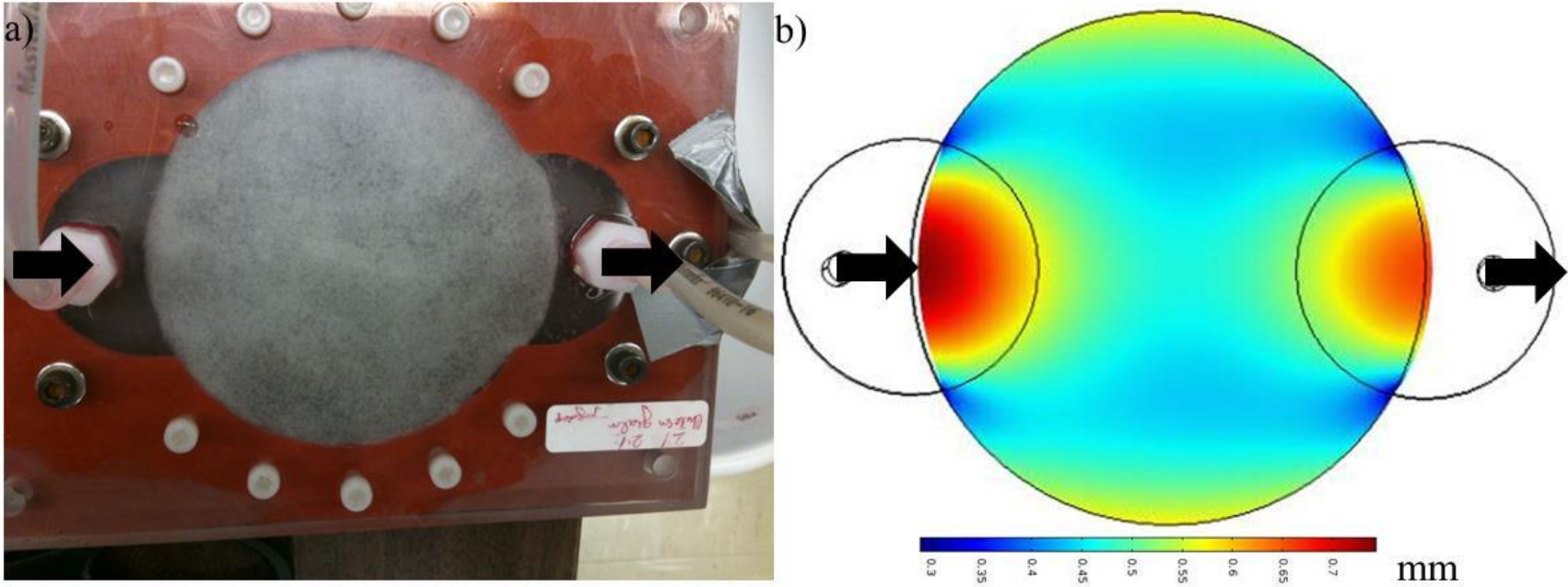
Translating permeability estimation to pore size, pore shape, and number of pores per unit area of the scaffold helps in directly using the data from scaffold microstructure analysis rather than needing additional porosity measurement and selecting an arbitrary equation. In addition, modeling the permeability using the pore architecture also provides insights into the dynamics of matrix deposition when monitoring the permeability using pressure drop and flow rate. Nevertheless, exploring alternative pore architecture such as pore throat model to capture the scaffold geometry could also help in understanding the importance of pore shape. The applicability of such models must be tested experimentally.

### **3.4.5 Validation of fluid flow-structural mechanics coupling approach.**

Experiments performed using PCL scaffolds showed low deformation compared to CG scaffolds at the same flow rates. The PCL scaffolds have higher ultimate stress, ultimate strain, and elastic modulus relative to CG scaffolds. To account for scaffold deformation in simulations, fluid flow and structural mechanics were coupled and the pressure drop was obtained. These simulation results for PCL scaffolds were identical to that of experiments, and simulation results showed no significant deformation at the measured flow rates. However, CG scaffold had observable deformation at flow rates 10mL/min or above (**Figure 3.4**). At flow rates higher than 10mL/min, CG scaffolds showed significant deformation and long term exposure at 25mL/min destroyed the scaffolds. Since simulations assume linear elastic conditions, Poisson's ratio has to be  $<0.5$  for poroelasticity to be applicable which is not true for CG scaffolds. The experimental pressure drop showed deviation from the linear trend after 10mL/min with an  $R^2$  value of 0.92. As shown by the simulation results, these deviations are due to structural deformations at higher flow rates rather than fluid eddies which would have increased the pressure drop.

In any case, pressure drop was analyzed for a non-rigid material with linear elastic properties in the range of CG scaffolds. For this purpose, simulations were initially performed using an elastic

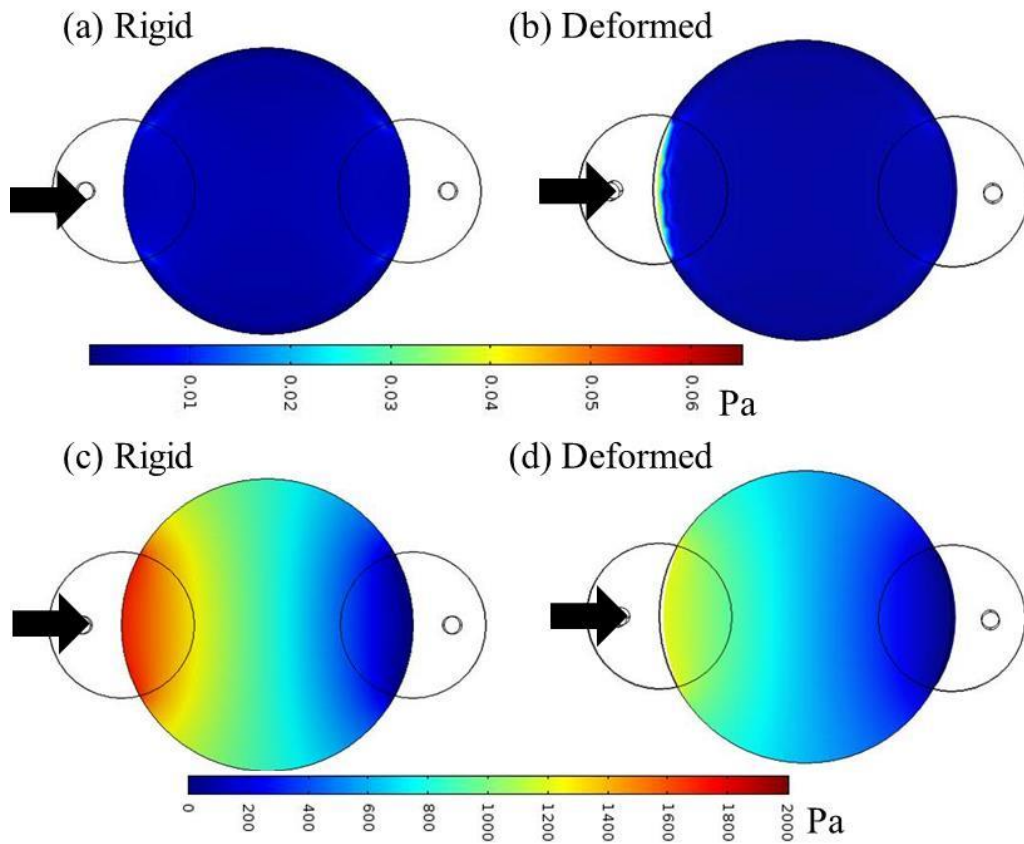
modulus value of 2kPa, and a Poisson's ratio of 0.3. However, simulations did not converge probably due to large deformation and inversion of mesh elements. Hence, simulations were performed using a higher elastic modulus value of 50kPa (selected based on convergence), and a Poisson's ratio of 0.3. Despite the differences in E value and Poisson's ratio from the actual CG scaffolds, trend in the pressure drop resembled that of the experimental results. At the same flow rate, displacement profiles were similar (**Figure 3.5**) to that in the experiments; higher displacements were observed at the beginning and towards the end of the scaffold. A maximum deformation of 2.9mm was observed from experiments using CG, while CFD predicted a maximum deformation of 1.6mm. The deviation between the experimental and simulation results at the entrance of the scaffold could be attributed to higher elastic modulus and lower Poisson's ratio used for CFD predictions. Overall, the fluid flow- structural mechanics coupling method can be used to predicted pressure drop in deformable scaffolds. This information can be used to characterize applicability of a scaffold in a particular bioreactor configuration at a specific flow rate. For example, use of CG scaffold in flow-through bioreactor at flow rates 10 mL/min or higher may be impractical.



**Figure 3.5** Comparison of scaffold deformation profiles between experiment and simulation a) Photograph of CG scaffold at 20mL/min flow rate in a flow-through bioreactor. b) Simulated profile of deformation in a CG scaffold with elastic modulus of 50kPa and Poisson's ratio of 0.3 at 20mL/min flow rate. Arrows indicate flow direction.

### 3.4.6 Effect of scaffold deformation on shear stress.

Previous simulations with the assumption of rigid structures had indicated the inlet and outlet shapes allowed uniform shear stress in the region where scaffolds were situated (Devarapalli, Lawrence et al. 2009). Since the shear stress influences the phenotypic characteristics of cells significantly, effect of deformation on shear stress profiles were studied within the scaffold.



**Figure 3.6** Altered hydrodynamic shear stress (a-b) and pressure drop (c-d) profiles in CG scaffold due to deformation at 20mL/min flow rate, with an elastic modulus of 50kPa and Poisson's ratio of 0.3. Rigid structure results are obtained using flow through porous media simulations without coupling it with structural mechanics and dynamic mesh. Arrows indicate flow direction.

These results showed (**Figure 3.6**) the shear stress near the entrance region to be nearly three times higher than that in the other regions. In case of rigid simulation results showed uniform shear stress but about three times lower than the entrance region of the deformed scaffold. Although area of this non-uniform shear stress region is small in the current study, this deviation would be significant if the scaffold size is reduced to that typically evaluated in various bioreactors. At the same flow rate the pressure drop difference was also significant between the deformed-simulation (1.7kPa) to the rigid simulation (1.4kPa), although the profile appeared similar. Simulations were based on the conservation of momentum principle. As a result, increase in fluid flow rate increases the momentum in the fluid, which correlates to increase in mechanical loading on the scaffold. Reduced pressure drop across the bioreactor with increased flow rate has to be accounted by other types of forces such as increased hydrodynamic shear stress at the entrance of the scaffold. Overall, this suggested that the distribution of mechanical stresses is not uniform. Since level of applied mechanical stresses significantly influences the regenerative process, non-uniformity in stresses would lead to decreased quality in the regenerated tissue.

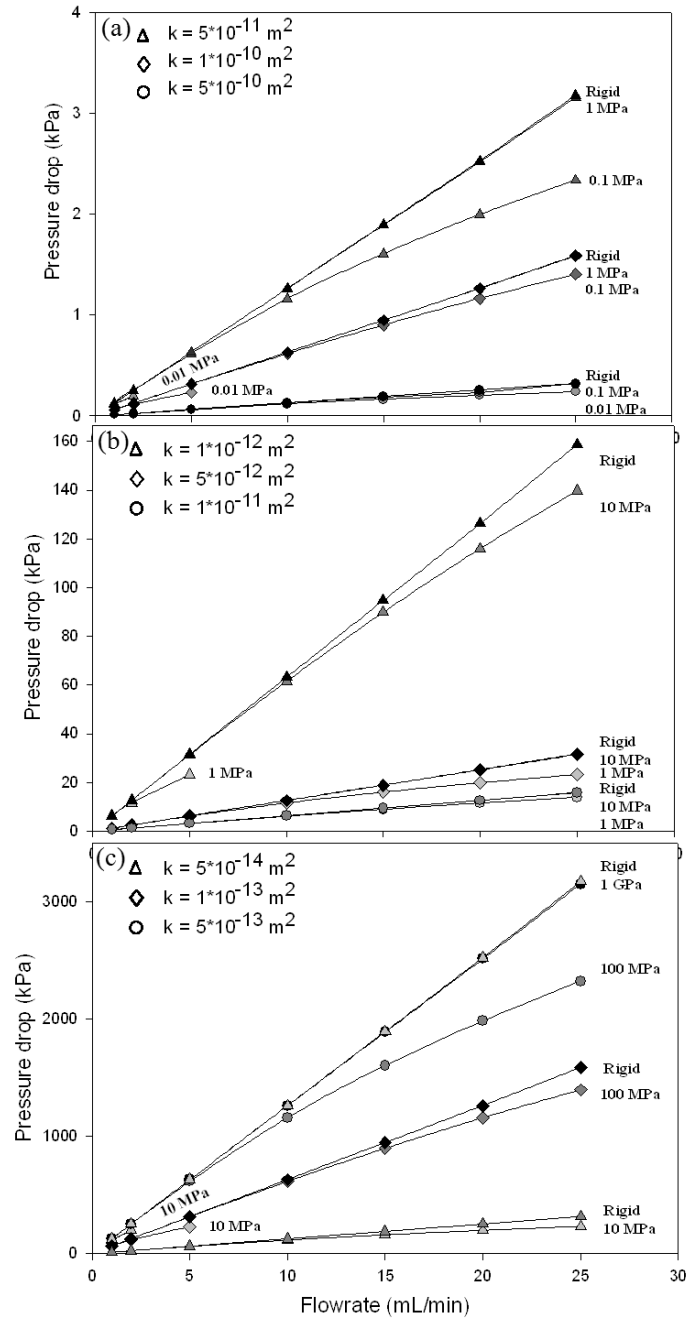
Other studies have utilized three dimensional images obtained from micro-computed tomography to integrate porous structure heterogeneity and understand the local shear stresses (Cioffi, Boschetti et al. 2006). As the image sizes are significantly larger, microscopic models are used along with micro-Finite Element or Lattice Boltzmann codes. This has resulted in significant discrepancy in estimated local shear stresses between the microscopic models to that observed in macroscopic models (Cioffi, Boschetti et al. 2006). Further, these studies lack experimental evidence to show which approach is better. However, use of such techniques to analyze polymeric scaffolds with no minerals has been limited by the resolution of the images. Novel techniques using various contrast agents have been explored to improve image resolution.

Further studies are necessary to understand the importance of these pore heterogeneity in predicted pressure drop.

#### **3.4.7 Effect of permeability on pressure drop and deformation.**

Many manufactured scaffolds possess a permeability ranging from  $10^{-8}\text{m}^2$  to  $10^{-12}\text{m}^2$  (Dias, Fernandes et al. 2012) while permeability of many tissues typically from  $10^{-12}\text{m}^2$  to  $10^{-15}\text{m}^2$  (Swartz and Fleury 2007). Thus, permeability of the porous scaffolds is expected to decrease during tissue regeneration due to the assembly of *de novo* ECM, cell growth, and scaffold degradation. These changes significantly alter the flow dynamics and nutrient distribution which ultimately determine the quality of the regenerated tissue. *A priori* knowledge of how the pressure drop would change with decreased permeability is useful to monitor tissue growth. In rigid structures, one could use Brinkman equation to calculate the pressure drop at various permeabilities, which will show an inverse proportionality to  $k$  at constant flow rate. In a flow-through bioreactor design, flow rate has to be increased to accommodate the increased resistance to flow if the scaffold permeability is reduced to ensure sufficient nutrient replenishment. This increase in flow rate increases the force impinged on the scaffold further deforming the scaffold structure. The minimum nutrient flow rate can be estimated using the rate of consumption of a nutrient at the inlet condition and then relating the consumption rate to the space time and the required concentration gradient for transport inside the cells (Devarapalli, Lawrence et al. 2009).

Simulations were performed by sequentially decreasing the permeability from  $10^{-10}\text{m}^2$  to  $10^{-14}\text{m}^2$  to understand how pressure drop changes due to scaffold deformation for non-rigid scaffolds. Reduction in permeability had a significant effect on deformation, since the fluid stress on the scaffold increases with decreases in permeability (**Figure 3.7**).



**Figure 3.7** Effect of scaffold permeability and elastic modulus on pressure drop at various flow rates a) Permeability range of  $5 \times 10^{-10} \text{ m}^2$  to  $5 \times 10^{-11} \text{ m}^2$ , b) Permeability range of  $1 \times 10^{-11} \text{ m}^2$  to  $1 \times 10^{-12} \text{ m}^2$ , c) Permeability range of  $5 \times 10^{-13} \text{ m}^2$  to  $5 \times 10^{-14} \text{ m}^2$ . Also shown are simulations with various elastic moduli of the scaffold (from 10kPa to 100000kPa) at constant permeability.

When the scaffold permeability was in the range of  $10^{-12}\text{m}^2$ , a difference in the pressure drop was observed between scaffolds with an elastic modulus of 10MPa to that of a rigid scaffold. However, scaffold deformation was negligible even at 1MPa elastic modulus when the scaffold permeability was near  $10^{-10}\text{m}^2$ . The deviations are significant when the permeability approaches that of native tissues. Thus when pressure drop is used as a non-invasive approach to monitor tissue growth, considering the deformation of the scaffold is important. Nevertheless, measurement of pressure drop in real time at a certain flow rate can be used as a non-invasive way to monitor tissue growth even in soft tissues.

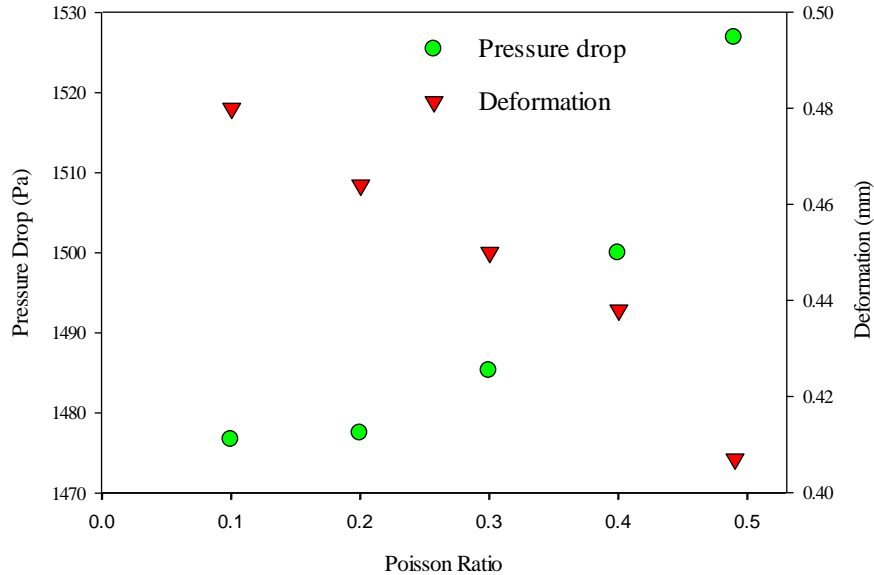
#### **3.4.8 Effect of scaffold mechanical properties on structural deformation.**

Various biomaterials have been explored in tissue engineering applications with unique chemical and mechanical properties. Scaffolds with a broad range of elastic moduli from 10MPa to 1200MPa (Goulet RW 1994) for hard tissues and 0.04MPa to 350MPa (Hayashi 2003) for soft tissues have been explored. Simulations were performed for a broad range of elastic modulus (0.01MPa to 100MPa) to understand the effect of elastic modulus on scaffold deformation. In addition, effect of Poisson's ratio in the linear range (0.1 to 0.49) was also tested. Changes in elastic modulus inversely affected the deformation in the scaffold (**Figure 3.7**). Based on the conservation of momentum principle, the applied mechanical loading is constant at constant flow rate. For higher flow rates, mechanical stresses increase proportionally. Hence, scaffolds with lower elastic modulus showed more deformation relative to scaffolds with higher elastic modulus. If scaffolds with a lower elastic modulus are used, considering the flow configuration while designing the bioreactor is critical. Simulation results in **Figure 3.7a** encompasses a broad range of properties represented by salt leached scaffolds ( $E = 600\text{kPa}$ ,  $k = 7 \times 10^{-10} \text{ m}^2$ ) used in this study. However, CG scaffolds ( $E = 9\text{kPa}$ ,  $k = 7.27 \times 10^{-11} \text{ m}^2$ ) have a high Poisson's ratio ( $>0.5$ ), and low elastic modulus value. Convergence issues were experienced near those numbers and the



pressure drop line with  $E=10\text{kPa}$  and  $k=5\times 10^{-11}\text{ m}^2$  in **Figure 3.7a** was the closest that represented the properties of CG scaffolds.

The effect of Poisson's ratio on pressure drop was evaluated at  $20\text{mL}/\text{min}$  flow rate using values of PCL scaffold permeability and elastic modulus. Increase in Poisson's ratio decreased the scaffold deformation and the pressure drop approached that of the rigid structures (**Figure 3.8**). From Equation (3.9), increase in Poisson's ratio at constant elastic modulus would decrease shear modulus. Hence, the shear strain would increase at a constant flow rate. Thus one has to assess the strain distribution in an alternative direction. Since the scaffold thickness is very small ( $0.2\text{ cm}$ ), we may not see a significant alterations between conditions in the current study. However, when axial-flow bioreactors are used to perfuse thicker scaffolds (Azuaje 2011), considering the effect of Poisson's ratio on shear stress is important. Similarly, simulations showed no dependency of scaffold density on pressure drop.



**Figure 3.8** Effect of Poisson's ratio on pressure drop and deformation. Simulations were performed at  $20\text{mL}/\text{min}$  flow rate, with an elastic modulus of  $600\text{kPa}$  and  $7\times 10^{-10}\text{ m}^2$  permeability (that of PCL scaffolds).

### **3.5 Acknowledgements**

I would like to thank Mr. Lukasz Witek for assistance with SEM imaging.

## CHAPTER 4

### MODELING PRESSURE DROP USING GENERALIZED SCAFFOLD CHARACTERISTICS IN AN AXIAL-FLOW BIOREACTOR FOR SOFT TISSUE ENGINEERING

#### **4.1 Introduction**

Axial-flow bioreactors where fluid passes through the scaffold thickness in the axial direction have received significant attention due to several unique advantages such as convection-driven nutrient distribution and ability to operate at high flow rates. These bioreactors have been found to support liver cells (Leclerc, Sakai et al. 2004), cardiac cells (Dvir T 2006), bone regeneration (Azuaje 2011), and abdominal wall (Pu, Rhodes et al. 2010). However, fundamental aspects such as nutrient permeability, shear stresses, and structural integrity of scaffolds are not established during tissue regeneration. As tissue regenerates transiently, porous characteristics change due to cell proliferation, deposition of new extracellular matrix, and degradation of the porous scaffold. These changes affect the transport characteristics, in particular resistance to medium growth. For example, a prior knowledge of pressure drop at various scaffold permeabilities is useful in non-invasive monitoring and understanding the regenerative process. With recent advances in CFD it is now possible to analyze the effects of flow, scaffold pore characteristics, mechanical properties, and consumption kinetics on tissue regeneration for a particular bioreactor design (Patrachari, Podichetty et al. 2012).

Some previously studies have tested the possibility of calculating permeability, of salt leached PCL scaffolds (rectangular pores), and freeze dried CG scaffolds (circular pores), using pore size and shape in flow-through bioreactors (Podichetty and Madihally 2014). The effect of scaffold mechanical properties was studied by coupling fluid flow in the bioreactor with structural mechanics of the scaffold using a dynamic mesh. In this study, the analyses was extended to i) axial-flow bioreactors optimized for uniform nutrient and shear stress distribution (Bhaskar 2012), and ii) electrospun scaffolds, which generate fibrous scaffolds mimicking various *in vivo* microenvironments. A co-axial electrospinning technique was used to obtain thicker fibers with high porosity (~70%). The simulation predictions were validated using experimental measured pressure drops. The simulation results were extended to various permeabilities, elastic moduli, and Poisson's ratios. These results validated the utility of analytical models based on pore configurations to determine permeability of the scaffold, facilitating a non-invasive technique to monitor pressure drop in real time during tissue growth.

## **4.2 Materials and methods**

### **4.2.1 Preparation of porous scaffolds**

PCL-CA electrospun scaffold: Polycaprolactone (PCL 43kDa,  $M_w=43,000-50,000$ ) was obtained from Polysciences (Warrington, PA). Cellulose acetate (CA, 30 kDa), octane 99%, acetone 99.9%, and 1-2 dioxin were obtained from Sigma Aldrich Chemical Co. (St. Louis, MO). Chloroform and ethanol (200 proof) was obtained from Aaper Alcohol and Chemical Company (Shelbyville, KY). Other reagents were purchased from Fisher Scientific (Waltham, MA) and used without further purification. PCL-CA fibrous structures with a diameter of 10cm and with two different thicknesses, 0.1cm and 0.2cm were fabricated by coaxial electrospinning. The setup consisted of two syringe pumps (74900 series, Cole-Parmer Instrument Company, Vernon Hills, IL) for pumping the shell and core solutions independently, BD 10mL syringe (Luer-Lok

Tip; Becton Dickinson and Company, Franklin Lakes, NJ), needle tips, high voltage power supply (ES30P-5W/DAM, Gamma high Voltage Research, Ormond Beach, FL), earth grounding, and a collection mandrel. PCL solution was formed in 9:1 (v/v) chloroform-methanol mixture and CA solution was formed in 2:1 (v/v) acetone-dioxin mixture. Syringe containing core spinning CA solution was connected to the spinneret using a 30cm long PTFE tubing (Sigma Aldrich, St. Louis, MO). The core spinneret inner diameter was 2.1mm and pumped at a flow rate of 0.5mL/h. Syringe containing shell spinning PCL solution was connected to the spinneret using a 10cm long plastic tube. The shell spinneret inner diameter was 3mm and the flow rate was 2mL/h. The distance from spinneret to ground collector was set at 8cm. A 17kV voltage was applied between the needle and the conductive collector. The temperature was 25°C and humidity was at 55% RH. Fibers aligned randomly were collected on a flat collector plate.

Chitosan-Gelatin scaffold: Chitosan (190-310kDa MW, 85% degree of deacetylation), porcine skin gelatin type-A (Bloom 300 or 75 kDa), and glacial acetic acid were obtained from Sigma Aldrich Chemical Co. (St. Louis, MO). CG scaffolds of 10cm diameter with thickness 0.2cm were fabricated using controlled rate freezing and lyophilization technique (Iyer, Walker et al. 2012). In brief, 2%-2% (wt/v) CG solution was prepared in 0.5M acetic acid using deionized water. A well of known diameter was prepared on Teflon sheet using silicon glue and the CG solution was poured in the well and was frozen at -80°C overnight. On top of the frozen solution, a wet paper towel was placed to remove the skinny layer and the assembly was refrozen. Prior to lyophilization (or sublimation), paper towel containing the skinny layer was peeled off. Frozen solutions were lyophilized overnight using bench top Virtis freeze dryer (Gardiner, NY). Prior to using the scaffolds, acetic acid was removed by incubating with ethanol for ten minutes and washed four times with PBS.

#### **4.2.2 Evaluation of mechanical properties.**

Tensile tests were performed under physiological conditions (PBS at pH 7.4 and 37°C) using Instron 5542 (INSTRON, Canton, MA) and a custom-built environmental chamber (Lawrence, Maase et al. 2009). In brief, samples were cut into 5cm×1cm strips. The thickness was measured using a digital caliper. Scaffolds were strained to break at a cross head of 10mm/mm. Data collected using Merlin (INSTRON, Canton, MA) software was exported to MS Excel and analyzed for elastic modulus from the slope of stress-strain plot in the linear region. Experiments were repeated at least four times and the average and standard deviations were calculated.

Poisson's ratio was determined under hydrated conditions (PBS solution maintained at 37°C), using the setup described previously (Podichetty and Madihally 2014). In brief, two INSTRON® screw grips were attached to an adjustable steel frame and a scale was attached to one of the screw grips. Scaffolds cut into 7cm×1cm strips were attached. The setup was placed inside a container filled with PBS. Sample was stretched along its length in increments of predetermined longitudinal extensions using an adjustable knob located on the back of the frame. At those extensions, changes in width were measured using a digital vernier caliper. Knowing the initial length and width, longitudinal ( $\epsilon_{\text{long}}$ ) and transverse ( $\epsilon_{\text{trans}}$ ) strains were calculated and plotted. The strain ranges were restricted to the linear region based on tensile testing. Poisson's ratio was determined as the slope of the line passing through the origin. Experiments were performed in triplicates and the mean and standard deviation were calculated.

#### **4.2.3 Estimation of scaffold permeability.**

Scaffold permeability depends on geometrical features. An analytical approach such as the Kozeny-Carmen equation expresses the relation between permeability and pore properties (Pennella, Cerino et al. 2013). The PCL-CA scaffolds fabricated using electrospinning technique produces fibrous structures. Reported permeability equations require the fiber size, porosity and

arrangement of fibers (Jackson and James 1986; Koponen, Kandhai et al. 1998). To characterize fiber size and porosity, dry scaffolds were examined using a scanning electron microscope (SEM, Joel JSM 6360) at an accelerating voltage of 10kV after gold sputter coating at 40mA, similar to previous publication (Lawrence, Maase et al. 2009). Fiber diameter( $d$ ) or radius ( $r$ ) and free space per unit area were quantified using at least four images per sample. Assuming isotropic distribution of fibers, porosity ( $\epsilon_p$ ), was calculated as the ratio of open pore area to the total image area. The fiber volume fraction ( $\phi$ ) was calculated as  $(1-\epsilon_p)$ . For flow through randomly oriented fibers, the permeability was calculated using the equation (Jackson and James 1986)

$$\kappa = \frac{3r^2}{20\phi} (-\ln \phi - 0.931) \quad (4.1)$$

where  $r$  is the fiber radius and  $\phi$  is the volume fraction of the solid. The permeability of the scaffold,  $k$ , is defined independent of the fluid viscosity so that it could be utilized in different flow conditions. Another approach for calculating permeability of large random fibers is based on the Lattice-Boltzmann method. In this case, the permeability is given by the equation (Koponen, Kandhai et al. 1998).

$$\kappa = \frac{5.55 * r^2}{(e^{10.1(1-\phi)} - 1)} \quad (4.2)$$

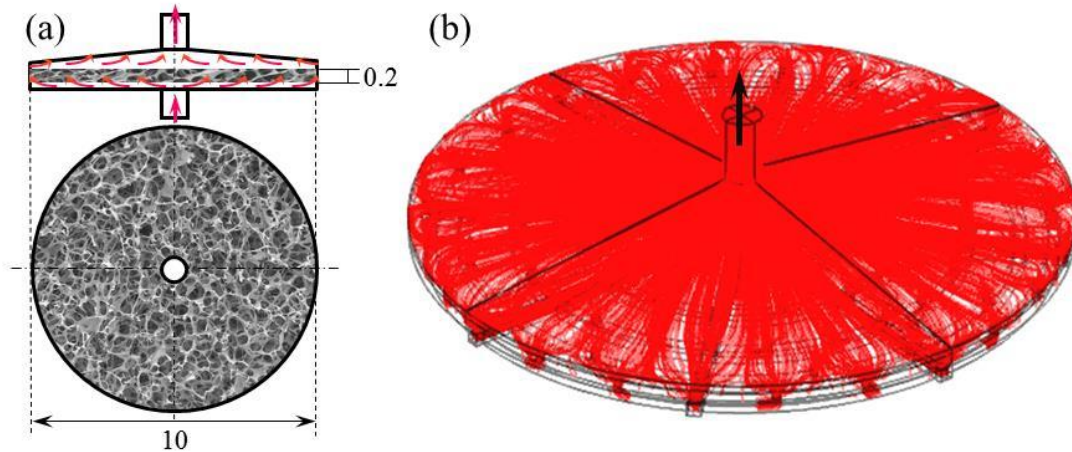
Permeability of freeze dried CG scaffold was calculated as described previously (Podichetty and Madihally 2014). In brief, micrographs were characterized for pore area, size, and number. Permeability was calculated using the equation

$$\kappa = \frac{\pi}{128} n_A d^4 \quad (4.3)$$

where  $d$  is the pore diameter and  $n_A$  is the number of pores per unit area. The circularity factor or shape factor for CG scaffolds was measured. Since the circularity factor was  $>0.8$ , pore geometry was considered cylindrical.

#### 4.2.4 Pressure drop measurement

An axial-flow bioreactor that can hold 0.2cm thick and 10cm diameter scaffold was constructed in-house (**Figure 4.1a**). These features included uniform distribution of fluids based on the simulation profiles obtained using the methodology described below (**Figure 4.1b**).



**Figure 4.1** Axial-flow bioreactor flow pattern. (a) Schematic showing the configuration and dimensions in cm. (b) Three dimensional streamlines at 25mL/min through the bioreactor with 0.2cm thick electrospun PCL-CA scaffold. Arrows indicate the direction of media flow.

Experiments were performed at flow rates from 5mL/min to 25mL/min with 5mL/min increments following the procedure described previously (Podichetty, Dhane et al. 2012). In brief, the scaffold was placed in the bioreactor, which was attached to a flow system consisting of a fluid reservoir, a variable speed Masterflex L/S peristaltic pump (Cole-Parmer, Vernon Hills, IL), an in-line physiological pressure transducer (Capto SP844, Skoppum, Norway), and a waste reservoir. Data from the pressure transducer were retrieved using Chart™ 5 for Windows via Powerlab/4SP System (ADI Instruments, Inc., Colorado Springs, CO). Data were recorded after allowing the bioreactor to reach steady state for every flow rate, based on the output signal (and



four times the space time i.e., the ratio of volume of the bioreactor to volumetric flow rate). To obtain pressure drop across the bioreactor, experiments were performed with and without the bioreactor in the flow system. The difference in pressure reading between these settings was attributed to the pressure drop across the bioreactor. Experiments were performed in quadruples. The mean and standard deviation of the pressure drop were evaluated at each flow rate.

### 4.3 Computational fluid dynamics modeling

The CFD simulations were performed by computing fluid flow to examine changes in the porous structure using dynamic mesh. A simulation with fluid flow-structural mechanics coupling was setup as described in our previous publication (Podichetty and Madihally 2014). Following conditions and equations were used while performing simulations.

- The effects of gravity were assumed to be negligible relative to the flow rate.
- Pressure at the exit is set to atmospheric conditions with the assumption of running the bioreactor in open loop.
- The viscosity and density of the growth medium were assumed to be that of water.
- Pore size distribution in the scaffold was considered isotropic.

*Bioreactor geometry:* An axial-flow bioreactor that can accommodate a circular scaffold of 10cm diameter and up to 0.2cm thicknesses was drawn using CAD (**Figure 4.1a**). The bioreactor geometry included flow channels and a distributor plate to ensure uniform fluid flow in the scaffold. The bioreactor geometry was divided into porous and non-porous domains. The medium entered through the inlet at the bottom of the bioreactor into the non-porous domain, moved into the porous domain, entered the second non-porous domain prior to exiting the bioreactor. The meshing was performed using free mesh parameters with triangular mesh with a maximum and minimum element size of 0.015m and  $2.8 \times 10^{-5}$ m respectively. This created ~71000 nodes. Increasing the number of nodes altered the pressure drop predictions only by less than 0.2%. Hence, the number of nodes was considered to be optimum for reliable predictions.

Flow equations: The continuity equation and Navier-Stokes was used equation to describe the three-dimensional incompressible, steady Newtonian fluid flow in the non-porous regions are given by

$$\nabla \cdot \mathbf{u} = 0 \quad (4.4)$$

$$-\nabla \cdot \boldsymbol{\tau} + \rho_f \mathbf{u} \cdot \nabla \mathbf{u} + \nabla p = 0 \quad (4.5)$$

where  $\boldsymbol{\tau}$  is the shear stress tensor,  $\rho_f$  is the fluid density,  $p$  is the pressure and  $\mathbf{u}$  is the velocity vector in 3D. The shear stress tensor was calculated using the velocity vector (Lawrence, Devarapalli et al. 2009). The Brinkman equation, which accounts for momentum transport by microscopic shear effects as well as pressure gradients, was used to characterize flow in the scaffold region (porous) region

$$\frac{\eta}{\kappa} \mathbf{u}_s = -\nabla \cdot \left[ \frac{-\boldsymbol{\tau}}{\varepsilon_p} + p \boldsymbol{\delta}_{ij} \right] \quad (4.6)$$

where  $\eta$  is the dynamic viscosity,  $\mathbf{u}_s$  is the superficial velocity vector,  $\varepsilon_p$  scaffold porosity,  $\boldsymbol{\delta}_{ij}$  is the Kronecker delta function  $p$  is the fluid pressure, and  $\kappa$  is the permeability independent of fluid viscosity.

To understand the flow regime, the average and maximum Reynolds numbers within the scaffold were also calculated using the corresponding interstitial velocities and the equation (Podichetty and Madihally 2014),

$$\text{Re} = \frac{u_i}{\eta} \frac{\phi_s D_p}{(1 - \varepsilon_p)} \quad (4.7)$$

where  $\phi_s$  is the sphericity,  $D_p$  is the pore diameter, and  $u_i$  is the interstitial velocity.

Structural mechanics: The initial total load ( $F_T$ ) was calculated by the Navier-Stokes equation with the assumption of scaffold as a non-deformable object. It was used as the load on the boundaries. The fluid load is given by

$$F_T = -n \cdot (-pI + \tau) \quad (4.8)$$

where  $n$  is the normal vector to the boundary, and  $I$  is the identity matrix. The stress experienced by the scaffold due to the fluid pore pressure was calculated by the following equation.

$$\sigma + \alpha_B p_f I = C \varepsilon \quad (4.9)$$

where  $C$  is the elasticity matrix,  $\sigma$  is the Cauchy stress tensor,  $\varepsilon$  is the strain tensor,  $\alpha_B$  is the *Biot-Willis coefficient* (ratio of poroelastic expansion coefficient to drained material compressibility), and  $p_f$  is the fluid pore pressure. For simulation studies,  $\alpha_B$  of 0.95 was assumed for both scaffolds (Podichetty and Madihally 2014), based on the condition  $\alpha_B$  is  $\sim 1$  for soft porous materials, close to porosity for stiff porous materials and zero for solid materials. The linear elasticity matrix was obtained using elastic modulus (E) and the shear modulus (G) values. Poisson's ratio ( $\nu$ ) and elastic modulus were used to calculate the shear modulus (G) using the linear elastic relationship

$$E = 2(1 + \nu)G \quad (4.10)$$

Simulations were performed at flow rates from 0.1mL/min to 25mL/min. The average and maximum interstitial velocities in the porous domain were retrieved from the simulation.

Dynamic mesh: The simulations were performed by coupling fluid flow with structural mechanics using a dynamic mesh (Podichetty and Madihally 2014). In brief, the calculated fluid stress and strain were used to predict mesh displacement based on scaffold elastic modulus, porosity and

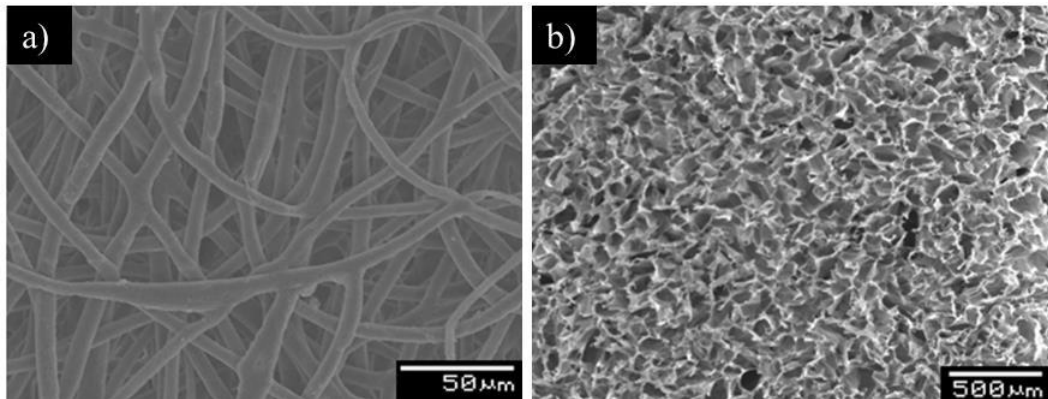
Poisson's ratio. The new deformed mesh was used to predict new pressure profile across the bioreactor using the flow equations described above.

Numerical solvers: The partial differential equations were solved with stationary segregated solver in a three steps process. First, a MULTifrontal Massively Parallel Sparse (MUMPS) direct solver was used to evaluate variables  $x$ ,  $y$ , and  $z$  (de Kloe, van der Steen et al. 2002). Second, a Generalized Minimal Residual (GMRES) (Saad and Schultz 1986) iterative solver was used to evaluate fluid velocity and pressure. Third, a GMRES iterative solver was used to evaluate the mesh displacement. A maximum 200 iterations were performed in the second and the third steps.

## 4.4 Results

### 4.4.1 Scaffold characterization

In this study, PCL-CA and CG scaffolds were used to evaluate pressure drop across an axial-flow bioreactor. Prior to using them in experiments, all scaffolds were observed for cracks, non-uniformity and intactness. The microstructures were characterized for pore size and shape, which varied based on the preparation technique (**Figure 4.2**).



**Figure 4.2** Micrographs of scaffold surfaces orthogonal to the flow direction. a) PCL-CA co-axial electrospun scaffold b) 2% (wt/v)-2% (wt/v) chitosan-gelatin freeze dried scaffold.

The PCL-CA scaffolds fabricated using electrospinning technique produced uniform fibrous structures with no beads. The fibers were randomly oriented and the average fiber diameter was found to be  $8.63 (\pm 0.901)\mu\text{m}$  (**Table 4.1**), much thicker than typically obtained in traditional electrospinning. Further, open area to the total area was found to be  $70(\pm 9)\%$ , which was considered as the scaffold porosity. Using Equation (4.1), permeability value was found to be  $2.54 \times 10^{-12} \text{m}^2$  while that using Equation (4.2) was found to be relatively higher  $5.25 \times 10^{-12} \text{m}^2$ . The permeability of CG scaffold was calculated using Equation (4.3). A permeability value of  $5.27 \times 10^{-12} \text{m}^2$  was obtained which was used in the simulation.

**Table 4.1** Scaffold pore characteristics and mechanical properties and modeling data for CFD simulations

variable	symbol	value
<b>Medium:</b>		
Fluid density (Podichetty, Dhane et al. 2012)	$\rho_f$	$1000 \text{kg/m}^3$
Dynamic viscosity (Podichetty, Dhane et al. 2012)	$\eta$	$0.000615 \text{ Pa.s}$
Biot-Willis coefficient (assumed)	$\alpha$	$0.95$
<b>PCL-CA scaffold:</b>		
Density (measured)	$\rho$	$83.8 \pm 15 \text{kg/m}^3$
Porosity (calculated)	$\epsilon_p$	$0.70 \pm 0.09$
Permeability (calculated) (Equation 4.1)	$k$	$2.54 \times 10^{-12} \text{ m}^2$
Permeability (calculated) (Equation 4.2)	$k$	$5.25 \times 10^{-12} \text{ m}^2$
Elastic modulus (measured)	$E$	$80 \pm 6 \text{kPa}$
Poisson's ratio (measured)	$\nu$	$0.39 \pm 0.04$
Fiber diameter (measured)	$d$	$8.63 \pm 0.901 \mu\text{m}$
<b>CG scaffold:</b>		
Density (measured)	$\rho$	$65 \pm 2 \text{kg/m}^3$
Porosity (measured)	$\epsilon_p$	$0.85 \pm 0.04$
Permeability (calculated) (Equation 4.3)	$k$	$5.27 \times 10^{-12} \text{ m}^2$
Elastic modulus (Ratakonda, Sridhar et al. 2012)	$E$	$9.14 \pm 0.4 \text{kPa}$
Poisson's ratio (Podichetty and Madihally 2014)	$\nu$	$1.2 \pm 0.13$

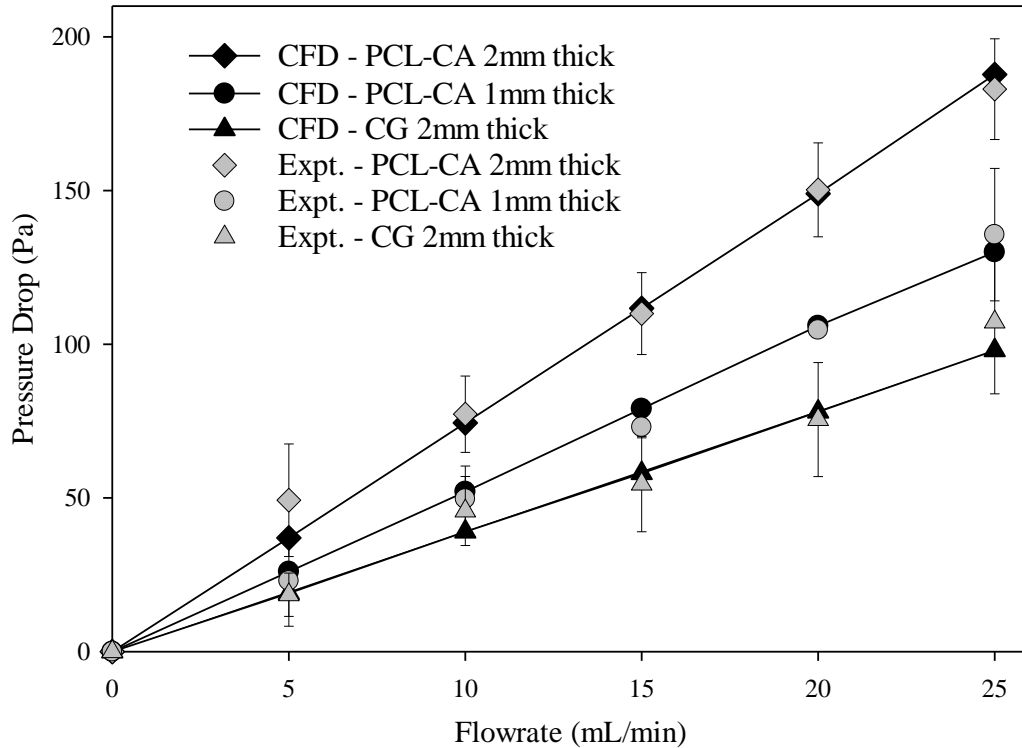
#### **4.4.2 Mechanical Properties of Scaffolds.**

Determining the elastic modulus is important to understand the utility of porous scaffolds in various tissue engineering applications. Further, elastic modulus values are important to determine the fluid flow induced deformation. From the stress-strain experiments conducted in hydrated conditions at 37°C, the elastic modulus of PCL-CA scaffolds were found to be 80(±6) kPa (**Table 4.1**). Some previous studies have reported the elastic modulus of CG scaffold at various concentrations and freezing temperature (Ratakonda, Sridhar et al. 2012). Materials experience dimensional changes in both axial (along the applied load) and transverse (orthogonal to the applied load) directions, which are characterized by Poisson's ratio. To understand the three-dimensional changes in porous scaffolds, Poisson ratio was determined experimentally for the scaffold to be used in pressure drop analyses. The Poisson's ratio for PCL-CA electrospun scaffolds was 0.39(±0.04). This was similar to Poisson's ratio of salt leached PCL scaffolds 0.3, as shown previously (Podichetty and Madihally 2014). The Poisson's ratio of CG scaffold was nearly 1 or > 0.5, considered as non-linear elastic behavior.

#### **4.4.3 Validation of permeability equation**

The permeabilities of electrospun PCL-CA scaffolds were calculated using Equation (4.1) (Jackson and James 1986) and Equation (4.2) that have been explored in evaluating fluid flow through randomly packed fibrous structures. Since these equations are defined independent of growth medium viscosity, they can be used in variety of culture conditions where growth medium is changed. Comparison of the pressure drop across the bioreactor from experiments at corresponding flow rates and scaffold properties showed agreement with the simulation results (**Figure 4.3**). Two different thicknesses of electrospun scaffolds (0.1cm and 0.2cm) were tested to understand these relationships at different thicknesses. Resistance in the path of fluid increased linearly due to the increased scaffold thickness, which manifested in proportional

increase in pressure drop at tested flow rates as expected by the Brinkman equation. Similar agreement with CG scaffolds was observed in magnitude and trend to that of the simulation results (**Figure 4.3**), despite reduced elastic modulus relative to PCL-CA scaffolds.



**Figure 4.3** Pressure drop validation across the bioreactor. Comparison of experimentally obtained pressure drop across the bioreactor to that of simulated with PCL-CA and CG scaffold. Experiments were conducted by positioning each scaffold of appropriate dimensions in the axial-flow bioreactor. Each data point in experiments corresponds to the average of at least three experiments with different scaffolds preparations and error bars correspond to standard deviations.

At permeability values determined by Equation (4.1), pressure drop obtained for both thicknesses of PCL-CA scaffolds agreed with experimental results. Permeability values determined by Equation (4.2) were higher by a factor of two. Both Equation (4.1) and Equation (4.2) use fiber

size and porosity. The scaffold porosity was predicted by determining the open area to the total area in a 2D structural analysis. In addition, other methods for evaluating porosity were also considered. First, the possibility of calculating the porosity based on apparent density of the scaffold was tested (Zhu, Cui et al. 2008). Second, an attempt was made to characterize the 3D structure using micro-computed tomography images (Jones, Arns et al. 2007). However, image resolution was poor, probably attributed to the low density difference between PCL-CA to that of water. Some have attempted to improve the resolution by adding contrast agents (example osmium staining), but the errors associated with these measurements are similar.

#### 4.4.4 Effect of axial-flow configuration on shear stress and pressure drop

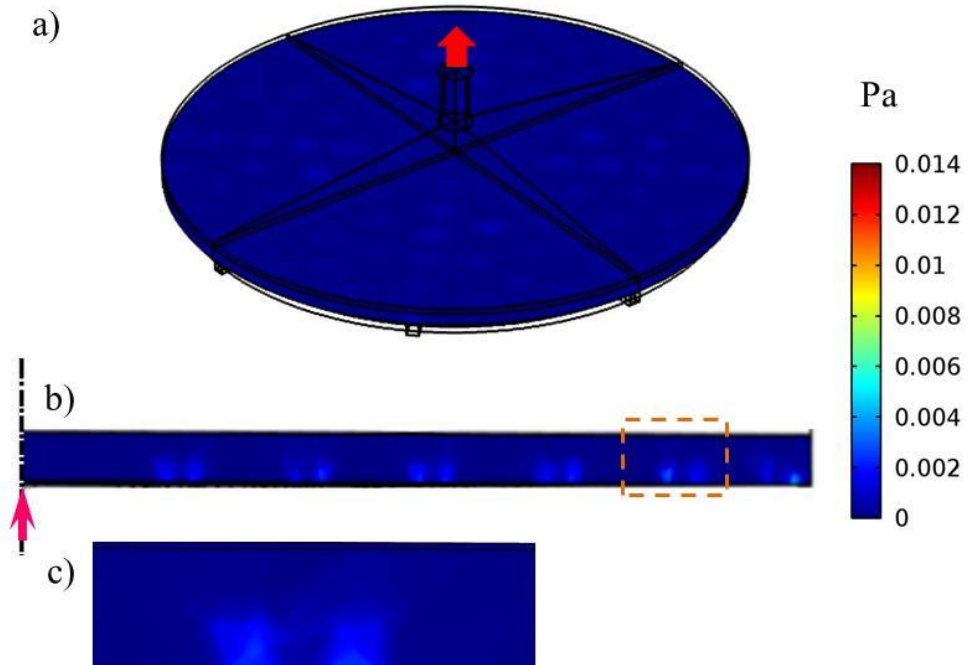
To understand the flow regime in the axial-flow conditions, the average and maximum interstitial Reynolds numbers were calculated from simulations at various flow rates. These values based on pore velocity obtained at various inlet flow rates were determined to be less than one for all flow rates (Table 4.2). One could adapt widely used Darcy's equation in the flow regime where the Reynolds numbers are less than one (Jacob 1988).

**Table 4.2** Reynolds number calculations in the porous scaffold.

<b>Inlet flow rate (mL/min)</b>	<b>Inlet velocity (mm/s)</b>	<b>Average Interstitial velocity (mm/s)</b>	<b>Average Reynolds number</b>	<b>Maximum Interstitial velocity (mm/s)</b>	<b>Maximum Reynolds number</b>
5	2.9	0.009	0.0003	0.40	0.01
10	5.8	0.019	0.0005	0.79	0.02
15	8.7	0.028	0.0008	1.19	0.03
20	11.6	0.037	0.0011	1.58	0.05
25	14.5	0.047	0.0014	1.97	0.06




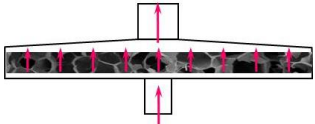
The shear stress distribution was analyzed in the scaffold along the thickness and the diameter. The results showed uniform hydrodynamic shear stress in both directions (radial and angular) for 0.2cm thick PCL-CA scaffold at 25mL/min (**Figure 4.4**).



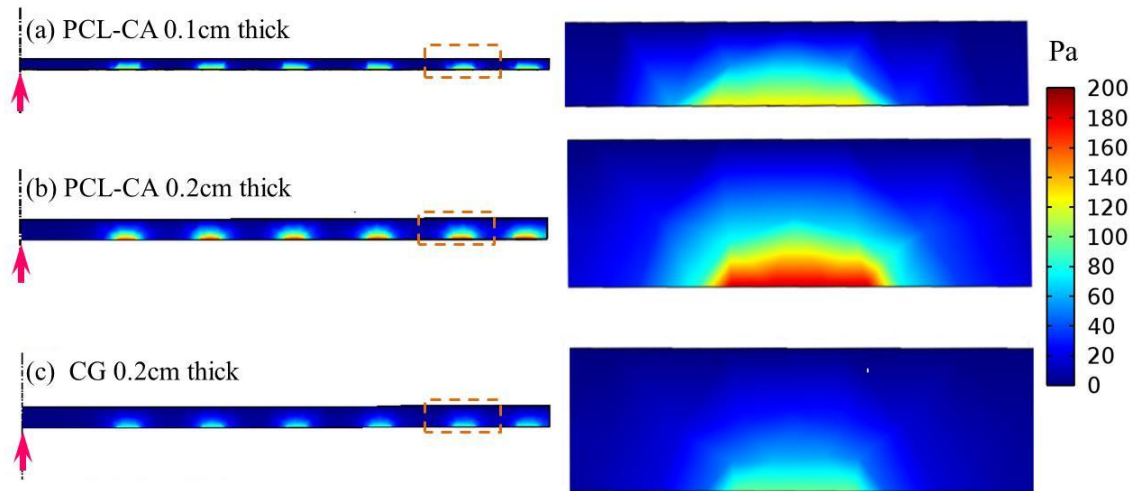
**Figure 4.4** Hydrodynamic shear stress profile for PCL-CA scaffold at 25mL/min inlet flow rate. (a) 3D view (b) Across the scaffold thickness from the center. (c) Magnified view corresponding to the rectangular region shown in (b).

The 0.1cm thick PCL-CA and 0.2cm thick CG scaffolds also showed similar uniform shear stress profiles. Since a distributor was utilized in the bioreactor design, stresses near the entry of fluid into the scaffold were analyzed. Higher shear stresses to a maximum of 0.1dyne/cm<sup>2</sup> (or 0.01Pa) were observed at regions where the medium entered the scaffolds. These values were less by orders of magnitude compared to flow-through bioreactors (**Table 4.3**) at same flow rates (Podichetty and Madihally 2014).

**Table 4.3** Comparison between flow-through and axial-flow bioreactor configurations with same 10cm diameter and 0.2cm thick scaffolds at 10mL/min.

	<b>Flow-through</b>	<b>Axial-flow</b>
Flow configuration	 <p>Through the scaffold diameter</p>	 <p>Through the scaffold thickness</p>
Pressure drop across the scaffold	<p>665(<math>\pm</math>23)Pa</p> <p>High at low flow rates, and significantly increases with flow rate and increases with decreased permeability</p>	<p>46(<math>\pm</math>11)Pa</p> <p>Lower even at higher flow rates, and moderately increases with decreased permeability</p>
Fluid dynamic equation for flow-through porous medium	<p>Since <math>Re_{max} &gt; 1</math>, Brinkman equation is useful to address boundary layer issues</p>	<p>Since <math>Re_{max} &lt; 0.1</math>, Darcy or Brinkman equations can be used</p>
Hydrodynamic shear stress	<p>0.025Pa</p> <p>Higher at the entrance and increases with flow rate</p>	<p><math>5.5 \times 10^{-3}</math>Pa</p> <p>Relatively low even at higher flow rates</p>
Maximum scaffold deformation	<p>0.45mm</p> <p>Higher at lower elastic modulus and higher flow rates</p>	<p><math>9.6 \times 10^{-4}</math>mm</p> <p>Insignificant even with low elastic modulus and high flow rates</p>
Nutrient distribution	<p>Easy to obtain uniform distribution as it is convection-dependent</p>	<p>Ensuring uniform distribution is challenging</p>

The pressure drop profile was evaluated across the scaffold thickness to understand where the maximum pressure drop occurred in the scaffold (**Figure 4.5**).

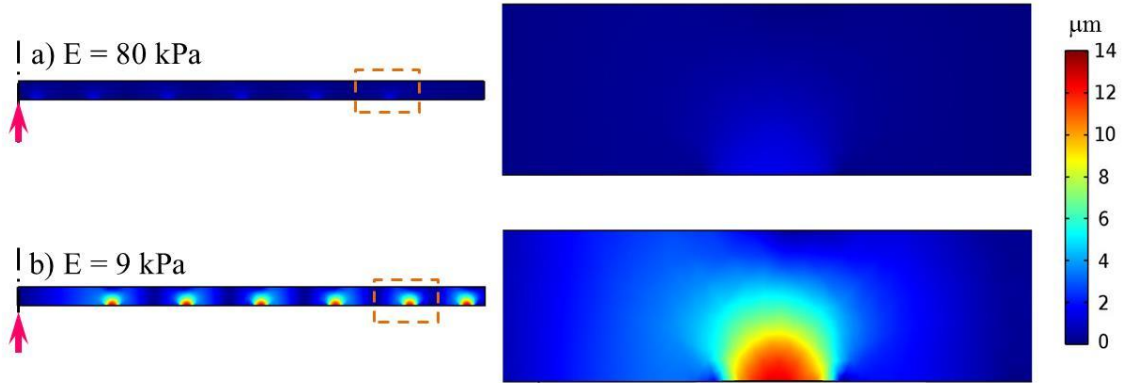


**Figure 4.5** Pressure drop profile at 25mL/min flow rate across the scaffold thickness from the center. Also shown are the magnified views from the corresponding rectangular regions. Arrows indicate the flow direction.

These results showed that much of the pressure drop occurred at the fluid entry region into the scaffold. At similar flow rates, pressure drop across the scaffold decreased significantly in the axial-flow bioreactor (**Table 4.3**) compared to the flow-through bioreactor for CG scaffold with 0.3 Poisson's ratio (Podichetty and Madihally 2014).

#### 4.4.5 Analysis of scaffold deformation

To understand the utility of changed flow configuration, the deformation caused on the scaffold was evaluated in the axial-flow direction. These results showed that PCL-CA electrospun scaffolds (**Figure 4.6**) had deformation in less than 1 $\mu$ m, even at locations where medium entered the scaffolds, suggesting no significant deformation due to higher elastic modulus value and lower pressure drop.



**Figure 4.6** Deformation profile across the scaffold thickness from the center at 25mL/min inlet flow rate for a) corresponding to PCL-CA electrospun scaffold and Poisson's ratio of 0.3. b) scaffold with elastic modulus CG scaffold ( $9\pm 0.4$ kPa) but with a Poisson's ratio of 0.3. Also shown are the magnified views from the corresponding rectangular regions. Arrows indicate the flow direction.

As the Poisson's ratio of CG was greater than 0.5 (beyond the linear elastic range and would not be valid with the governing equations), a value of 0.3 was select to compare the CG scaffold deformation profile between the axial-flow and flow-through configuration from the previous publication (Podichetty and Madihally 2014). The flow-through bioreactor showed significantly higher (**Table 3**) deformation in the scaffold relative to axial-flow bioreactors at same inlet flow rates.

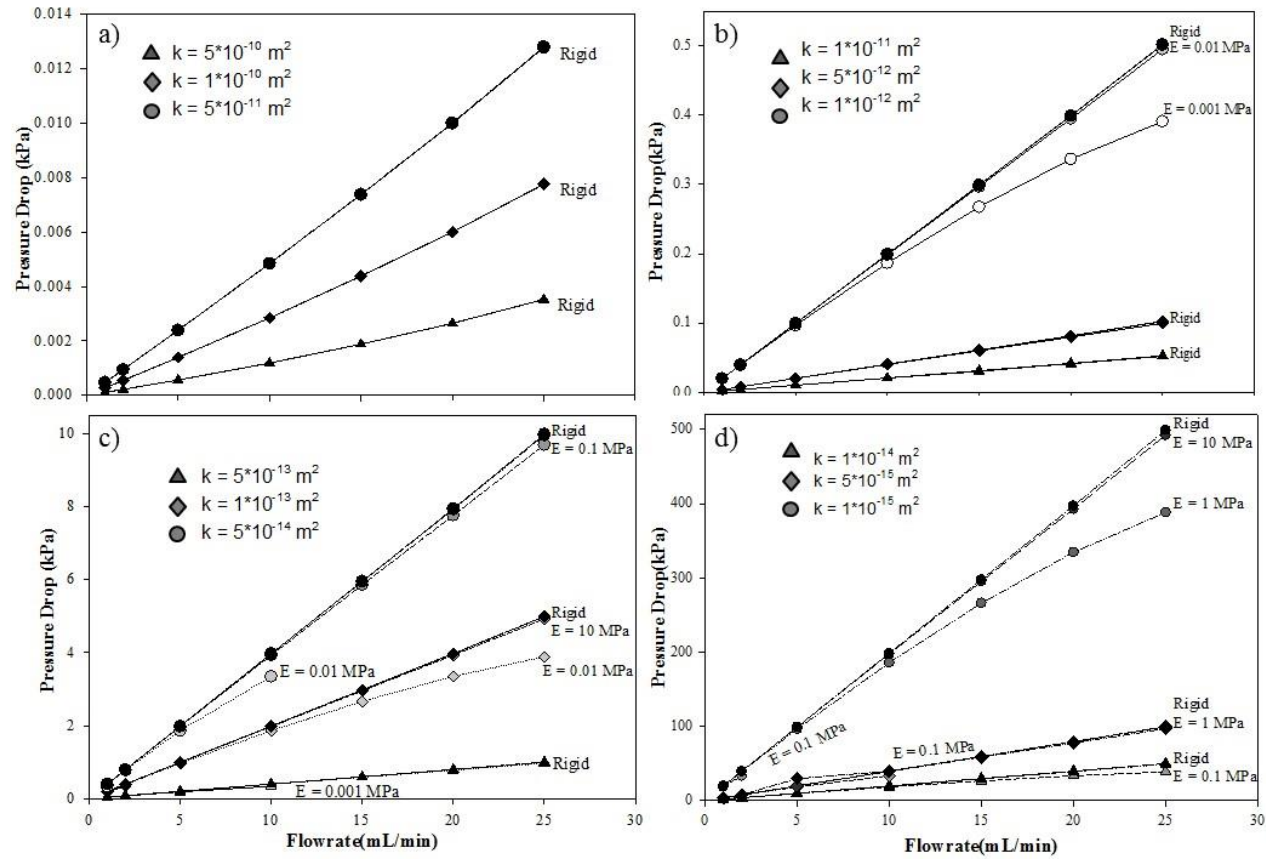
#### 4.4.6 Effect of permeability on pressure drop

Porous scaffolds used in tissue regeneration have permeabilities ranging from  $10^{-8}\text{m}^2$  to  $10^{-12}\text{m}^2$  (Dias, Fernandes et al. 2012) while that of many tissues is in the range of  $10^{-12}\text{m}^2$  to  $10^{-15}\text{m}^2$  (Swartz and Fleury 2007). Thus, during tissue regeneration the permeability of the porous scaffolds has to decrease via remodeling by assembly of matrix elements, increased cell number, and scaffold degradation. Reduced permeability significantly affects the flow dynamics and

nutrient distribution, which is directly related to the quality of the regenerated tissue. Simulations were performed by decreasing the permeability from  $10^{-10}\text{m}^2$  to  $10^{-15}\text{m}^2$  to understand how pressure drop would change if scaffold deformation is included with the same mechanical properties. Reduction in permeability had a significant effect on pressure drop and deformation, since the fluid stress on the scaffold increases with decreases in permeability (**Figure 4.7**). When the scaffold permeability was in the range of  $10^{-12}\text{m}^2$ , a significant difference in the pressure drop was observed between scaffolds with an elastic modulus of 0.001MPa to that of a rigid scaffold. However, scaffold deformation was negligible at 0.001MPa elastic modulus near  $10^{-10}\text{m}^2$  scaffold permeabilities. Deformation may be significant when the permeability approaches that of native soft tissues.

#### **4.4.7 Effect of scaffold mechanical properties on pressure drop and deformation**

Significant research has been done in creating biomaterials, with different chemical and mechanical properties, for various tissues engineering applications. The scaffolds have a broad range of elastic moduli from 10MPa to 1200MPa (Goulet RW 1994) for hard tissues and 0.04MPa to 350MPa (Hayashi 2003) for soft tissues. Hence, to understand the effect of elastic modulus on scaffold deformation and pressure drop, simulations were performed for a broad range of elastic modulus (0.001MPa to 100MPa). In addition, effect of Poisson's ratio in the linear range (0.1 to 0.49) and density was also tested. Reduction in elastic modulus decreased the pressure drop, as a result of scaffold deformation, especially at higher flow rates (**Figure 4.7**).



**Figure 4.7** Simulation results of pressure drop across the axial-flow bioreactor showing for various permeabilities and elastic moduli at various flow rates.

As higher flow rates create higher mechanical stress, scaffolds with lower elastic modulus are more susceptible to deformation. The effect of Poisson's ratio on pressure drop across the axial-flow bioreactor was evaluated at 20mL/min flow rate using physical and mechanical properties values of PCL-CA scaffold. The simulation showed no change in pressure drop (149.13Pa) for Poisson's ratio values 0.1, 0.2, and 0.3 and an insignificant increase for 0.4 Poisson's ratio (149.14Pa) and 0.49 (149.16Pa). Similarly, simulations showed no dependency of density on pressure drop.

#### **4.5 Discussion**

In this study, pressure drop and deformation across an axial-flow bioreactor were modeled by coupling equations describing fluid flow with structural mechanics of the scaffold. The elastic modulus and Poisson's ratio of electrospun PCL-CA was evaluated under hydrated condition. The elastic modulus of PCL-CA scaffold was less than the PCL scaffolds prepared by salt leaching technique, where the elastic modulus was 600 ( $\pm 100$ ) kPa under similar testing conditions (Podichetty and Madihally 2014). These differences could be attributed to the scaffold preparation techniques (Sethuraman, Makornkaewkeyoon et al. 2013). In addition, presence of CA in the inner core may not add significant mechanical strength in hydrated conditions. Using a similar technique, the elastic modulus of CG scaffolds have been reported, which was nearly ten times less than PCL-CA electrospun scaffolds (Ratakonda, Sridhar et al. 2012).

Scaffolds with different pore architecture were used in this study, fibrous PCL-CA scaffold and CG scaffold with cylindrical pores. Scaffold permeability is typically calculated based on porosity and tortuosity relationship to porosity (Koponen, Kataja et al. 1997; Shimko, Shimko et al. 2005). Alternatively, permeability can be estimated using pore size distribution with imaging (Dias, Fernandes et al. 2012) or using Kozeny-Carman equation based on pore characteristics (Dias, Fernandes et al. 2012). Scaffolds utilized in tissue engineering applications are routinely

characterized for porosity, pore size and shape, fiber diameter and fiber alignment. In addition, numerous publications have correlated the effect of pore size on cell colonization in 3D structures (Lawrence and Madihally 2008). Determination of permeability based on pore architecture such as pore size, pore shape, and number of pores per unit area helps utilizing the scaffold microstructure data rather than requiring additional porosity measurement and/or using an arbitrary equation. The pore characteristics and structural properties of the scaffold were used to calculate the permeability. Equations to calculate the permeability that utilize these features are valuable to determine pressure drops *a priori* and monitor tissue remodeling. The assumption of rectangular pores would be more valid if salt leaching technique was employed. This study attempted to connect those dots via modeling and validating the results using experiments.

The scaffold properties were used for predicting pressure drop and deformation. Flow-through the porous medium was simulated using Brinkman equation, which consists of an additional viscous term compared to Darcy's equation in the form of a Laplacian, similar to Navier-Stokes equation. This term accounts for the momentum transport by microscopic shear effects as well as pressure gradients (Whitaker 1996) and allows smooth transition from free flow to porous media. The Brinkman equation has been extensively used in the analyses of other reactors and proved to be valuable to compare results with previous publications on flow-through bioreactor (Devarapalli, Lawrence et al. 2009; Lawrence, Devarapalli et al. 2009; Podichetty, Dhane et al. 2012; Pok, Dhane et al. 2013). However, the maximum and average Reynolds number in the porous scaffold were less than one, suggesting the applicability of Darcy's equation at low flow rates. Based on Darcy's law, the scaffold permeability can be calculated from experimental pressure drop and flow rate. This permeability can be compared with the permeability calculated based on scaffold pore characteristics. The theory of poroelasticity for analysis of a porous media consisting of an elastic matrix containing interconnected fluid-saturated pores could be used in axial-flow bioreactors (Cowin 1999) similar to soil consolidation and bone biomechanics studies



(Sengers, Oomens et al. 2004; Hellmich and Ulm 2005). A mesoscopic approach using Lattice-Boltzmann method is also used based on Brinkman equation (Khayyeri, Checa et al. 2010). Since Lattice-Boltzmann method is limited to a small portion of the scaffold, the obtained simulation results are difficult to validate experimentally at this juncture. However, these values need to be validated experimentally as applicability of Brinkman equation for conditions below porosity of 0.5 is questionable. Pressure drop simulation results were in agreement with the experimental results. This is unlike the flow-through bioreactor where the pressure drop varied with elastic material due to deformation (**Table 4.3**). The relatively lower mechanical strength of CG scaffold can cause deformation at higher flow rates (Podichetty and Madihally 2014). This suggested the validity of the modeling approach and the permeability equation based on pore architecture. Also, scaffold deformation was significantly lower relative to that in flow-through bioreactor.

Stresses transferred due to fluid flow induced deformation can be determined by combining solid mechanics with fluid mechanics. Decreased shear stresses in the bioreactor would increase matrix composition in parallel-flow bioreactors relative to flow-through reactor (Zhao and Ma 2005). This has been speculated to be due to high shear stresses washing away secreted matrix elements prior to their assembly in flow-through bioreactors (Devarapalli, Lawrence et al. 2009). Thus, decreased shear stress could have a similar impact when axial-flow bioreactors are utilized. Changing the flow configuration to axial direction is advantageous as fluid is distributed throughout the bottom of the scaffold. Hence, the performance of the axial-flow bioreactor is superior to the flow-through configuration especially with lower elastic modulus scaffolds. Compared to flow-through bioreactor, axial-flow bioreactors can be operated at high flow rates as the pressure drops are significantly lower. The axial-flow is suitable for culturing highly metabolic active cells that require a high replenishment of nutrients (Chu, Shi et al. 2009).

An understanding of how pressure drop relates to permeability can be useful in monitoring tissue growth and adjust the flow rate to ensure nutrient sufficiency. When pressure drop is used as a non-invasive approach to monitor tissue growth, considering the scaffold deformation is useful to understand the quality of the regenerated tissue. Nevertheless, measurement of pressure drop in real time at a certain flow rate can be used as a non-invasive way to monitor tissue growth even in soft tissues. These results suggest minimum to no effect of Poisson's ratio and fluid density on porous scaffold deformation in axial-flow bioreactors. In summary, using an axial-flow bioreactor for scaffolds with lower mechanical strength can avoid deformation.

#### **4.6 Acknowledgements**

I would like to thank Mr. Abdu Khalf for assistance with PCL-CA scaffold and SEM imaging. I would also like to thank Mr. Prasana Bhasker for assistance with the bioreactor design and Dr. Brenda Smith for assistance with the  $\mu$ CT.

## CHAPTER 5

### RESIDENCE TIME DISTRIBUTION ANALYSIS AND EVALUATION OF EXIT CONCENTRATION IN AXIAL-FLOW BIOREACTOR

#### **5.1 Introduction**

The axial-flow bioreactors have recently attracted attention in tissue engineering applications for regenerating a variety of high aspect ratio tissues, such as skin, liver, and bladder. They offer several advantages over conventional perfusion bioreactors such as flow-through and parallel-flow. The nutrient distribution in axial-flow bioreactors is mainly convection-driven, and the ability to operate at high flow rate with relatively low pressure drop and scaffold deformation. The objectives of this study were to analyze residence time distribution (RTD) in the axial-flow bioreactor, and validate the outlet oxygen and glucose concentration predictions from computational fluid dynamics (CFD), dispersion model, and segregation model using an experimental setup.

CFD is useful in evaluating flow patterns inside bioreactors (Porter, Zauel et al. 2005; Cioffi, Boschetti et al. 2006; Hutmacher and Singh 2008; Wendt, Riboldi et al. 2011). The nutrient consumption kinetic can be added to the model to predict nutrient consumption based on bioreactor configuration, scaffold properties, cell kinetics, and operational conditions. However, these predictions must be validated with experimental analysis.

Further, CFD analysis can be used to understand the influence of nutrient transport on cell growth, effect of dynamics of cell proliferation in a bioreactor, characterize fluid flow, provide initial estimates, and supplement experimental results. One major challenge with CFD is the verification of model and reliability of computations involved. Gold standard for verification is to perform experiments on physical realization of simulation predictions and tally experimental observations against CFD results. This comparison would help quantify deviations in CFD computations from actually observed results. Hence, in this study nutrient consumption was assessed experimentally by seeding cells in the scaffold to validate consumption prediction from simulations.

## **5.2 Materials and methods**

### **5.2.1 Preparation of porous scaffolds**

Ten cm diameter circular CG and PCL scaffolds with a thickness of 0.2cm were prepared by the methods previously reported (Podichetty and Madihally 2014). In brief, 2%(wt/v)-2%(wt/v) chitosan (190-310kDa MW and 85% degree of deacetylation)-gelatin Type-A (Bloom 300) from porcine skin (both from Sigma Aldrich Chemical Co. St. Louis, MO) was mixed in distilled water and autoclaved (at 121°C in a wet cycle for 60min). Under a sterile laminar hood, 0.5M acetic acid was added to dissolve chitosan. Solution was poured into a circular mold of 10cm diameter on a Teflon sheet (US Plastics Co.), frozen overnight at -80°C and freeze dried overnight in a Virtis freeze dryer (Gardiner, NY). Prior to hydration, all scaffolds were immersed in absolute ethanol until they were completely saturated without air pockets, and then washed in phosphate buffered saline solution (PBS, pH=7.4) prior to further use.

PCL solution was prepared by dissolving 2.7g of PCL in 16mL of chloroform. 29g of common salt (milled and sieved to obtain 74µm-246µm crystal size) was added to the PCL solution to obtain 85% porosity scaffold. The mixture was poured into a circular mold, and air dried for 8

hours in a ventilated hood to evaporate chloroform. The scaffold was removed and placed in distilled water for 36 hours to dissolve the salt. Distilled water was replaced every 3 hours. To characterize pore size and porosity, dry scaffolds were examined using a scanning electron microscope (SEM, Joel JSM 6360) at an accelerating voltage of 10kV after gold sputter coating at 40mA, similar to previous publication (Podichetty and Madihally 2013). In brief, micrographs were characterized for pore area, size, and number. Since the circularity factor was >0.8 for CG scaffolds, pore geometry was considered cylindrical and permeability ( $m^2$ ) of the porous medium ( $\kappa$ ) was calculated using the equation

$$\kappa = \frac{\pi}{128} n_A d^4 \quad (5.1)$$

where  $d$  is the pore diameter and  $n_A$  is the number of pores per unit area. The permeability of PCL scaffold was calculated assuming rectangular pores using the equation

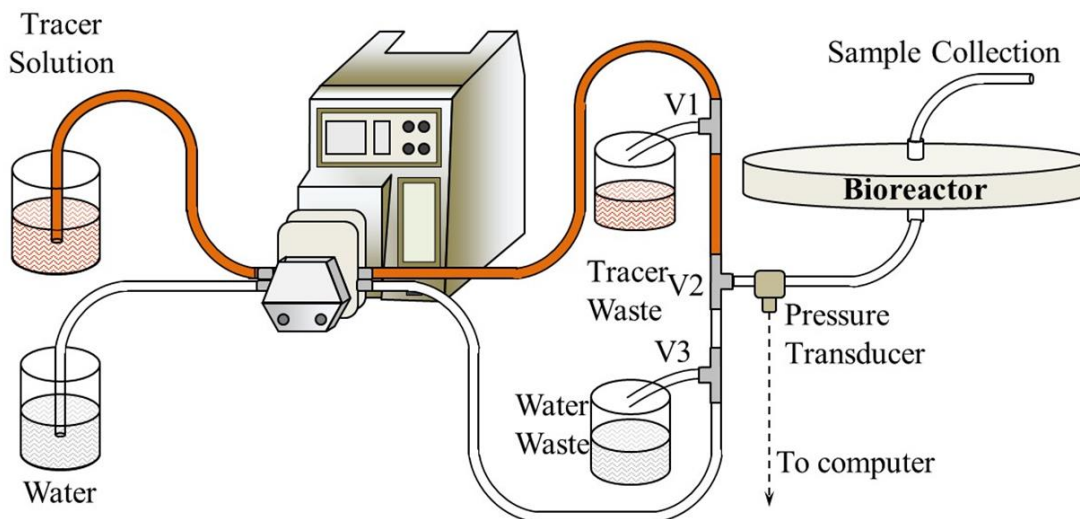
$$k = \frac{n_A L W^3}{12} \quad (5.2)$$

where  $n_A$  is the number of pores per unit area,  $L$  is the pore length, and  $W$  is the pore width.

### 5.2.2 Obtaining RTD function using step-input of a tracer

An open flow system (**Figure 5.1**) previously reported (Lawrence, Devarapalli et al. 2009) was used to introduce a tracer with step input mode, with minor modifications. In brief, the axial-flow bioreactor was constructed in house with a split design, top part with the conical structure and outlet while the bottom part with location for placement of the scaffold, stainless steel distributor plate, and the inlet. A silicon gasket was used to tightly seal the two parts. The tubing system was designed in order to include two fluid reservoirs and two waste containers. Two tubes were passed via the peristaltic pump, one for the water reservoir and the other for the reservoir filled with red tracer solution. The tubes were connected to three way stopcocks (V1 and V3) to divert

the fluid either to the bioreactor or into a waste container. A three way stopcock(V2) was used to connect the two sides, which allowed the dye solution or water to enter the bioreactor.



**Figure 5.1** Schematic of the flow system used to determine the residence time distribution the axial-flow bioreactor (Lawrence, Devarapalli et al. 2009).

The value V1 was adjusted to allow the tracer to flow into the waste container and valve V3 was adjusted to allow water to flow through the bioreactor. Water was allowed to flow through the system until steady state was obtained. After achieving steady state, the tracer solution was introduced as step into the bioreactor by adjusting value V1 and V3 simultaneously. Experiments were performed at 15 mL/min flow rate on the bioreactor without scaffold and with CG and PCL scaffolds. During the experiments, 0.5mL to 1mL sample were collected at different times until 4 times the space time (Podichetty, Dhane et al. 2012).

The samples were analyzed using Spectramax Emax spectrometer (Molecular Devices, Sunnyvale, CA) at a wavelength of 490nm. Absorbance,  $A(t)$  was measured for samples from each time point ( $t$ ). A 96 well plate with 100 $\mu$ L of sample from each time point was used for analysis.

The original tracer solution Absorbance ( $A_0$ ) was measured and  $A(t)/A_0$  was calculated. The fractional concentration ( $C(t)/C_0$ ) exiting the reactor was calculated using the following equation

$$\frac{C(t)}{C_0} = \frac{A(t)}{A_0} \quad (5.3)$$

Obtained  $C(t)/C_0$  values for various time intervals were plotted in Sigma Plot 12 (SPSS Science, Chicago, IL) software. A non-linear Chapman 3-parameter equation was found to fit the data

$$\frac{C(t)}{C_0} = a(1 - e^{-bt})^c \quad (5.4)$$

where  $a$ ,  $b$  and  $c$  are the constants, obtained from the curve fit. The external age distribution function,  $E(t)$ , was calculated using the equation (Fogler 2006).

$$E(t) = \frac{d}{dt} \left[ \frac{C_{mix}(t)}{C_0} \right]_{Step} = abce^{-bt}(1 - e^{-bt})^{1-c} \quad (5.5)$$

Mean residence time was calculated using the first-moment equation

$$t_m = \frac{\int_0^{\infty} tE(t)dt}{\int_0^{\infty} E(t)dt} = \frac{\int_0^{\infty} e^{-bt}(1 - e^{-bt})^{1-c} t dt}{\int_0^{\infty} e^{-bt}(1 - e^{-bt})^{1-c} dt} \quad (5.6)$$

Further the variance was calculated using the second-moment equation

$$\sigma^2 = \frac{\int_0^{\infty} (t - t_m)^2 E(t)dt}{\int_0^{\infty} E(t)dt} \quad (5.7)$$

All integrals were evaluated numerically. The experiments were repeated three times for each condition. The mean residence time,  $t_m$  was obtained from the residence time analysis. The obtained  $t_m$  values were compared with the ideal space time,  $\tau$ , for corresponding volumetric flow

rates and volume of the reactor. The  $\frac{\sigma^2}{t_m^2}$  values were also calculated for each experiment. The average and standard deviation values were calculate for each condition

### 5.2.3 Determining nutrient exit concentration using segregation and dispersion models

The mixing in the bioreactor was considered to follow a macrofluid model (or segregation model) based on the assumption that cells present on scaffold are surrounded by a nutrients film and behave like micro batch reactors. Based on this model, average conversion,  $\bar{X}_A$ , was obtained using the equation

$$\bar{X}_A = \int_0^{\infty} (X_A(t))_{batch} E(t) dt \quad (5.8)$$

where  $(X_A)_{batch}$  is the conversion obtained in a batch reactor for time t. Since the reaction is in liquid phase, a constant volume was assumed. The batch conversion at any time, t, was obtained using the rate of reaction equation

$$r_A = \frac{-C_{A0} d(X_A)_{batch}}{dt} = -\frac{V_m [1 - (X_A)_{batch}]}{[K_m + C_{A0} [1 - (X_A)_{batch}]]} \quad (5.9)$$

Equation (12) was rearranged and integrated to obtain  $X_A(t)_{batch}$  function as

$$C_{A0} * (X_A)_{batch} - K_m * \ln(1 - (X_A)_{batch}) - t * V_m = 0 \quad (5.10)$$

Obtained  $X_{batch}$  for each time point was multiplied with the E(t) function from Equation (5.5) and integrated numerically to obtain the average conversion. Since, E(t) was determined at 15 mL/min flow rate, it was reduced to dimensionless quantities using the ideal space time,  $\tau$ .

$$\theta = \frac{t}{\tau}; E(\theta) = \tau E(t) = \tau abce^{-bt} (1 - e^{-bt})^{1-c} \quad (5.11)$$



The dimensionless age distribution function was utilized to calculate the conversion and exiting concentrations of oxygen and glucose for 5 mL/min, 2 mL/min, and 1 mL/min.

For dispersion model, assuming much of the changes happen within the scaffold region i.e., a closed vessel with large deviations ( $1/Pe > 0.01$ ) from plug flow reactor dispersion number was calculated using the equation

$$\frac{\sigma^2}{t_m^2} = \frac{2}{Pe_D} \left[ 1 - \frac{1}{Pe_D} (1 - e^{-Pe_D}) \right] \quad (5.12)$$

Using experimentally determined  $\frac{\sigma^2}{t_m^2}$  values,  $Pe_D$  was calculated. This model involves dispersion of the material in the axial direction. Based on Michaelis-Menten consumption kinetic equation for oxygen and glucose, outlet concentration of oxygen and glucose were calculated based on the shell balance

$$\frac{1}{Pe_D} \frac{d^2 C_A}{dz^2} - \frac{dC_A}{dz} - \frac{\tau v_{\max} C_A}{K_M + C_A} = 0 \quad (5.13)$$

with the Danckwerts (originally derived by Langmuir) boundary conditions

$$\text{when } z=0, C_A + \frac{1}{Pe_D} \frac{dC_A}{dz} = C_{A0}$$

$$\text{when } z=0.2 \text{ cm, } \frac{dC_A}{dz} = 0$$

Equation (5.13) was solved numerically for various flow rates using partial differential equations tool in COMSOL in one dimensional stationary coefficient form. The exit concentration was calculated for 1mL/min, 2 mL/min, 5mL/min, and 15mL/min at 3 different cells densities. Table 5.1 shows the rate constants used in the calculations. The exit concentrations from the dispersion model were compared to results from other methods.

#### 5.2.4 Determining nutrient concentration by HepG2 cell seeded scaffolds:

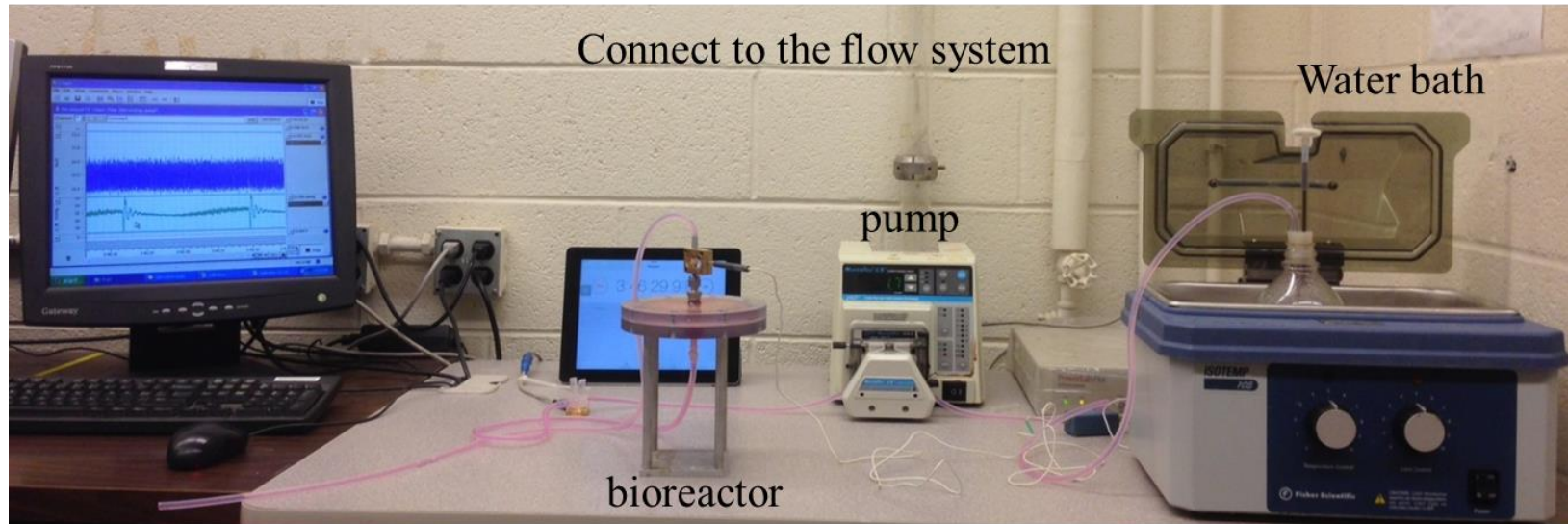
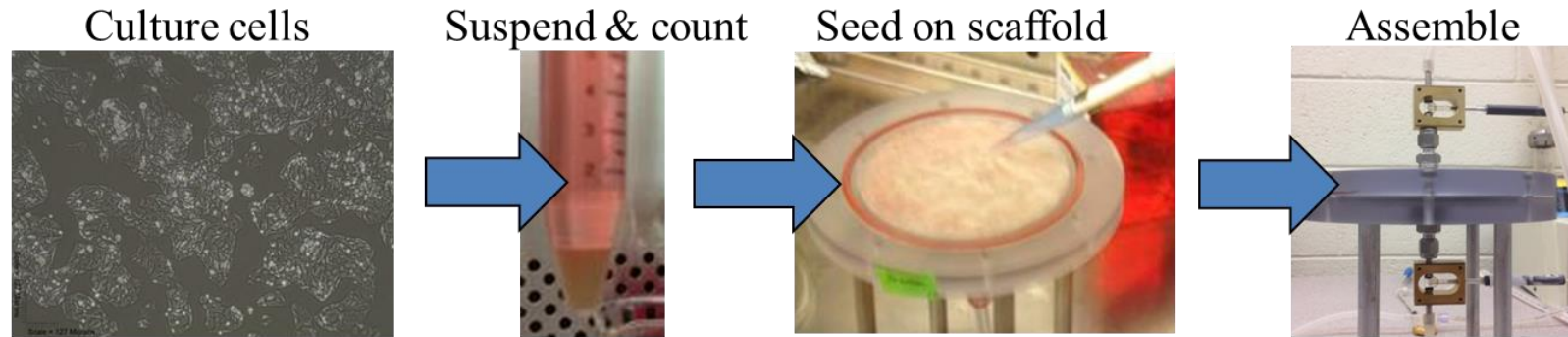
Human hepatocellular carcinoma cell line Hep G2 (ATCC<sup>®</sup> HB-8065<sup>™</sup>) were maintained in Eagles's Minimum Essential Medium (EMEM, ATCC Manassas, VA) following vendor's protocol. In brief, EMEM supplemented with 10% fetal bovine serum (Invitrogen Corp, Carlsbad, CA) was used as the culture medium initially. Cells were maintained at 37°C, 5% CO<sub>2</sub>/95% air, and fed with fresh medium every other day. When confluent or during the seeding process, cells were detached with 0.25% (w/v) trypsin-0.53mM EDTA (Invitrogen Corp, Carlsbad, CA), neutralized with EMEM. Cells were centrifuged at 125×g for 5minutes and dispersed in growth medium. Viable cells were counted using trypan blue dye exclusion assay. The CG scaffold of 10cm diameter and 0.2cm thickness formed by freeze drying was neutralized in ethanol, washed with sterile PBS, and exposed to UV light for 20 minutes. Based on the scaffold volume,  $19 \times 10^6$  cells ( $1.2 \times 10^{12}$  cells/m<sup>3</sup>) were seeded.

To obtain uniform cell distribution across the scaffold, the concentrated cell suspension was carefully distributed to cover the entire scaffold, similar to the process described previously (Iyer, Walker et al. 2012). Seeded scaffold was incubated overnight with 8mL growth medium to ensure cell attachment (**Figure 5.2**). The open-loop perfusion system consisting of a medium reservoir (immersed in a water bath to maintain 37°C), a variable speed peristaltic pump (Masterflex, Cole Palmer, IL), and the axial-flow bioreactor used in the RTD studies. The cell seeded scaffold was placed in the bioreactor and the two parts were assembled. Based on the simulation studies explained below, growth medium was perfused at 1mL/min flow rate and then changed to other flow rates. The oxygen concentrations were obtained in real-time using two flow-through electrodes (16-730, Microelectrodes, Inc., Bedford, NH) located at the entrance and the exit of the bioreactor. Oxygen concentrations from the electrodes were acquired using Chart<sup>™</sup> 5 for Windows via the Powerlab/4SP System (ADI Instruments, Inc., Colorado Springs,

CO) after allowing the bioreactor to reach steady state for every flow rate. Exiting medium was collected for determining the glucose content. Experiments were performed in triplets.

The glucose content was analyzed using glucose-oxidase membrane in YSI-2700 Biochemistry analyzer (YSI Life Sciences, Yellow Spring, OH) following vendor's protocol, similar to previous publication(Podichetty, Dhane et al. 2012).

After the incubation time, cell seeded scaffolds from 5 different locations in the scaffold were analyzed by scanning electron microscope (SEM, Joel JSM 6360, Tokyo, Japan) and histology with hematoxylin and eosin stain (H&E). For this purpose, cell-containing scaffolds were fixed in 10% buffered formalin solution for 30min at room temperature. Samples were dried using absolute ethanol followed by a brief vacuum drying. Dried samples were sputter coated with gold at 40mA prior to observing under SEM. Samples were embedded in paraffin, 4 $\mu$ m thick sections were cut, and were stained with (H&E). Digital photomicrographs were captured at random locations using a color digital camera attached to an inverted microscope.



**Figure 5.2** Schematic of cell culture experimental setup with axial-flow bioreactor

### 5.3 CFD Simulation of Nutrient Consumption.

To understand the nutrient distribution with consumption and predict exit concentrations, CFD simulations were performed using COMSOL v4.3 Multiphysics (COMSOL, Inc., Burlington, MA) by coupling fluid flow with changes in the porous scaffold on a dynamic mesh and defined rate laws. The simulation setup for coupling fluid flow and structural mechanics (Podichetty and Madihally 2014) and coupling of the reaction kinetic described in the previous publications (Podichetty, Dhane et al. 2012). In brief, pressure at the exit was set to atmospheric conditions to mimic fluid flow through the bioreactor in open loop. The viscosity and density of the growth medium were assumed to be that of water and the scaffold pore size distribution was considered isotropic. Contribution of solid volume of cells in the scaffold was considered to be negligible relative to the polymer volume. An axial-flow bioreactor that can accommodate a circular scaffold of 10cm diameter and up to 0.2cm thicknesses was drawn using Computer Aided Design (CAD). Consumption of oxygen and glucose were assumed to follow Michaelis-Menten equation given by

$$-r_A = \frac{V_m C_A}{K_m + C_A} \quad (5.14)$$

where  $r_A$  is the rate of reaction of the species under consideration,  $V_m$  is the maximum reaction rate, and  $K_m$  is the Michaelis constant. The kinetic parameters of oxygen and glucose for primary porcine hepatocytes were used from literature (Devarapalli, Lawrence et al. 2009) and are summarized in **Table 5.1**. The estimation was based on the stoichiometry of aerobic respiration where 6 moles of oxygen is consumed per mole of glucose. Simulations were performed at constant cell density with the assumption that the residence time of nutrients within the reactor is significantly smaller than the growth rate of cells.

**Table 5.1** Rate constant of oxygen and glucose for hepatocytes with varying cell density.

Cell density (Cell/m <sup>3</sup> )	Cells in scaffold	Oxygen		Glucose	
		K <sub>m</sub> (mol/m <sup>3</sup> )	V <sub>m</sub> (μmol/m <sup>3</sup> s)	K <sub>m</sub> (mol/m <sup>3</sup> )	V <sub>m</sub> (μmol/m <sup>3</sup> s)
0.6×10 <sup>12</sup>	9.5×10 <sup>6</sup>	0.0263	20.5	0.0263	3.42
1.2×10 <sup>12</sup>	19×10 <sup>6</sup>	0.0263	41.1	0.0263	6.85
2.4×10 <sup>12</sup>	38×10 <sup>6</sup>	0.0263	82.2	0.0263	13.68

#Inlet concentrations: oxygen = 0.22mol/m<sup>3</sup> and glucose = 5.5mol/m<sup>3</sup>

However, simulations were performed using various cell densities to obtain snap-shots of consumption kinetics via calculating the  $V_m$  and  $K_m$  values at respective cell densities. Based on the 10cm diameter and 0.2cm thick scaffold, 9.5×10<sup>6</sup> cells (0.5×=0.6×10<sup>12</sup> cells/m<sup>3</sup>), 19×10<sup>6</sup> cells (×=1.2×10<sup>12</sup> cells/m<sup>3</sup>) and 38×10<sup>6</sup> cells (2×=2.4×10<sup>12</sup> cells/m<sup>3</sup>) were used to determine the effect of cell doublings.

The exit concentrations and nutrient distribution were evaluated using the convection diffusion equation, which links to the flow field to the concentration variances.

$$\nabla \cdot (-D\nabla c) + u \cdot \nabla c = r_A \quad (5.15)$$

where  $c$  is the concentration of the nutrient species,  $r_A$  is the rate of nutrient consumption of the species under consideration,  $D$  is the effective diffusivity of the species, and  $u$  is the velocity. The diffusivity of oxygen and glucose in CG scaffold (4.7×10<sup>-9</sup> m<sup>2</sup>/s and 1.19×10<sup>-9</sup> m<sup>2</sup>/s respectively) were obtained from previous publication (Podichetty, Dhane et al. 2012). The simulations were performed with stationary segregated solver in a three steps process. First, a MULTifrontal Massively Parallel Sparse (MUMPS) direct solver was used to evaluate variables  $x$ ,  $y$ , and  $z$ . Second, a Generalized Minimal Residual (GMRES) iterative solver was used to evaluate fluid velocity and pressure. Third, a GMRES iterative solver was used to evaluate the mesh displacement. A maximum 200 iterations were performed in the second and the third steps.

Velocity ( $V$ ) profiles within the scaffold thickness were obtained using “Cross-Section Plot Parameters” in the software, and *Peclet* number was calculated using the equation,

$$Pe = \frac{Vr}{D_{eff}} \quad (5.16)$$

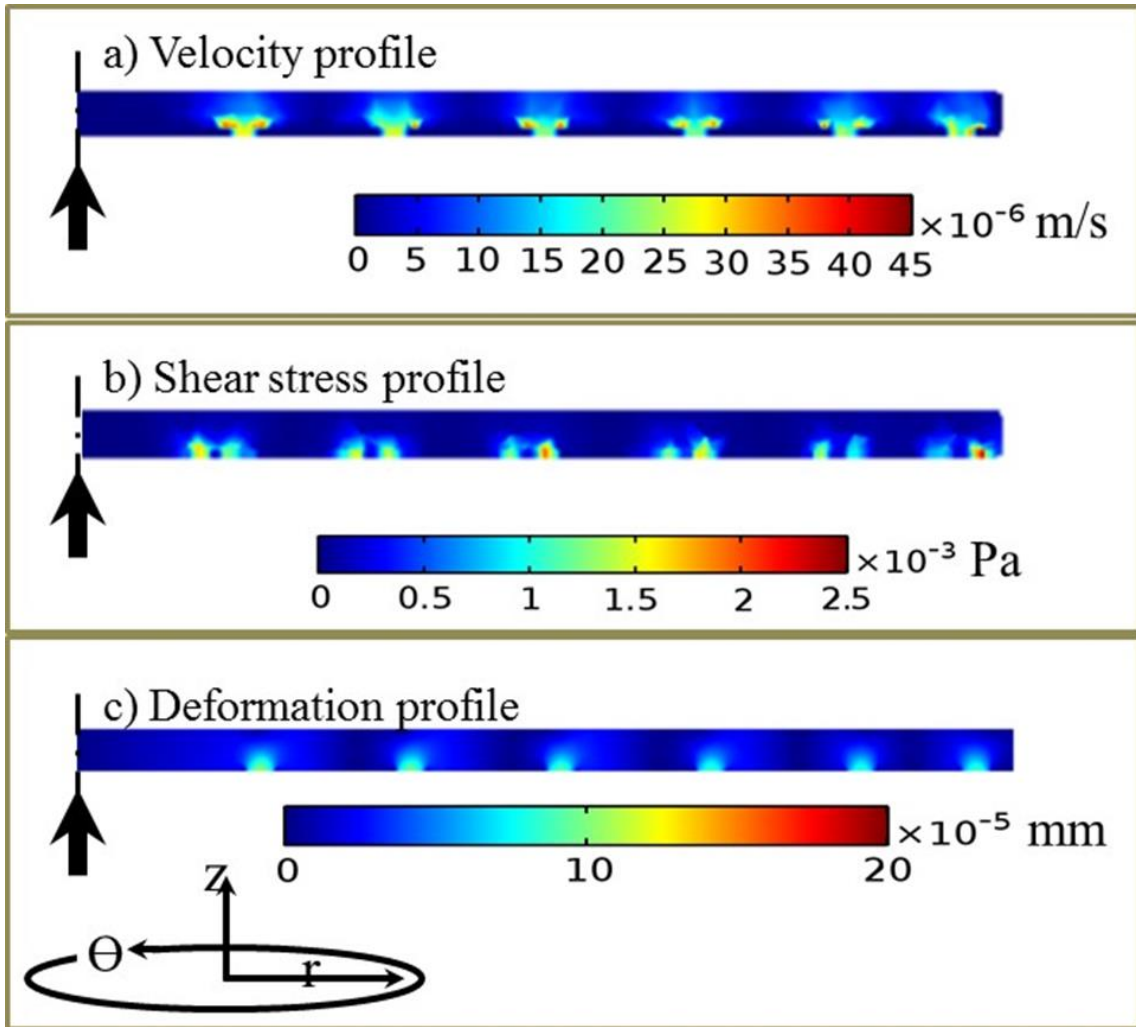
where,  $r$  is the pore radius, and  $D_{eff}$  is the diffusivity coefficient of either oxygen or glucose. Velocity profiles within the scaffold thickness were obtained using “Cross-Section Plot Parameters” in the software and used in the calculations.

## 5.4 Results and discussion

### 5.4.1 Simulated fluid flow characteristics

In this study, an axial-flow bioreactor accommodating a 10cm diameter of 0.2cm thick scaffolds was used. Using the same bioreactor configuration previously, the simulation setup has been validated to predict the fluid dynamic behavior (Podichetty, Bhaskar et al. 2014). The permeability was calculated based on pore architecture such as pore size, pore shape, and number of pores per unit area. Flow through the porous medium was simulated using Brinkman equation, although Darcy’s equation could be used as the Reynolds number is less than 0.1. Flow-induced deformation was modeled by coupling the steady state momentum transport equation with solid mechanics to account for deformation of the scaffold. Pressure drop experiments were performed to validate the model, and simulation results were in agreement with the experimental results. Since a distributor was utilized in the bioreactor design, stresses near the entry of fluid into the scaffold were analyzed.

The selection of flow rate depends on several factors including shear stresses inside the microarchitecture, scaffold deformation, and scaffold properties. Structural changes due to fluid flow alter the nutrient distribution due to altered local convective flow and diffusivity. **Figure 5.3** shows slice plots of velocity profile, shear stress profile, and deformation profile at 1mL/min.



**Figure 5.3** Cross sectional profiles of the scaffold from the central axis showing a) velocity, b) shear stress, and c) deformation at a flow rate of 1mL/min. Arrow indicate flow direction.

The velocity and shear stress profile were uniform with relatively higher values around the locations where growth medium entered the scaffolds. Maximum shear stresses of 0.1 dyne/cm<sup>2</sup> (or 0.01 Pa) were observed at regions where the medium entered the scaffolds. The velocity and shear stress values were significantly lower, sufficient to prevent cells from being dislodged by the flowing medium (Rademacher, Paulitschke et al. 2001). The maximum deformation was 14 $\mu$ m, even at locations where medium entered the scaffolds. This is over a 2000  $\mu$ m scaffold



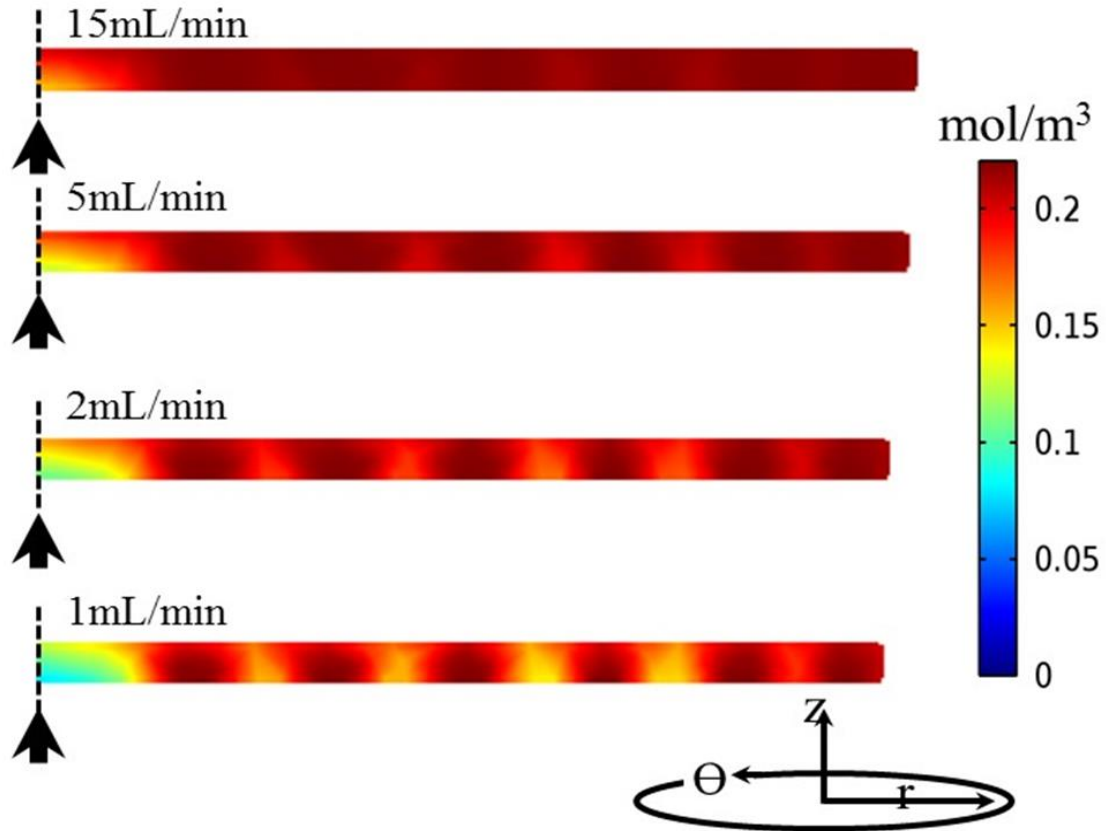
thickness (corresponding to 0.7% strain), suggesting no significant deformation even at higher elastic modulus value of the scaffold. These values were less by few orders of magnitude compared to flow-through bioreactors at same flow rates (Podichetty and Madihally 2014). Based on the velocity profile, shear stress profile, and deformation in the scaffold a flow rate of 1mL/min was selected for cell culture experiments.

#### 5.4.2 Concentration profile of nutrients

In addition to flow through porous medium and solid mechanics, convective diffusion equation was used to obtain the concentration profiles with nutrient consumption. Nutrient consumption was restricted to the porous region since the cells are present only in the scaffolds. Effect of flow rate on oxygen and glucose consumption by a constant number of cells ( $1.2 \times 10^{12}$  cells/m<sup>3</sup>) and distribution in the scaffold was investigated with defined rate laws. Also, a ‘quasi-static’ approximation was used with the assumption that the residence time of nutrients within the bioreactor is significantly shorter than the cell doubling time. Simulations performed showed nearly uniform distribution of nutrients across the scaffold at different flow rates (**Figure 5.4**). The average oxygen concentration in the scaffold was higher at higher flow rates as a result of reduction in residence time with increase in flow rate. The concentration profile showed lower oxygen concentrations at the center of the scaffold especially at lower flow rates. Earlier studies using a flow-through bioreactor showed that uptake rate of nutrients is sensitive to the local nutrient concentration (Devarapalli, Lawrence et al. 2009); muscle cells showed a 35% decrease in uptake for 50% reduction in oxygen concentration. The minimum volumetric flow rate can be estimated using the rate of consumption at the inlet condition. For example, oxygen uptake rate at the inlet concentration can be estimated using the Michaelis-Menten rate law. The volumetric flow rate can be calculated using the following relation,

$$-r_{O_2} = \frac{v\Delta C_{O_2}}{V_R} \quad (5.17)$$

where  $V_R$  is the volume of the reactor and  $\Delta C_{O_2}$  expected medium concentration change. This principle was also tested at 1 mL/min and found to be applicable.

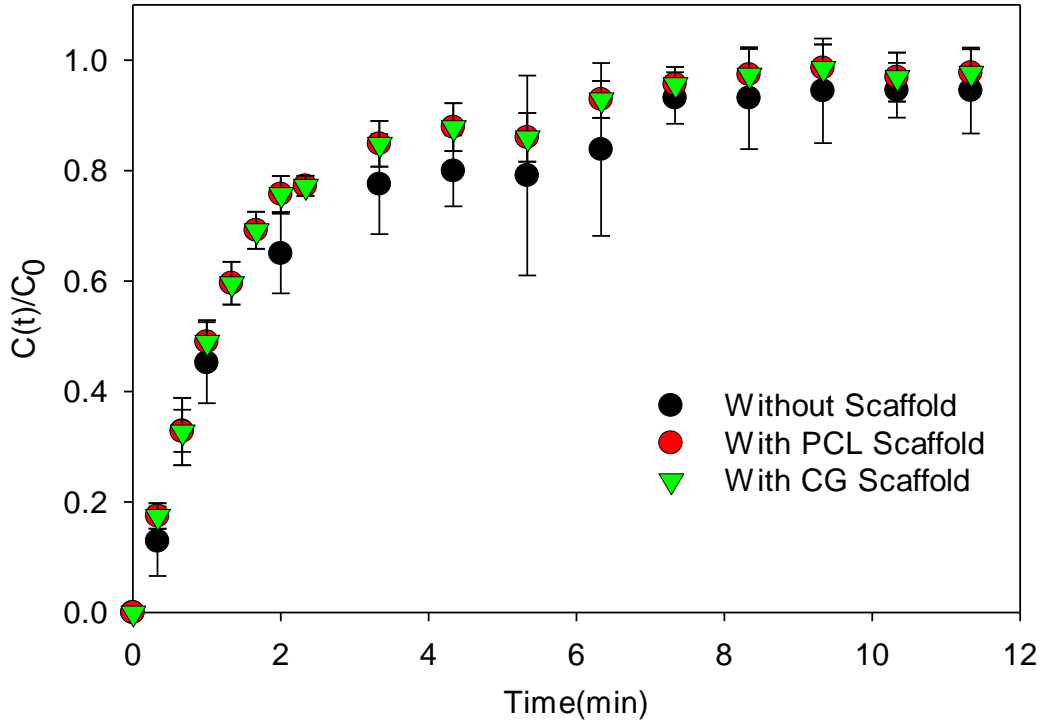


**Figure 5.4** Oxygen concentration profiles across the scaffold thickness from the central symmetric axis with  $1.2 \times 10^6$  cells/cm<sup>3</sup>. Arrows indicate flow direction.

### 5.4.3 Residence time distribution analysis

The primary requirement of bioreactors is to provide uniform distribution to the cells present in the porous scaffold. The RTD measures the amount of time different fluid molecules spends within the reactor (Lawrence, Beene et al. 2004; Fogler 2006). In other words, RTD is a measure of dispersal of a molecule in a flowing medium owing to the combined action of a velocity profile and molecular diffusion. RTD experiments were performed in the axial-flow bioreactor to understand the distribution of nutrients by introducing a tracer as a step change in the

concentration. The outlet tracer concentrations were plotted at various times to understand the profiles with and without scaffolds (**Figure 5.5**).



**Figure 5.5**  $C(t)/C_0$  curve at different time steps at 15mL/min. Each data point corresponds to the average of at least three experiments with different scaffolds preparations and error bars correspond to standard deviations.

The  $C(t)/C_0$  profiles were compared to understand whether channeling (initial peaks in the curve) or dead volume (long tail in the graph) is present. These indicated no peaks in the  $C(t)/C_0$  profiles suggesting that there was no channeling.

To understand the distribution of nutrients,  $E(t)$  and  $tE(t)$  curves were plotted from which  $t_m$  was calculated. The integral of  $E(t)$  curve gave a value less than 1, which suggested the possible of delayed exit of the nutrients due to the presence of dead zones. The tracer took longer to exit the bioreactor without a scaffold (**Table 5.2**), the  $t_m$  of  $2.75(\pm 0.19)$  min compared to  $2.52(\pm 0.19)$  min with CG scaffolds and  $2.1(\pm 0.08)$  min with PCL scaffolds at 15 mL/min flow rate.

**Table 5.2** Comparison of nutrient distribution by RTD at 15mL/min flow rate

Condition	Residence time (min)		Bioreactor Volume (mL)		Dead volume (mL)
	Ideal, $\tau$	RTD, $t_m$	Ideal $V_R$	RTD $V_R$	
without scaffold	2.90	2.75±0.19	43.5	41.24	2.26
with CG scaffold	2.74	2.52±0.19	41.1	37.8	3.33
with PCL scaffold	2.72	2.1±0.08	40.8	31.5	9.33

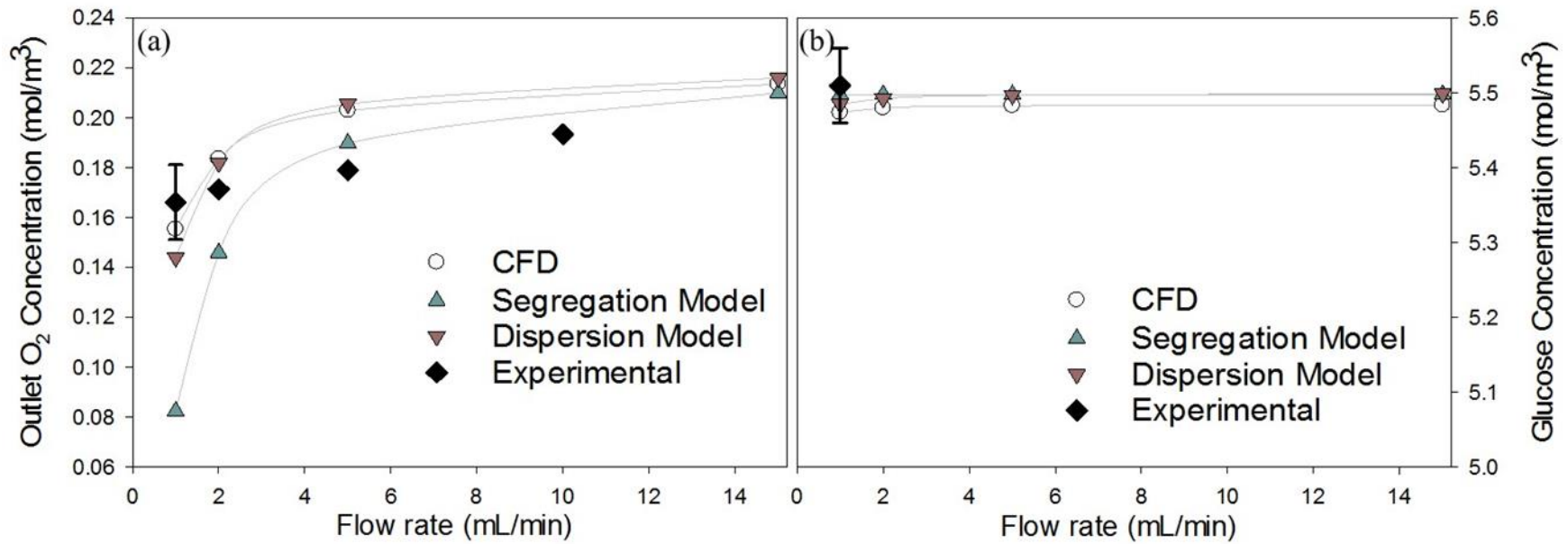
The calculations accounting for the volume occupied by the polymer in the scaffold suggested that some reduction in  $t_m$  with scaffold was as a result of reduced free volume of the bioreactor. The deviations in nutrient distribution from ideal conditions were compared by calculating the ideal space time,  $\tau$  (calculated using the ratio of the volume of the reactor to the flow rate of the growth medium) using ideal bioreactor volumes at 15mL/min (**Table 5.2**). Ideally when molecules are distributed in the entire volume of the bioreactor,  $t_m$  should be equal to  $\tau$ . However, there was a difference between the  $\tau$  and  $t_m$ , suggesting presence of minimal distribution zones i.e., dead volumes within the bioreactor. The difference between  $\tau$  and  $t_m$  was maximum in PCL scaffolds but there was minimal difference with CG scaffold.

The dead volumes were calculated by the difference in ideal volume to that observed via RTD by multiplying  $\tau$  and  $t_m$  with 15mL/min flow rate. For bioreactor without scaffold, dead volume was 2.26mL corresponding to 95% distribution. In the presence of CG scaffolds, dead volume increased to 3.33mL corresponding to 91.9% distribution, attributed to the increased resistance of the porous medium. The dead volume with PCL scaffolds was 9.33mL significantly higher, leading to only 77.1% distribution in the bioreactor. This further confirmed the significant difference between CG and PCL scaffolds due to the hydrophilic and hydrophobic nature of the polymers. For subsequent comparison studies CG scaffolds were used, as CFD simulations did

not account for the functional groups in the porous scaffold. Dead volume reduced the effective volume of the bioreactor, probably resulting in poor quality of regenerated tissue.

#### **5.4.4 CFD exit nutrient concentration compared to Segregation Model.**

The RTD for a bioreactor does not depend on the reaction, but on the fluid distribution characteristics. Hence, to understand nutrient consumption characteristics, combining the rate of reaction for hepatocytes is necessary to determine the outlet concentrations. Since rate of reaction is sensitive to the local nutrient concentration, there is a need to include mixing characteristics. Segregation model, a zero parameter model was used to calculate the outlet oxygen and glucose concentrations assuming that cells behave like microbatch reactors with the consumption of nutrients. Dimensionless  $E(\theta)$  was used to calculate average consumption at various flow rates (**Figure 5.6a**). Comparison of the outlet oxygen concentrations between the simulation results and segregation model predictions showed lower concentrations (i.e., higher consumption) of oxygen in segregation model at all flow rates. Deviations increased at reduced flow rates of 2mL/min and 1mL/min. Similar trends were also observed in glucose consumption (**Figure 5.6b**), although the consumption amount was relatively minor. Nevertheless, one reason for these deviations at lower flow rates could be the extrapolation of the RTD where nutrient distribution could be dominated by diffusion rather than convection which could alter the RTD profile.



**Figure 5.6** Nutrient outlet concentration comparisons. (a) CFD and segregation model oxygen outlet concentrations at a cell density of  $2.4 \times 10^{12} \text{ cells/m}^3$  (b) Comparison simulation with experimental oxygen and glucose consumption at 1 mL/min and cell density:  $1.2 \times 10^{12} \text{ cells/m}^3$ .

To better understand these possibilities, Peclet number was calculated using the Equation (5.16), which showed that lower flow rates had a *Peclet* number less than 1 (**Table 5.3**).

**Table 5.3** Peclet number at various flow rates in the porous scaffold

inlet flow rate (mL/min)	Average Interstitial velocity (m/s) $\times 10^6$	PCL Scaffold		CG Scaffold	
		$Pe_{oxygen}$	$Pe_{Glucose}$	$Pe_{oxygen}$	$Pe_{Glucose}$
1	1.874	0.297	0.074	0.664	0.165
5	9.37	1.48	0.37	3.32	0.82
10	18.5	2.97	0.74	6.64	1.65
15	28.1	4.47	1.11	10.00	2.48
20	37.4	5.94	1.47	13.28	3.29
25	46.8	7.40	1.84	16.55	4.10

Hence, one has to perform additional RTD experiments at those flow rates and predict the conversion from segregation model. Overall, segregation model provided good agreement at higher flow rates. These analyses can be extended to other cell types by combining the rate kinetic parameters (Devarapalli, Lawrence et al. 2009).

#### 5.4.5 Characterizing non-ideal fluid distribution using Dispersion Model

On the contrary, we questioned whether a one-parameter dispersion model that accounts for axial dispersion of molecules would provide better predictions. Others have used dispersion model for bioreactor predictions (Dubois, Tremblay et al. 2011). In this model, axial dispersion of nutrients governed by an analogy to diffusion, in addition to the convective distribution, is used to predict the deviations from ideal conditions. Correlations exist to relate  $Pe_D$  to the  $\sigma^2/t_m^2$  from RTD experiments to understand the nutrient distribution. For this purpose,  $\sigma^2/t_m^2$  values were calculated using the RTD results. The  $\sigma^2/t_m^2$  value for CG scaffolds was 0.56 ( $\pm 0.12$ ) and for PCL scaffolds it was 0.52 ( $\pm 0.063$ ).  $Pe_D$  was calculated from the correlation for a closed system using Equation (5.12). These values were near that of the  $Pe$  for glucose at 15 mL/min flow rate, suggesting that magnitude of dispersion coefficient to be near that of diffusivity of glucose.

Using the  $Pe_D$  values in Equation (5.13), exit concentrations were calculated (**Figure 5.6**). Exit concentrations from the dispersion model agreed with CFD predictions at all flow rates for both oxygen and glucose. A minor difference was at 1mL/min and 2mL/min flow rates; dispersion model predictions of oxygen and glucose exit concentrations were lower compared to CFD results. At 1mL/min flow rate substantial decrease was observed compared to 2mL/min flow rate, which suggests the need for convective distribution of nutrients. Another one-parameter model is the tanks-in-series model and at large deviations, predictions are known to be similar to that of a dispersion model. Alternatively, one could also use a compartmental model approach accounting for the dead volume while using PCL scaffolds.

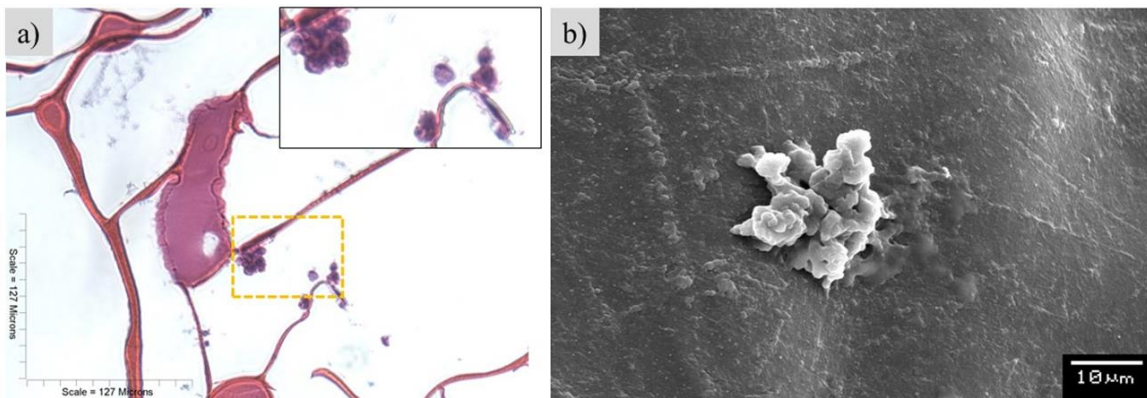
#### **5.4.6 Exit nutrient concentration compared to experiments.**

HepG2 cells were seeded at  $1.2 \times 10^{12}$  cells/m<sup>3</sup> density similar to the simulation setup and outlet concentrations was determined for oxygen and glucose at 1mL/min growth medium flow rate. The experimental outlet concentrations generally agreed with predicted concentrations from CFD simulations (**Figure 5.6b**). At higher flow rates, oxygen consumption results agreed with the segregation model and CFD. At lower flow rates, oxygen exit concentrations from the dispersion model agreed with the CFD. This suggests that the CFD simulations in general could model oxygen consumption kinetics. In terms of glucose, no trends could be observed, as the consumption was very little relative to the initial amount of glucose present in the medium. Also, the standard deviation in determining the concentration was higher than the actual consumption. Nevertheless, the minor variation between experimental results and model predictions can be attributed to a number of factors including distribution of cells, differences in the cell type, and surface from where kinetic parameters were determined that were used in CFD simulations.

To understand the cell distribution on porous structures, scaffolds with cells were analyzed by histology and SEM. Since scaffold was too large for these analyses, 1cm×1cm size samples from five different locations were analyzed. The H&E sections showed presence of cells in all



sections, suggesting uniform seeding of individual cells (**Figure 5.7a**). However, clusters of cells were observed in some areas rather than individual cells. Analyses of structures via SEM confirmed (**Figure 5.7b**) the presence of cluster of cells.



**Figure 5.7** Micrograph showing HepG2 cells in the CG scaffolds. a) H&E stained section. Inset is a magnified region from the rectangular area. b) Scanning electron micrograph.

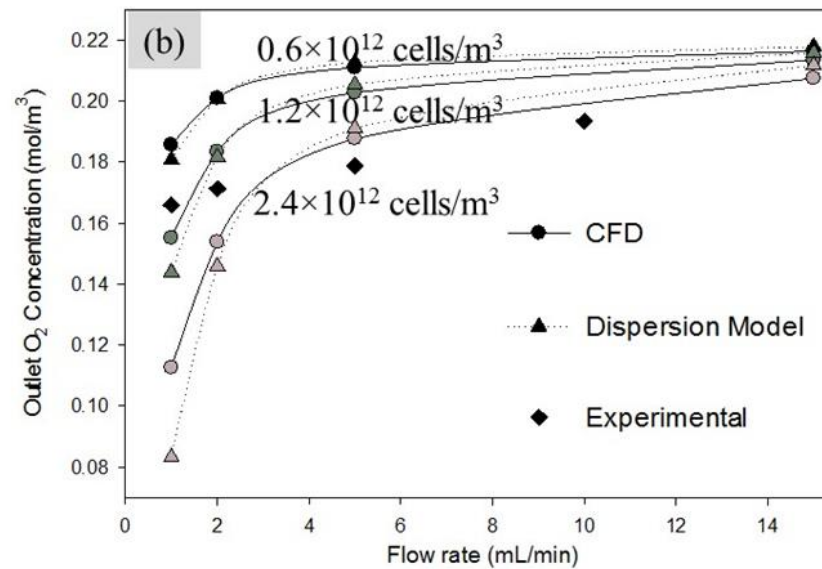
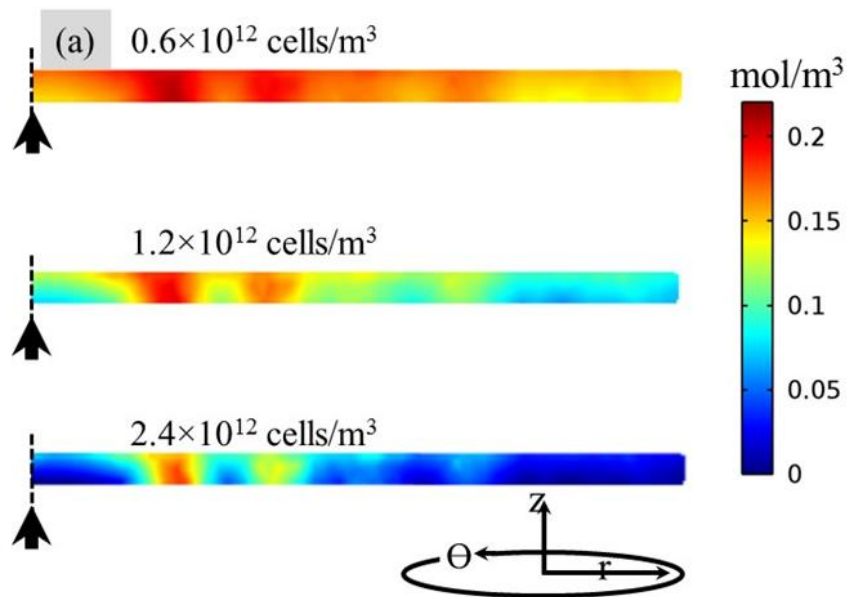
Formation of clusters could partially explain the reduction in consumption as there could be diffusion limitation in the exchange of nutrients to the cells present in the interior of the clusters. Presence of cell clusters could be attributed to the seeding technique where concentrated cells were seeded and one could either seed cells with more dilution or use the perfusion system to seed the cells to reduce cell clusters.

Alternatively, the minor differences in consumption could be attributed to the change in condition at which the kinetic parameters were evaluated and the sensitivity of the analyses (Weise, Fernekorn et al. 2013). Further, kinetic parameters obtained from porcine hepatocytes were used, while HepG2 cells are human derived (Ploss, Khetani et al. 2010; Janorkar, Harris et al. 2011). Although porcine hepatocytes have identical behavior compared to human hepatocytes, HepG2 cells are carcinoma-derived and programmed for growth with a compromised functionality. In addition, the kinetic parameters were obtained from cells which were cultured on tissue culture

plastic. Since CG porous structures were used in this study, there could be differences in the kinetic parameters. Hence, kinetic parameters must be evaluated for hepatocytes on 3D scaffolds. One advantage of using a large axial-flow bioreactor is that it allows determination of nutrient consumption with high fidelity. Experiments could be performed at different flow rates under steady state conditions to determine kinetic parameters.

#### **5.4.7 Effect of varying cell density on concentration profile.**

Simulations were performed at constant cell density to determine nutrient consumption characteristics. However, during the tissue regeneration process cells multiply which could affect the concentration profile in the bioreactor. To account for changes in cell number, simulations were performed using various cell densities to obtain snap-shots of consumption kinetics (**Figure 5.8a**). Since the current analysis of cell volume suggested no significant contribution to the porosity of the scaffold, simulations were performed at constant porosity. The concentration profile showed decrease in oxygen concentration with increase in cell density at the same flow rate (**Figure 5.8b**). Dispersion model predictions generally agreed with the CFD simulations, except at lower flow rates for all cell densities. Hence, increase in cell number increases nutrient requirements and one has to increase the flow rate accordingly during the regenerative process. The oxygen concentration was sufficient with the cell densities  $0.6 \times 10^{12}$  cells/m<sup>3</sup> and  $1.2 \times 10^{12}$  cells/m<sup>3</sup>. However, regions with insufficient oxygen concentration were observed with a higher cell density of  $2.4 \times 10^{12}$  cells/m<sup>3</sup> even though the outlet concentration was 0.113 mol/m<sup>3</sup>. Hence, the dynamic change in cell number influences the nutrient requirements in the scaffold. The addition of cell volume to the scaffold did not significantly alter the porosity and permeability of the scaffold. Since, pressure drop and shear stress were determined using Navier-Stokes equation and Brinkman equation, independent of the reaction, the change in cell density had no effect on pressure drop and shear stress. As tissue regeneration is a dynamic process flow rate must be carefully selected based on nutrient requirements of the cells and target cell density.



**Figure 5.8** Effect of cell density on oxygen consumption in CG scaffold. Arrow indicates flow direction.

The flow rate can be altered during the regeneration process based on predictions from CFD to meet the nutrient requirements. However, the flow rate has a significant influence on the shear stress experienced by the cells. Other factors such as change in permeability due to production of extracellular matrix (ECM) and higher cells density affect the pressure drop and hydrodynamics shear stress on the scaffold (Podichetty and Madihally 2014). Although, the axial-flow bioreactor can be operated at higher flow rate at reduced permeability without scaffold deformation, effects of flow rate and change in scaffold morphology on cells and nutrients requirements must be carefully monitored.

Since the nutrient distribution is governed by diffusion and convection (based on the bioreactor design), it is important to accommodate the effective diffusivities of nutrients through the porous structure. Based on the glucose diffusivity experiment described above, effective diffusivity ( $D_{eff}$ ) of  $4.7 \times 10^{-9} (\pm 0.05 \times 10^{-9}) \text{m}^2/\text{s}$  was used for glucose in simulation. The ratio of free diffusivity of glucose from literature (Lawrence, Devarapalli et al. 2009) to effective diffusivity was considered as the hindrance factor for 2%-2% chitosan-gelatin scaffolds.

## **5.5 Acknowledgements**

I would like to thank Mr. Kumar Singarapu for assistance with the cell culture experiments. I would also like to thank Mr. Óscar Pardo-Planas for assistance with the glucose analysis.

## CHAPTER 6

### CONCLUSION AND RECOMMENDATIONS

#### 6.1 Conclusions

In this study, an integrated approach of computational fluid dynamic modeling (CFD) and experimental analysis was used to evaluate governing equations useful in modeling 3D cell culture. The possibility of estimating the permeability from pore size with imaging or using Kozeny-Carman equation based on pore characteristics helps utilize the scaffold microstructure data rather than requiring additional porosity measurement and/or the use of an arbitrary equation. This study also includes analysis of nutrient consumption and deformation due to fluid flow. The governing equations are validated using experimental analysis. Additionally, an understanding of how pressure drop relates to permeability is useful in monitoring tissue growth and can be helpful to adjust the flow rate to ensure sufficient nutrient supply. When pressure drop is used as a non-invasive approach to monitor tissue growth, considering the scaffold deformation is useful to understand the quality of the regenerated tissue. Obtained conclusions for the three specific aims are given below.

##### 6.1.1 Modeling media induced porous scaffold deformation

- Effect of scaffold deformation due to growth medium perfusion was modeled and validated using a flow-through bioreactor. Since traditional poroelasticity uses Darcy's equation, applicable to conditions with very low fluid flow rate (Reynolds number  $< 1$ ), validity of ignoring the inertial effects in the bioreactors was tested. Based on the differences in predicted pressure drop, Brinkman equation was combined with structural mechanics along with a moving mesh to transcribe the forces generated by the flow of growth medium. Pressure drop in scaffolds typically used in soft tissue regeneration was

successfully predicted.

- CG and PCL scaffolds were formed using freeze drying technique and salt leaching techniques that generated pores of circular and rectangular shapes respectively. The pore shape-dependent equations were used to calculate the permeability and predict the pressure drops. Both scaffolds were prepared with similar porosities but with nearly ten-fold difference in permeability. Using an experimental set-up, Poisson's ratio was determined in hydrated conditions. CG scaffolds were found to follow non-linear elasticity while PCL scaffold were within the elastic limit. Comparison of experimentally determined pressure drop to that of simulations validated the equations and simulation approach.
- Simulations were performed for a range of permeabilities encompassing porous scaffolds and soft tissues, which showed significant increase in pressure drop with decrease in permeability. Also, significant deformation occurred at very low permeabilities despite the elastic modulus being 100MPa. Deformations caused the shear stress to be non-uniform despite the bioreactor design being selected based on the uniform shear stress distribution in rigid structures. Fluid flow compresses the scaffolds at the edges leading to channeling of media around the scaffold. This manifests in the reduction in pressure drop and knowing the pressure drop difference between a rigid scaffold to that of an deformable scaffold, one could estimate the effect of fluid flow on that particular scaffold.
- The simulations were extended to broad range of scaffolds mechanical properties using various elastic moduli and Poisson's ratio. Since low elastic modulus produced large deformations even at high permeabilities, optimizing fluid flow based on scaffold properties, flow configuration, and flow rate is important in growing tissues that are similar to the native tissues. Increase in Poisson's ratio, decreased the scaffold deformation and the pressure drop approached that of the rigid structures. It is essential

to couple the fluid flow and structural mechanics to effectively model the tissue regeneration process.

### **6.1.2 Modeling pressure drop using generalized scaffold characteristics in an axial-flow bioreactor for soft tissue regeneration.**

- Scaffolds with fibrous pore architecture and cylindrical pores were used to extend the analysis to broader types of scaffolds and in axial-flow bioreactor. The pore characteristics and structural properties of the scaffold were used to calculate the permeability. Flow through the porous medium was simulated using Brinkman equation and the moving mesh. The maximum and average Reynolds number in the porous scaffold were less than one in axial-flow bioreactor, suggesting that the Darcy's equation can be used at low flow rates. Based on Darcy's law, the scaffold permeability can be calculated from experimental pressure drop and flow rate. However, Brinkman equation was used for comparing it to other bioreactor types. Pressure drop in scaffolds typically used in soft tissue regeneration was successfully predicted.
- Experiments were performed to validate the pressure drop predictions. The scaffold properties were used for predicting pressure drop and deformation. Comparison of the pressure drop across the bioreactor from experiments at corresponding flow rates and scaffold properties showed agreement with the simulation results. This suggested the validity of the modeling approach and the permeability equation based on pore architecture. Stress transferred due to fluid flow induced deformation can be determined by combining structural mechanics with fluid flow.
- The scaffold deformation was significantly lower in axial-flow bioreactor relative to that of flow-through bioreactor at similar flow rates. Also, pressure drop across the scaffold decreased significantly in the axial-flow bioreactor compared to the flow-through bioreactor. Reduction in permeability had a significant effect on pressure drop and

deformation, since the fluid stress on the scaffold increases with decreases in permeability.

- The simulations were extended to broad range of scaffold's mechanical properties using various elastic moduli and Poisson's ratios. These results suggest minimum to no effect of Poisson's ratio and fluid density on porous scaffold deformation in axial-flow bioreactors. Using an axial-flow bioreactor for scaffolds with lower mechanical strength can avoid deformation. Changing the flow configuration to axial direction is advantageous as fluid is distributed throughout the bottom of the scaffold. The axial-flow is advantageous over flow-through as the fluid is distributed throughout the bottom of the scaffold. Hence, the performance of the axial-flow bioreactor is superior to the flow through configuration especially with lower elastic modules scaffolds. Compared to flow-through bioreactor, axial-flow bioreactors can be operated at high flow rates as the pressure drops are significantly lower. The axial-flow is suitable for culturing highly metabolic active cells that require a high replenishment of nutrients

### **6.1.3 Residence time distribution analysis and evaluation of exit concentration in axial-flow bioreactor**

- The convection-diffusion equation was utilized to obtain concentration profiles at three different cell densities in conjunction with the previous fluid dynamic simulations. A 'quasi-static' approximation was used with the assumption that the residence time of nutrients within the bioreactor is significantly shorter than the cell doubling time. Simulations performed showed uniform distribution of nutrients across the scaffold at different flow rates. The concentration profile showed lower oxygen concentrations at the center of the scaffold especially at lower flow rates. Based on the velocity and shear stress profiles as well as deformation in the scaffold a flow rate of 1mL/min was selected for cell culture experiments and model validation.



- The RTD analysis was performed to understand non-ideal fluid distribution and validate simulation results. The space time ( $\tau$ ) for the bioreactor without scaffold was higher than bioreactor with scaffolds due to higher free volume. Decreased mean residence time ( $t_m$ ) can be attributed to different phenomena such as dead zones and channeling which results in less consumption of nutrients. For bioreactor without scaffold, dead volume was 2.26mL corresponding to 95% distribution. In the presence of CG scaffolds, dead volume increased to 3.33mL corresponding to 91.9% distribution, attributed to the increased resistance of the porous medium. The dead volume with PCL scaffolds was 9.33mL significantly higher, leading to only 77.1% distribution in the bioreactor.
- The RTD analysis was combined with zero-parameter segregation model and one-parameter dispersion model to calculate the outlet concentration. Comparison of the outlet oxygen concentrations between the simulations and segregation model showed good agreement between 15mL/min and 5mL/min flow rates. However, deviations were observed at reduced flow rates of 2mL/min, which increased significantly at 1mL/min due to the use of dimensional analysis for extrapolating RTD to lower flow rates. Dispersion model is useful to predict scaffold dependent nutrient consumption with the help of RTD. However, obtaining a concentration distribution profile of nutrients that could help design new bioreactor may be limited.
- The model predictions were validated using an experimental setup with HepG2 (liver) cells. The experimental outlet concentrations generally agreed with predicted concentrations from CFD simulations. The minor variation between experimental results and simulation prediction can be attributed to a number of factors including distribution of cells, differences in the cell type, and surface from where kinetic parameters were determined that were used in CFD simulations. Histology and scanning electron microscopy analyses showed presence of cells in all sections, but clusters of cells were observed in some areas rather than individual cells. Formation of clusters could partially

explain the reduction in consumption as there could be diffusion limitation in the exchange of nutrients to the cells present in the interior of the clusters.

## 6.2 Recommendations

1. This study used large perfusion bioreactors along with average pore characteristics along with linear elastic materials, and showed the validity of using few governing equations. With this understanding one has to build improved models such as incorporating pore heterogeneity (Cioffi, Boschetti et al. 2006) and non-linear elastic characteristics (Ratakonda, Sridhar et al. 2012). A mesoscopic approach using Lattice-Boltzmann method is also used based on Brinkman equation to define fluid flow in porous media. Since Lattice-Boltzmann method is limited to a small portion of the scaffold, the obtained simulation results are difficult to validate experimentally at this juncture. However, these values need to be validated experimentally as applicability of Brinkman equation for conditions below porosity of 0.5 is questionable. One has to validate the approach with appropriate velocity profiles using techniques such as particle velocity meter and then validate the local shear stresses in soft tissues.
2. In this study, the kinetic parameters were obtained from porcine hepatocytes which were cultured on tissue culture plastic. Porcine hepatocytes have identical behavior compared to human hepatocytes, however, HepG2 cells used in this study are carcinoma-derived and programmed for growth rather than functionality mimicking native hepatocytes. Since porous scaffolds were used in this study, there could be differences in the kinetic parameters. Others have shown different effects of culturing HepG2 cells on porous structures relative to tissue culture plastic. Hence, kinetic parameters must be evaluated for hepatocytes on 3D scaffolds. Presence of

cell clusters in the scaffold could be attributed to the seeding technique where concentrated cells were seeded. One could either seed cells with more dilution or use the perfusion system to seed the cells to reduce cell clusters.

3. Dimensional analysis helps reduce complex problems to simpler form before obtaining a quantitative solution. In free flow inside closed channels, the selection of pipe diameter is done by utilizing the Moody chart based on dimensionless variables such as Reynolds number, relative roughness, and friction factor. Similarly, availability of *a priori* charts for designing systems involving porous media can help simplify the design process for bioreactor systems. The design variables such as flow rate, porosity and permeability can be transformed into dimensionless variables and characteristic curves can be developed to relate these dimensionless variables. This process will significantly reduce the amount of effort required to improve existing bioreactors and develop new ones.
4. In this study, the CFD and experimental analysis were performed using single pass open flow loop to validate the governing equations. Typically, tissue regeneration *in vitro* is performed in a closed loop by recirculating the media (Sodian, Lemke et al. 2002; Bock and Reichl 2007). To mimic the bioreactor operation during tissue regeneration where growth medium is recirculated and periodically replenished, performing CFD simulation is necessary. Further, in this study the experiments were performed at one cell density. Experiments must be performed at different cell densities to account for cell doubling during the tissue regeneration process.
5. The effective diffusivity of nutrient through porous scaffold is typically evaluated using theoretical equations based on scaffold porosity. The standard definition (Curcio, Macchiarini et al. 2010) in the literature for flow through porous medium is

$\frac{D_{eff}}{D_{\infty}} = \left( \frac{\varepsilon_p}{\tau} \right)$  where  $\tau$  is the tortuosity of the porous medium although others have

used that of the cells. In most models, the tortuosity is defined in terms of scaffold porosity (Coletti, Macchietto et al. 2006). The Mackie-Meares relationship and Maxwell relationship are some of the widely used models for predicting porosity based effective diffusivity. However, these models fail at lower porosities and when the size of the nutrient molecule is similar to that of the scaffold pore size. Hence, existing models or new models must be developed to account for the pore size relative to the molecule size.

## REFERENCES

- Azuaje, F. (2011). "Computational discrete models of tissue growth and regeneration." Brief Bioinform **12**(1): 64-77.
- Bancroft, G. N., V. I. Sikavitsas and A. G. Mikos (2003). "Design of a flow perfusion bioreactor system for bone tissue-engineering applications." Tissue Eng **9**(3): 549-554.
- Bancroft, G. N., V. I. Sikavitsas and A. G. Mikos (2003). "Technical Note: Design of a Flow Perfusion Bioreactor System for Bone Tissue Engineering Applications." Tissue Engineering **9**(3): 549-554.
- Bancroft, G. N., V. I. Sikavitsas, J. van den Dolder, T. L. Sheffield, C. G. Ambrose, J. A. Jansen and A. G. Mikos (2002). "Fluid flow increases mineralized matrix deposition in 3D perfusion culture of marrow stromal osteoblasts in a dose-dependent manner." Proc Natl Acad Sci U S A **99**(20): 12600-12605.
- Bhaskar, P. R. (2012). Design of an Axial Flow Bioreactor for Tissue Engineering School of Chemical Engineering Oklahoma State University
- Blan, N. R. and R. K. Birla (2008). "Design and fabrication of heart muscle using scaffold-based tissue engineering." Journal of Biomedical Materials Research Part A **86A**(1): 195-208.
- Bock, A. and U. Reichl (2007). Closed Loop Control of Perfusion Systems in High-density Cell Culture. Cell Technology for Cell Products. R. Smith, Springer Netherlands. **3**: 549-551.
- Burg, K. J. L., M. Delnomdedieu, R. J. Beiler, C. R. Culberson, K. G. Greene, C. R. Halberstadt, W. D. Holder, A. B. Loeb sack, W. D. Roland and G. A. Johnson (2002). "Application of magnetic resonance microscopy to tissue engineering: A polylactide model." Journal of Biomedical Materials Research **61**(3): 380-390.
- Butler, D. L., S. A. Hunter, K. Chokalingam, M. J. Cordray, J. Shearn, N. Juncosa-Melvin, S. Nirmalanandhan and A. Jain (2009). "Using functional tissue engineering and bioreactors to mechanically stimulate tissue-engineered constructs." Tissue Eng Part A **15**(4): 741-749.
- Capuani, F., D. Frenkel and C. P. Lowe (2003). "Velocity fluctuations and dispersion in a simple porous medium." Phys Rev E Stat Nonlin Soft Matter Phys **67**(5 Pt 2): 056306.
- Cartmell, S. H., B. D. Porter, A. J. Garcia and R. E. Guldborg (2003). "Effects of medium perfusion rate on cell-seeded three-dimensional bone constructs in vitro." Tissue Eng **9**(6): 1197-1203.
- Chakraborty, P., B. Roy, P. Bairi and A. K. Nandi (2012). "Improved mechanical and photophysical properties of chitosan incorporated folic acid gel possessing the characteristics of dye and metal ion absorption." J. Mater. Chem. **22**: 20291-20298.
- Chen, G., T. Ushida and T. Tateishi (2000). "A biodegradable hybrid sponge nested with collagen microsponges." Journal of Biomedical Materials Research **51**(2): 273-279.
- Chen, G., T. Ushida and T. Tateishi (2001). "Preparation of poly(-lactic acid) and poly(-lactic-co-glycolic acid) foams by use of ice microparticulates." Biomaterials **22**(18): 2563-2567.
- Chen, G., T. Ushida and T. Tateishi (2002). "Scaffold Design for Tissue Engineering." Macromolecular Bioscience **2**(2): 67-77.
- Chen, H.-C. and Y.-C. Hu (2006). "Bioreactors for tissue engineering." Biotechnology Letters **28**(18): 1415-1423.

- Cheng, M., J. Deng, F. Yang, Y. Gong, N. Zhao and X. Zhang (2003). "Study on physical properties and nerve cell affinity of composite films from chitosan and gelatin solutions." Biomaterials **24**(17): 2871-2880.
- Chu, X. H., X. L. Shi, Z. Q. Feng, J. Y. Gu, H. Y. Xu, Y. Zhang, Z. Z. Gu and Y. T. Ding (2009). "In vitro evaluation of a multi-layer radial-flow bioreactor based on galactosylated chitosan nanofiber scaffolds." Biomaterials **30**(27): 4533-4538.
- Chung, C. A., C. W. Chen, C. P. Chen and C. S. Tseng (2007). "Enhancement of cell growth in tissue-engineering constructs under direct perfusion: Modeling and simulation." Biotechnol Bioeng **97**(6): 1603-1616.
- Cioffi, M., F. Boschetti, M. T. Raimondi and G. Dubini (2006). "Modeling evaluation of the fluid-dynamic microenvironment in tissue-engineered constructs: a micro-CT based model." Biotechnol Bioeng **93**(3): 500-510.
- Cohen, S., T. Dvir and M. Shachar (2012). Pulse-medium perfusion bioreactor with improved mass transport for multiple 3-d cell constructs. **EP1697494 B1**.
- Coletti, F., S. Macchietto and N. Elvassore (2006). "Mathematical modeling of three-dimensional cell cultures in perfusion bioreactors." Industrial & Engineering Chemistry Research **45**(24): 8158-8169.
- Cowin, S. C. (1999). "Bone poroelasticity." J Biomech **32**(3): 217-238.
- Cukierman, E., R. Pankov, D. R. Stevens and K. M. Yamada (2001). "Taking Cell-Matrix Adhesions to the Third Dimension." Science **294**(5547): 1708-1712.
- Curcio, E., P. Macchiarini and L. De Bartolo (2010). "Oxygen mass transfer in a human tissue-engineered trachea." Biomaterials **31**(19): 5131-5136.
- de Kloe, J., A. van der Steen, H. Öksüzoglu and H. Dijkstra (2002). "A Fully Implicit Parallel Ocean Model Using MUMPS." The Journal of Supercomputing **23**(2): 167-183.
- Devarapalli, M., B. J. Lawrence and S. V. Madhally (2009). "Modeling nutrient consumptions in large flow-through bioreactors for tissue engineering." Biotechnol Bioeng **103**(5): 1003-1015.
- Dias, M. R., P. R. Fernandes, J. M. Guedes and S. J. Hollister (2012). "Permeability analysis of scaffolds for bone tissue engineering." J Biomech **45**(6): 938-944.
- Discher, D. E., D. J. Mooney and P. W. Zandstra (2009). "Growth factors, matrices, and forces combine and control stem cells." Science **324**(5935): 1673-1677.
- Dubois, J., L. Tremblay, M. Lepage and P. Vermette (2011). "Flow Dynamics Within a Bioreactor for Tissue Engineering by Residence Time Distribution Analysis Combined With Fluorescence and Magnetic Resonance Imaging to Investigate Forced Permeability and Apparent Diffusion Coefficient in a Perfusion Cell Culture Chamber." Biotechnology and Bioengineering **108**(10): 2488-2498.
- Dvir T, B. N., Shachar M, Cohen S. (2006). "A novel perfusion bioreactor providing a homogenous milieu for tissue regeneration." Tissue Eng. **12**(10): 2843-2852.
- Elliott, D. M., D. A. Narmoneva and L. A. Setton (2002). "Direct Measurement of the Poisson's Ratio of Human Patella Cartilage in Tension." J Biomech Eng **124**(2): 223-228.
- Fogler, H. S. (2006). Elements of chemical reaction engineering. Upper Saddle River, NJ, Prentice Hall.
- Frerich, B. (2011). Perfusable Bioreactor for the Production of Human or Animal Tissues. **US20110091926A1**.

- Fung, Y. C. (1993). Biomechanics: Mechanical Properties of Living Tissues. New York, Springer.
- Gomes, M. E., C. M. Bossano, C. M. Johnston, R. L. Reis and A. G. Mikos (2006). "In Vitro Localization of Bone Growth Factors in Constructs of Biodegradable Scaffolds Seeded with Marrow Stromal Cells and Cultured in a Flow Perfusion Bioreactor " Tissue Engineering **12**(1): 177-188.
- Gooch, K. J., J. H. Kwon, T. Blunk, R. Langer, L. Freed and E. G. Vunjak-Novakovic (2001). "Effects of mixing intensity on tissue-engineered cartilage." Biotechnology and Bioengineering **72**(4): 402-407.
- Goulet RW, G. S., Ciarelli MJ, Kuhn JL, Brown MB, Feldkamp LA. (1994). "The relationship between the structural and orthogonal compressive properties of trabecular bone." J Biomech. **27**(4): 375-539.
- Griffith, L. G. and G. Naughton (2002). "Tissue Engineering--Current Challenges and Expanding Opportunities." Science **295**(5557): 1009-1014.
- Haga, J. H., Y. S. Li and S. Chien (2007). "Molecular basis of the effects of mechanical stretch on vascular smooth muscle cells." J Biomech **40**(5): 947-960.
- Han, M.-J. (2000). "Biodegradable membranes for the controlled release of progesterone. 1. Characterization of membrane morphologies coagulated from PLGA/progesterone/DMF solutions." Journal of Applied Polymer Science **75**(1): 60-67.
- Harris, L. D., B.-S. Kim and D. J. Mooney (1998). "Open pore biodegradable matrices formed with gas foaming." Journal of Biomedical Materials Research **42**(3): 396-402.
- Haugh, M. G., C. M. Murphy and F. J. O'Brien (2010). "Novel freeze-drying methods to produce a range of collagen-glycosaminoglycan scaffolds with tailored mean pore sizes." Tissue Eng Part C Methods **16**(5): 887-894.
- Hayashi, K. (2003). Biomechanics of soft tissue in cardiovascular systems (eds Holzapfel, G. & Ogden, R. W.). New York, Springer
- Hellmich, C. and F. J. Ulm (2005). "Drained and undrained poroelastic properties of healthy and pathological bone: A poro-micromechanical investigation." Transport in Porous Media **58**(3): 243-268.
- Heydarkhan-Hagvall, S., M. Esguerra, G. Helenius, R. Sapperberg, B. R. Johansson and B. Risberg (2006). "Production of Extracellular Matrix Components in Tissue-Engineered Blood Vessels." Tissue Engineering **12**(4): 831-842.
- Hidalgo-Bastida, L. A., S. Thirunavukkarasu, S. Griffiths, S. H. Cartmell and S. Naire (2012). "Modeling and design of optimal flow perfusion bioreactors for tissue engineering applications." Biotechnology and Bioengineering **109**(4): 1095-1099.
- Hollister, S. J. and C. Y. Lin (2007). "Computational design of tissue engineering scaffolds." Computer Methods in Applied Mechanics and Engineering **196**(31-32): 2991-2998.
- Hong, J. K. and S. V. Madhally (2011). "Next generation of electrosprayed fibers for tissue regeneration." Tissue Eng Part B Rev **17**(2): 125-142.
- Hosseinkhani, H., Y. Inatsugu, Y. Hiraoka, S. Inoue and Y. Tabata (2005). "Perfusion culture enhances osteogenic differentiation of rat mesenchymal stem cells in collagen sponge reinforced with poly(glycolic Acid) fiber." Tissue Eng **11**(9-10): 1476-1488.

- Huang, Y., S. Onyeri, M. Siewe, A. Moshfeghian and S. V. Madihally (2005). "In vitro characterization of chitosan-gelatin scaffolds for tissue engineering." Biomaterials **26**(36): 7616-7627.
- Huang, Y., S. Onyeri, M. Siewe, A. Moshfeghian and S. V. Madihally (2005). "In vitro characterization of chitosan-gelatin scaffolds for tissue engineering." Biomaterials **26**(36): 7616-7627.
- Hutmacher, D. W. and H. Singh (2008). "Computational fluid dynamics for improved bioreactor design and 3D culture." Trends Biotechnol **26**(4): 166-172.
- Innocentini, M. D. M., V. R. Salvini, A. Macedo and V. C. Pandolfelli (1999). "Prediction of ceramic foams permeability using Ergun's equation." Materials Research **2**: 283-289.
- Ishaug-Riley, S. L., G. M. Crane-Kruger, M. J. Yaszemski and A. G. Mikos (1998). "Three-dimensional culture of rat calvarial osteoblasts in porous biodegradable polymers." Biomaterials **19**(15): 1405-1412.
- Ishaug, S. L., G. M. Crane, M. J. Miller, A. W. Yasko, M. J. Yaszemski and A. G. Mikos (1997). "Bone formation by three-dimensional stromal osteoblast culture in biodegradable polymer scaffolds." J Biomed Mater Res **36**(1): 17-28.
- Iyer, P., K. J. Walker and S. V. Madihally (2012). "Increased matrix synthesis by fibroblasts with decreased proliferation on synthetic chitosan-gelatin porous structures." Biotechnol Bioeng **109**(5): 1314-1325.
- Jackson, G. W. and D. F. James (1986). "The permeability of fibrous porous media." The Canadian Journal of Chemical Engineering **64**(3): 364-374.
- Jacob, B. (1988). Dynamics of Fluid in Porous Media. New York, American Elsevier Publishing Company, Inc.
- Janorkar, A. V., L. M. Harris, B. S. Murphey and B. L. Sowell (2011). "Use of three-dimensional spheroids of hepatocyte-derived reporter cells to study the effects of intracellular fat accumulation and subsequent cytokine exposure." Biotechnol Bioeng **108**(5): 1171-1180.
- Jones, A. C., C. H. Arns, A. P. Sheppard, D. W. Hutmacher, B. K. Milthorpe and M. A. Knackstedt (2007). "Assessment of bone ingrowth into porous biomaterials using MICRO-CT." Biomaterials **28**(15): 2491-2504.
- Kelly, W. J. (2008). "Using computational fluid dynamics to characterize and improve bioreactor performance." Biotechnology and Applied Biochemistry **049**(4): 225-238.
- Khayyeri, H., S. Checa, M. Tagil, F. J. O'Brien and P. J. Prendergast (2010). "Tissue differentiation in an in vivo bioreactor: in silico investigations of scaffold stiffness." J Mater Sci Mater Med **21**(8): 2331-2336.
- Khor, E. and L. Y. Lim (2003). "Implantable applications of chitin and chitosan." Biomaterials **24**(13): 2339-2349.
- Kim B.S., B. C.E. and A. A. (2000). "Biomaterials for tissue engineering." World J Urol. **18**(1): 2-9.
- Kim, B. S., A. J. Putnam, T. J. Kulik and D. J. Mooney (1998). "Optimizing seeding and culture methods to engineer smooth muscle tissue on biodegradable polymer matrices." Biotechnol Bioeng **57**(1): 46-54.



- Kim, E., F. Guilak and M. A. Haider (2008). "The dynamic mechanical environment of the chondrocyte: a biphasic finite element model of cell-matrix interactions under cyclic compressive loading." J Biomech Eng **130**(6): 061009.
- Kim, G. M., K. H. Le, S. M. Giannitelli, Y. J. Lee, A. Rainer and M. Trombetta (2013). "Electrospinning of PCL/PVP blends for tissue engineering scaffolds." J Mater Sci Mater Med **24**(6): 1425-1442.
- Kim, J. and T. Ma (2012). "Bioreactor strategy in bone tissue engineering: pre-culture and osteogenic differentiation under two flow configurations." Tissue Eng Part A **18**(21-22): 2354-2364.
- Kim, S. S., C. A. Sundback, S. Kaihara, M. S. Benvenuto, B.-S. Kim, D. J. Mooney and J. P. Vacanti. (2000). "Dynamic Seeding and in Vitro Culture of Hepatocytes in a Flow Perfusion System." Tissue Engineering **6**(1): 39 - 44.
- Knebel, G. and S. Muehlfriedel (2011). Bioreactor and Method for Cultivating Cells and Tissues.
- Ko, H. C., B. K. Milthorpe and C. D. McFarland (2007). "Engineering thick tissues--the vascularisation problem." Eur Cell Mate **14**: 1-19.
- Koponen, A., D. Kandhai, E. Hellen, M. Alava, A. Hoekstra, M. Kataja, K. Niskanen, P. Slood and J. Timonen (1998). "Permeability of three-dimensional random fiber webs." Physical Review Letters **80**(4): 716-719.
- Koponen, A., M. Kataja and J. Timonen (1997). "Permeability and effective porosity of porous media." Physical Review E **56**(3): 3319-3325.
- Kuijpers, A. J., G. H. M. Engbers, J. Feijen, S. C. De Smedt, T. K. L. Meyvis, J. Demeester, J. Krijgsveld, S. A. J. Zaat and J. Dankert (1999). "Characterization of the Network Structure of Carbodiimide Cross-Linked Gelatin Gels." Macromolecules **32**(10): 3325-3333.
- Lawrence, B., J. Beene, S. Madihally and R. Lewis (2004). "Incorporating Nonideal Reactors in a Junior-Level Course using Computational Fluid Dynamics (CFD)." Chemical Engineering Education **38**(2): 136-141.
- Lawrence, B. J., M. Devarapalli and S. V. Madihally (2009). "Flow dynamics in bioreactors containing tissue engineering scaffolds." Biotechnol Bioeng **102**(3): 935-947.
- Lawrence, B. J., E. L. Maase, H. K. Lin and S. V. Madihally (2009). "Multilayer composite scaffolds with mechanical properties similar to small intestinal submucosa." J Biomed Mater Res A **88**(3): 634-643.
- Lawrence, B. J. and S. V. Madihally (2008). "Cell colonization in degradable 3D porous matrices." Cell Adh Migr **2**(1): 9-16.
- Leclerc, E., Y. Sakai and T. Fujii (2004). "Microfluidic PDMS (Polydimethylsiloxane) Bioreactor for Large-Scale Culture of Hepatocytes." Biotechnology Progress **20**(3): 750-755.
- Li, S., H. Garreau and M. Vert (1990). "Structure-property relationships in the case of the degradation of massive aliphatic poly-( $\alpha$ -hydroxy acids) in aqueous media." Journal of Materials Science: Materials in Medicine **1**(3): 123-130.
- Ma, J., H. Wang, B. He and J. Chen (2001). "A preliminary in vitro study on the fabrication and tissue engineering applications of a novel chitosan bilayer material as a scaffold of human neonatal dermal fibroblasts." Biomaterials **22**(4): 331-336.
- Ma, T. (2011). Dual-Chamber Perfusion Bioreactor for Orthopedic Tissue Interface and Methods of use. **US20110229970A1**.

- Madhally, S. V. (2010). Principles of Biomedical Engineering, Artech House Publishers.
- Mahapatro, A. and D. Singh (2011). "Biodegradable nanoparticles are excellent vehicle for site directed in-vivo delivery of drugs and vaccines." Journal of Nanobiotechnology **9**(1): 55.
- Maquet, V. and R. Jerome (1997). "Design of macroporous biodegradable polymer scaffolds for cell transplantation." Materials Science Forum **250**(15): 15-42.
- Martin, I., D. Wendt and M. Heberer (2004). "The role of bioreactors in tissue engineering." Trends in Biotechnology **22**(2): 80-86.
- Martin, Y. and P. Vermette (2005). "Bioreactors for tissue mass culture: Design, characterization, and recent advances." Biomaterials **26**(35): 7481-7503.
- Mazariegos, G. V., J. F. Patzer, R. C. Lopez, M. Giraldo, M. E. DeVera, T. A. Grogan, Y. Zhu, M. L. Fulmer, B. P. Amiot and D. J. Kramer (2002). "First Clinical Use of a Novel Bioartificial Liver Support System (BLSS)†." American Journal of Transplantation **2**(3): 260-266.
- McCoy, R. J. and F. J. O'Brien (2010). "Influence of shear stress in perfusion bioreactor cultures for the development of three-dimensional bone tissue constructs: a review." Tissue Eng Part B Rev **16**(6): 587-601.
- Middleton, J. C. and A. J. Tipton (1998). Synthetic biodegradable polymers as medical devices. Med. Plastics Biomater. **3**: 30.
- Mooney, D. J., D. F. Baldwin, N. P. Suh, J. P. Vacanti and R. Langer (1996). "Novel approach to fabricate porous sponges of poly(-lactic-co-glycolic acid) without the use of organic solvents." Biomaterials **17**(14): 1417-1422.
- Moroni, L., J. R. de Wijn and C. A. van Blitterswijk (2006). "3D fiber-deposited scaffolds for tissue engineering: influence of pores geometry and architecture on dynamic mechanical properties." Biomaterials **27**(7): 974-985.
- Moshfeghian, A., J. Tillman and S. V. Madhally (2006). "Characterization of emulsified chitosan-PLGA matrices formed using controlled-rate freezing and lyophilization technique." J Biomed Mater Res A **79**(2): 418-430.
- Moshfeghian, A., J. Tillman and S. V. Madhally (2006). "Characterization of emulsified chitosan-PLGA matrices formed using controlled-rate freezing and lyophilization technique." Journal of Biomedical Materials Research Part A **79A**(2): 418-430.
- Nam, Y. S. and T. G. Park (1999). "Porous biodegradable polymeric scaffolds prepared by thermally induced phase separation." Journal of Biomedical Materials Research **47**(1): 8-17.
- Niklason, L. E., J. Gao, W. M. Abbott, K. K. Hirschi, S. Houser, R. Marini and R. Langer (1999). "Functional arteries grown in vitro." Science **284**(5413): 489-493.
- Ochoa, I., J. A. Sanz-Herrera, J. M. Garcia-Aznar, M. Doblare, D. M. Yunos and A. R. Boccaccini (2009). "Permeability evaluation of 45S5 Bioglass-based scaffolds for bone tissue engineering." J Biomech **42**(3): 257-260.
- OPTN. (2012). "Waiting list candidates for organ transplant " Retrieved 22 April 2012, 2012, from <http://optn.transplant.hrsa.gov/data/>.
- Palsson, C.-A. P. a. B. O. (1996). "Cell Growth and Differentiation on Feeder Layers Is Predicted to be influenced by Bioreactor Geometry." Biotechnol Bioeng **50**: 479-492.
- Park, Y. J., K. H. Nam, S. J. Ha, C. M. Pai, C. P. Chung and S. J. Lee (1997). "Porous poly(-lactide) membranes for guided tissue regeneration and controlled drug delivery: membrane fabrication and characterization." Journal of Controlled Release **43**(2-3): 151-160.

- Parsons, J. R. (1998). Cartilage. New York, Chapman & Hall.
- Patrachari, A. R., J. T. Podichetty and S. V. Madihally (2012). "Application of computational fluid dynamics in tissue engineering." J Biosci Bioeng **114**(2): 123-132.
- Pennella, F., G. Cerino, D. Massai, D. Gallo, G. Falvo D'Urso Labate, A. Schiavi, M. A. Deriu, A. Audenino and U. Morbiducci (2013). "A survey of methods for the evaluation of tissue engineering scaffold permeability." Ann Biomed Eng **41**(10): 2027-2041.
- Perrin, D. E. and J. P. English (1997). Polyglycolide and polylactide. New York, Harwood Academic Publishers.
- Ploss, A., S. R. Khetani, C. T. Jones, A. J. Syder, K. Trehan, V. A. Gaysinskaya, K. Mu, K. Ritola, C. M. Rice and S. N. Bhatia (2010). "Persistent hepatitis C virus infection in microscale primary human hepatocyte cultures." Proc Natl Acad Sci U S A **107**(7): 3141-3145.
- Podichetty, J. T., P. R. Bhaskar, A. Khalf and S. V. Madihally (2014). "Modeling Pressure Drop Using Generalized Scaffold Characteristics in an Axial-Flow Bioreactor for Soft Tissue Regeneration." Ann Biomed Eng. **42**(6): 1319-1330
- Podichetty, J. T., D. V. Dhane and S. V. Madihally (2012). "Dynamics of diffusivity and pressure drop in flow-through and parallel-flow bioreactors during tissue regeneration." Biotechnol Prog **28**(4): 1045-1054.
- Podichetty, J. T. and S. V. Madihally (2014). "Modeling of porous scaffold deformation induced by medium perfusion." Journal of Biomedical Materials Research Part B: Applied Biomaterials **102**(4): 737-748.
- Pok, S., D. V. Dhane and S. V. Madihally (2013). "Computational simulation modelling of bioreactor configurations for regenerating human bladder." Comput Methods Biomech Biomed Engin **16**(8): 840-851.
- Porter, B., R. Zael, H. Stockman, R. Guldborg and D. Fyhrie (2005). "3-D computational modeling of media flow through scaffolds in a perfusion bioreactor." J Biomech **38**(3): 543-549.
- Pu, F., N. P. Rhodes, Y. Bayon, R. Chen, G. Brans, R. Benne and J. A. Hunt (2010). "The use of flow perfusion culture and subcutaneous implantation with fibroblast-seeded PLLA-collagen 3D scaffolds for abdominal wall repair." Biomaterials **31**(15): 4330-4340.
- Pulieri, E., V. Chiono, G. Ciardelli, G. Vozzi, A. Ahluwalia, C. Domenici, F. Vozzi and P. Giusti (2008). "Chitosan/gelatin blends for biomedical applications." Journal of Biomedical Materials Research Part A **86A**(2): 311-322.
- Rademacher, A., M. Paulitschke, R. Meyer and R. Hetzer (2001). "Endothelialization of PTFE vascular grafts under flow induces significant cell changes." Int J Artif Organs **24**(4): 235-242.
- Raghunath, J., J. Rollo, K. M. Sales, P. E. Butler and A. M. Seifalian (2007). "Biomaterials and scaffold design: key to tissue-engineering cartilage." Biotechnol Appl Biochem **46**(Pt 2): 73-84.
- Raimondi, M. T., M. Moretti, M. Cioffi, C. Giordano, F. Boschetti, K. Lagana and R. Pietrabissa (2006). "The effect of hydrodynamic shear on 3D engineered chondrocyte systems subject to direct perfusion." Biorheology **43**(3-4): 215-222.
- Ratakonda, S., U. M. Sridhar, R. R. Rhinehart and S. V. Madihally (2012). "Assessing viscoelastic properties of chitosan scaffolds and validation with cyclical tests." Acta Biomater **8**(4): 1566-1575.
- Ratner, B. D., A. S. Hoffman, F. J. Shoen and J. E. Lemons (1996). Biomaterials science:an introduction to materials in medicine. Waltham, MA, Academic Press.

- Rong Huei, C. and H.-D. Hwa (1996). "Effect of molecular weight of chitosan with the same degree of deacetylation on the thermal, mechanical, and permeability properties of the prepared membrane." Carbohydrate Polymers **29**(4): 353-358.
- Ruan, Y., H. Lin, J. Yao, Z. Chen and Z. Shao (2011). "Preparation of 3D Fibroin/Chitosan Blend Porous Scaffold for Tissue Engineering Via a Simplified Method." Macromolecular Bioscience **11**(3): 419-426.
- Saad, Y. and M. H. Schultz (1986). "GMRES: a generalized minimal residual algorithm for solving nonsymmetric linear systems." SIAM J. Sci. Stat. Comput. **7**(3): 856-869.
- Salem, A. K., R. Stevens, R. G. Pearson, M. C. Davies, S. J. B. Tendler, C. J. Roberts, P. M. Williams and K. M. Shakesheff (2002). "Interactions of 3T3 fibroblasts and endothelial cells with defined pore features." Journal of Biomedical Materials Research **61**(2): 212-217.
- Salerno, A., M. Oliviero, E. Di Maio, S. Iannace and P. A. Netti (2007). "Design and preparation of  $\mu$ -bimodal porous scaffold for tissue engineering." Journal of Applied Polymer Science **106**(5): 3335-3342.
- Sanz-Herrera, J. A., J. M. Garcia-Aznar and M. Doblare (2009). "A mathematical approach to bone tissue engineering." Philos Transact A Math Phys Eng Sci **367**(1895): 2055-2078.
- Schoof, H., J. Apel, I. Heschel and G. Rau (2001). "Control of pore structure and size in freeze-dried collagen sponges." Journal of Biomedical Materials Research **58**(4): 352-357.
- Schugens, C., V. Maquet, C. Grandfils, R. Jerome and P. Teyssie (1996). "Biodegradable and macroporous polylactide implants for cell transplantation: 1. Preparation of macroporous polylactide supports by solid-liquid phase separation." Polymer **37**(6): 1027-1038.
- Schulz, R. and B. Augustinus (2005). Method and Bioreactor for the Cultivation and Stimulation of Three-Dimensional vital and Mechanically-Resistant Cell Transplants. **CA2543374A**.
- Seal, B. L., T. C. Otero and A. Panitch (2001). "Polymeric biomaterials for tissue and organ regeneration." Materials Science and Engineering: R: Reports **34**(4-5): 147-230.
- Sengers, B. G., C. W. Oomens and F. P. Baaijens (2004). "An integrated finite-element approach to mechanics, transport and biosynthesis in tissue engineering." J Biomech Eng **126**(1): 82-91.
- Sethuraman, V., K. Makornkaewkeyoon, A. Khalf and S. V. Madihally (2013). "Influence of scaffold forming techniques on stress relaxation behavior of polycaprolactone scaffolds." Journal of Applied Polymer Science **130**(6): 4237-4244.
- Shimko, D. A., V. F. Shimko, E. A. Sander, K. F. Dickson and E. A. Nauman (2005). "Effect of porosity on the fluid flow characteristics and mechanical properties of tantalum scaffolds." J Biomed Mater Res B Appl Biomater **73**(2): 315-324.
- Sikavitsas, V. I., G. N. Bancroft, H. L. Holtorf, J. A. Jansen and A. G. Mikos (2003). "Mineralized matrix deposition by marrow stromal osteoblasts in 3D perfusion culture increases with increasing fluid shear forces." Proceedings of the National Academy of Sciences **100**(25): 14683-14688.
- Silver, F. H., D. L. Christiansen and C. M. Buntin (1989). "Mechanical properties of the aorta: a review." Crit Rev Biomed Eng **17**(4): 323-358.
- Singh, D. K. and A. R. Ray (1997). "Radiation-induced grafting of N,N'-dimethylaminoethylmethacrylate onto chitosan films." Journal of Applied Polymer Science **66**(5): 869-877.
- Singh, V. (2003). Disposable Perfusion Bioreactor for Cell Culture. **US006544788B2**.

- Sittinger, M. and J. Bujia (1999). Process for Producing an Implant from Cell Cultures. **US005891455A**.
- Sodian, R., T. Lemke, C. Fritsche, S. P. Hoerstrup, P. Fu, E. V. Potapov, H. Hausmann and R. Hetzer (2002). "Tissue-engineering bioreactors: a new combined cell-seeding and perfusion system for vascular tissue engineering." Tissue Eng **8**(5): 863-870.
- Stephens, J. S., J. A. Cooper, F. R. Phelan, Jr. and J. P. Dunkers (2007). "Perfusion flow bioreactor for 3D in situ imaging: investigating cell/biomaterials interactions." Biotechnol Bioeng **97**(4): 952-961.
- Suarez Arriaga, M. C. (2012). A tensorial formulation in four dimensions of thermoporoelastic phenomena. Mathematical and Numerical Modeling in Porous Media: Applications in Geosciences. M. A. Diaz Viera, P. Sahay, M. Coronado and T. A. O., CRC Press 53-62.
- Swartz, M. A. and M. E. Fleury (2007). "Interstitial flow and its effects in soft tissues." Annu Rev Biomed Eng **9**: 229-256.
- Swartz, M. A., A. Kaipainen, P. A. Netti, C. Brekken, Y. Boucher, A. J. Grodzinsky and R. K. Jain (1999). "Mechanics of interstitial-lymphatic fluid transport: theoretical foundation and experimental validation." J Biomech **32**(12): 1297-1307.
- Taluja, A., Y. S. Youn and Y. H. Bae (2007). "Novel approaches in microparticulate PLGA delivery systems encapsulating proteins." J. Mater. Chem. **17**: 4002-4014.
- Tilton, J. N. (2007). Fluid and Particle Dynamics. Perry's Chemical Engineers' Handbook. D. W. Green and R. R. Perry, McGraw-Hill Professional. **Eighth Edition**.
- Timmins, N. E., A. Scherberich, J. A. Fruh, M. Heberer, I. Martin and M. Jakob (2007). "Three-dimensional cell culture and tissue engineering in a T-CUP (tissue culture under perfusion)." Tissue Eng **13**(8): 2021-2028.
- Trepats, X., L. Deng, S. S. An, D. Navajas, D. J. Tschumperlin, W. T. Gerthoffer, J. P. Butler and J. J. Fredberg (2007). "Universal physical responses to stretch in the living cell." Nature **447**(7144): 592-595.
- Truskey, G. A., F. Yuan and D. F. Katz (2004). Transport Phenomena in Biological Systems. Upper Saddle River, NJ, Pearson Prentice Hall: 317-321.
- Upton M.T. and Flickinger T.J. (2006). Cell Culture Spinner Flasks. **US6991933B1**.
- Vunjak-Novakovic, G., B. Obradovic, I. Martin, P. M. Bursac, R. Langer and L. E. Freed (1998). "Dynamic Cell Seeding of Polymer Scaffolds for Cartilage Tissue Engineering." Biotechnology Progress **14**(2): 193-202.
- Weathers, J. P. and J. M. Towler (2012). Scalable Wall Bioreactor for Culture of Plant and Animal Tissues. **US008114664B2**.
- Weise, F., U. Fernekorn, J. Hampl, M. Klett and A. Schober (2013). "Analysis and comparison of oxygen consumption of HepG2 cells in a monolayer and three-dimensional high density cell culture by use of a matrigrid(R)." Biotechnol Bioeng **110**(9): 2504-2512.
- Wendt, D., A. Marsano, M. Jakob, M. Heberer and I. Martin (2003). "Oscillating perfusion of cell suspensions through three-dimensional scaffolds enhances cell seeding efficiency and uniformity." Biotechnology and Bioengineering **84**(2): 205-214.
- Wendt, D., S. Riboldi, M. Cioffi and I. Martin (2011). Bioreactors in Tissue Engineering: Scientific Challenges and Clinical Perspectives, Springer Berlin / Heidelberg: 1-27.

- Whang, K., C. H. Thomas, K. E. Healy and G. Nuber (1995). "A novel method to fabricate bioabsorbable scaffolds." Polymer **36**(4): 837-842.
- Whitaker, S. (1996). "The Forchheimer equation: A theoretical development." Transport in Porous Media **25**(1): 27-61.
- Wiig, H. and M. A. Swartz (2012). "Interstitial fluid and lymph formation and transport: physiological regulation and roles in inflammation and cancer." Physiol Rev **92**(3): 1005-1060.
- Williams, K. A., S. Saini and T. M. Wick (2002). "Computational fluid dynamics modeling of steady-state momentum and mass transport in a bioreactor for cartilage tissue engineering." Biotechnol Prog **18**(5): 951-963.
- Wise, D. L. (1995). Encyclopedic Handbook of Biomaterials and Bioengineering Part A: Materials. New York, Marcel Dekker.
- Wiseman, D. M., A. J. Domb and J. Kost (1998). Handbook of Biodegradable Polymers, Taylor & Francis.
- Woo, S. L.-Y., Gomez M.A. and Akeson W.H. (1985). Mechanical behaviour of soft tissues: Measurements, modifications, injuries and treatment. Norwalk, Appleton Crofts.
- Woo, S. L.-Y. and R. E. Levine (1998). Ligament, tendon and fascia. New York, Chapman & Hall.
- Yang S, Leong KF, Du Z and C. CK (2004). "The Design of Scaffolds for Use in Tissue Engineering. Part I. Traditional Factors " Tissue Engineering **7**(6): 679-689.
- Yang, S. F. (1999). Study on biomimetic artificial bone, Tsinghua University.
- Yeatts, A. B. and J. P. Fisher (2011). "Bone tissue engineering bioreactors: dynamic culture and the influence of shear stress." Bone **48**(2): 171-181.
- Zhao, F. and T. Ma (2005). "Perfusion bioreactor system for human mesenchymal stem cell tissue engineering: dynamic cell seeding and construct development." Biotechnol Bioeng **91**(4): 482-493.
- Zhao, F. and T. Ma (2005). "Perfusion bioreactor system for human mesenchymal stem cell tissue engineering: Dynamic cell seeding and construct development." Biotechnology and Bioengineering **91**(4): 482-493.
- Zhu, X., W. Cui, X. Li and Y. Jin (2008). "Electrospun fibrous mats with high porosity as potential scaffolds for skin tissue engineering." Biomacromolecules **9**(7): 1795-1801.

## APPENDIX A

### STRUCTURAL MECHANICS SIMULATION USING COMSOL MULTIPHYSICS v4.2a

The following is a guide on two-way coupling of *Free and Porous Media Flow Physics* and *Solid Mechanics Physics* in COMSOL Multiphysics v4.2a

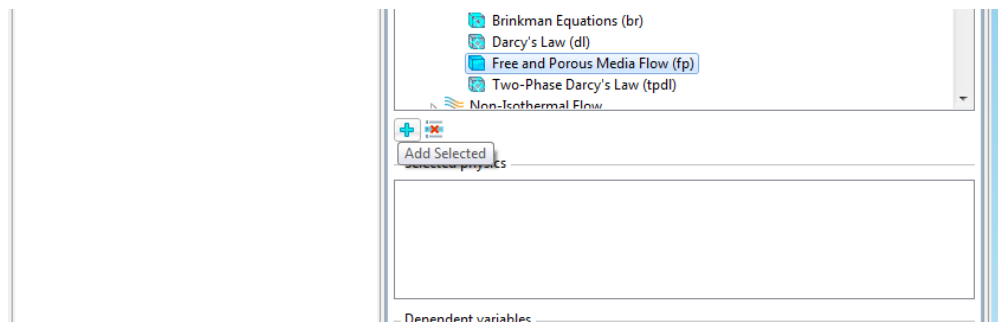
#### Notes:

1. Two or more physics can be coupled using Two-way coupling.
2. The keywords in COMSOL Multiphysics v4.2a is set to **bold** in the modeling instructions below for better understanding.

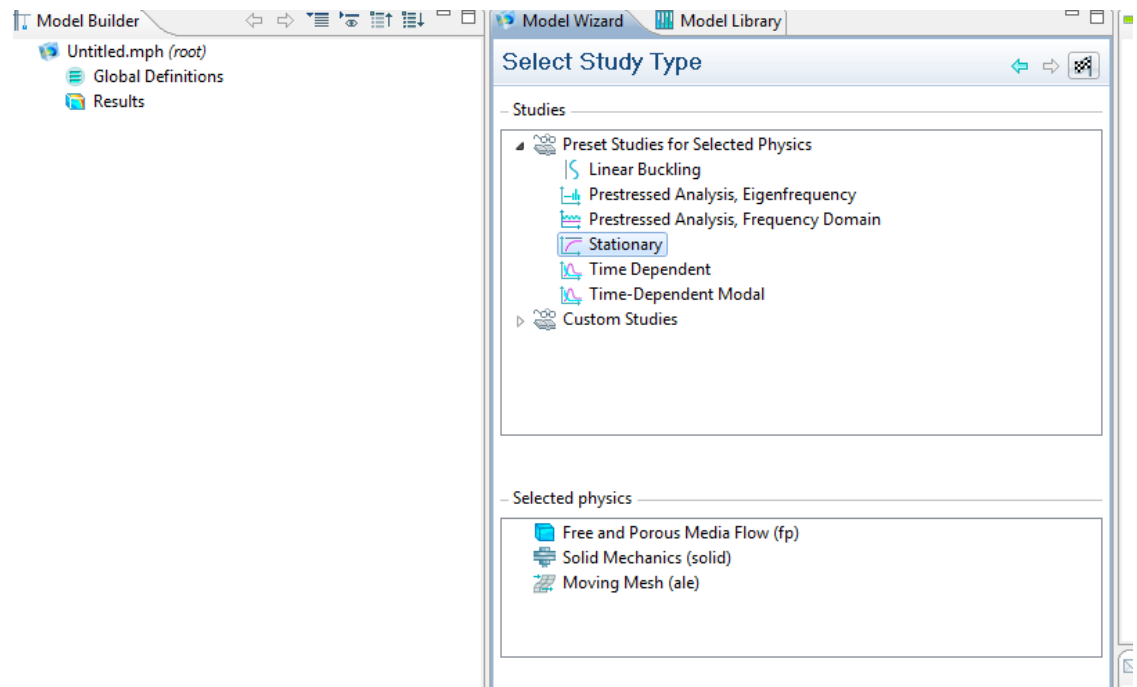
#### Modeling Instructions

##### Step 1: Setting up physics using Model wizard

1. In **model wizard**, select **3D** and click **Next** button beside **Select Space Dimension** menu bar.
2. Under the **Add Physics** tree, select **Fluid Flow > Porous Media and Subsurface Flow > Free and Porous Media Flow (fp)** and click **Add Selected** button as shown in the figure below.



3. Under the **Add Physics** tree, select **Structural Mechanics > Solid Mechanics (solid)** and click **Add Selected** button.
4. Under the **Add Physics** tree, select **Mathematics > Deformed Mesh > Moving Mesh (ale)** and click **Add Selected** button.
5. Click **Next**.
6. Under **Select Study Type** tree, select **Present Studies for Selected Physics > Stationary** and click **Finish** button (checkered flag).



### Step 2: Creating bioreactor Geometry

1. Under **Model Builder** window, click **Model 1 > Geometry 1**.
2. Right click **Geometry 1** and select **Work Plane**.

**Note:** Work Plane is used for drawing 2D objects embedded in 3D. These objects can then be extruded or revolved into the 3<sup>rd</sup> Dimension [1].

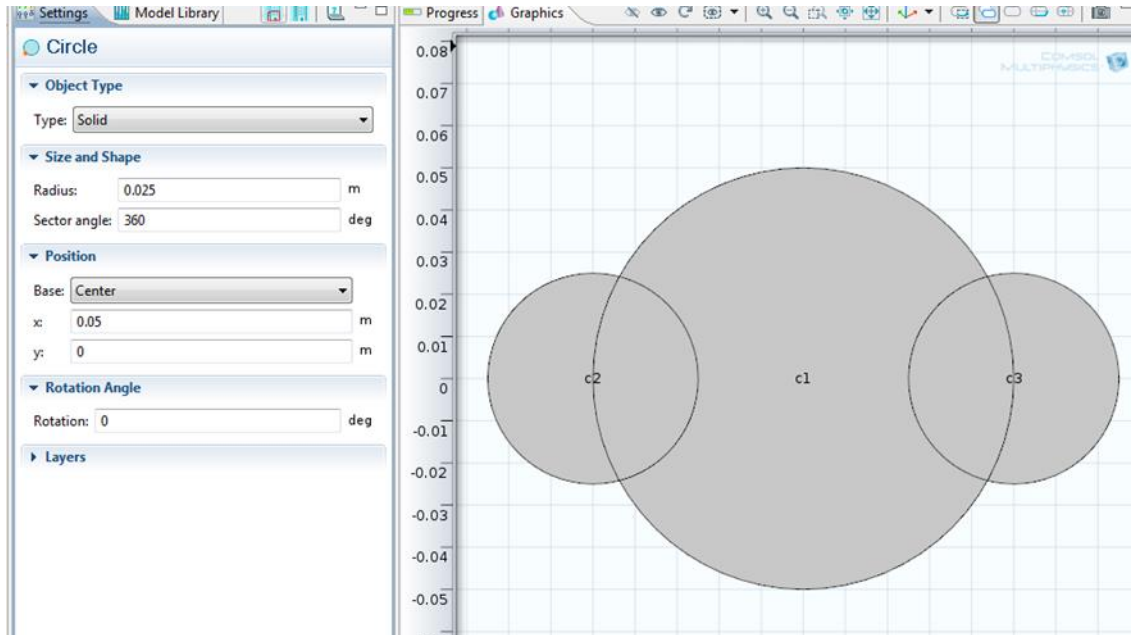
3. Under **Work Plane 1**, right click **Geometry > Circle**.
4. Click on **Circle 1** and in **Settings** window under **Size and Shape** tab, enter **Radius 0.05**.

**Note:** Circle 1 is used for creating the center scaffold domain with a diameter of 10 cm.



5. Again, under **Work Plane 1**, right click **Geometry > Circle**.
6. Click on **Circle 2** and in **Settings** window under **Size and Shape** tab, enter **Radius** 0.025. Under **Position** tab select **Base: Center**, and enter **x: -0.05** and **y: 0**.
7. Again, under **Work Plane 1**, right click **Geometry > Circle**.
8. Click on **Circle 3** and in **Settings** window under **Size and Shape** tab, enter **Radius** 0.025. Under **Position** tab select **Base: Center**, and enter **x: 0.05** and **y: 0**.
9. Click **Build Selected** button on the **Settings** menu bar.

**Note:** Circle 2 and Circle 3 with a diameter of 5 cm represent the non-porous domain. They are positioned 0.05 m and -0.05 (x axis) respectively from the center of the scaffold domain.



10. Right click **Work Plane 1** and select **Extrude**.
  11. Click on **Extrude 1** and in the **Settings** window under **Distance from Work Plane** enter **Distances (m) 0.002**, and click on **Reverse direction** check button.
- Note:** This step would extrude the 2D geometry with a distance of 0.002 m in the negative z axis direction.
12. Right click **Geometry 1** and select **Work Plane**.

13. Under **Work Plane 2**, right click **Geometry** > **Circle**.

14. Click on **Circle 1** and in **Settings** window under **Size and Shape** tab, enter **Radius** 0.003. Under Position window select **Base: Center**, and enter **x: -0.063** and **y: 0**.

**Note:** Circle 1 is used to create an inlet with a radius of 0.003 m, at a distance of 0.063m in the negative x axis direction.

15. Again, under **Work Plane 2**, right click **Geometry** > **Circle**.

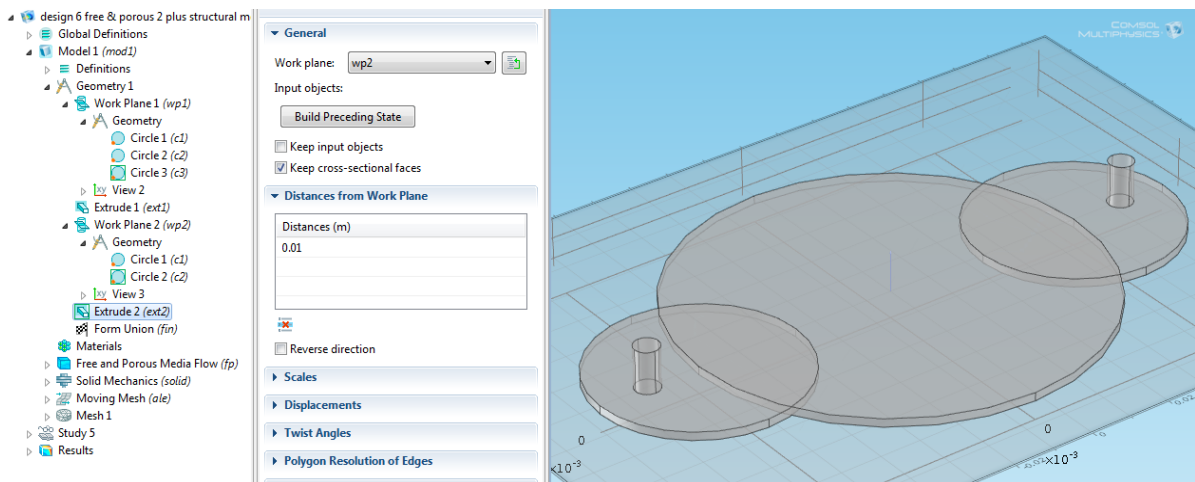
16. Click on **Circle 2** and in **Settings** window under **Size and Shape** tab, enter **Radius** 0.003. Under Position window select **Base: Center**, and enter **x: 0.063** and **y: 0**.

17. Right click **Work Plane 2** and select **Extrude**.

18. Click on **Extrude 2** and under **Distance from Work Plane** enter **Distances (m)** 0.01.

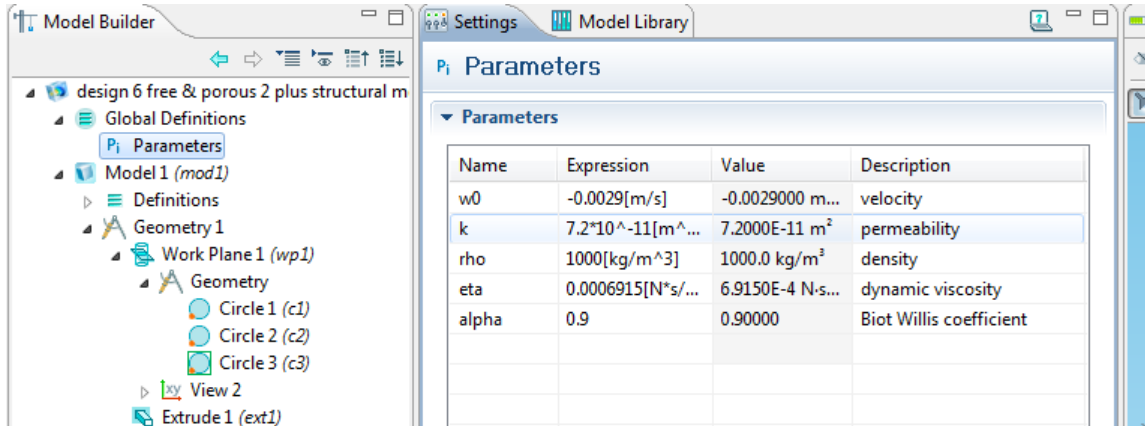
**Note:** This step will extrude Circle 1 and Circle 2 in the positive z direction to a distance of 0.01 m

19. Click **Build all** button on the **Settings** menu bar.



### Step 3: Defining global Parameters

1. Under **Model Builder** window, right click **Global Definitions** and select **Parameters**.
2. Enter the parameters as shown in the figure below.



### Step 4: Setting up Free and Porous Media Flow physics

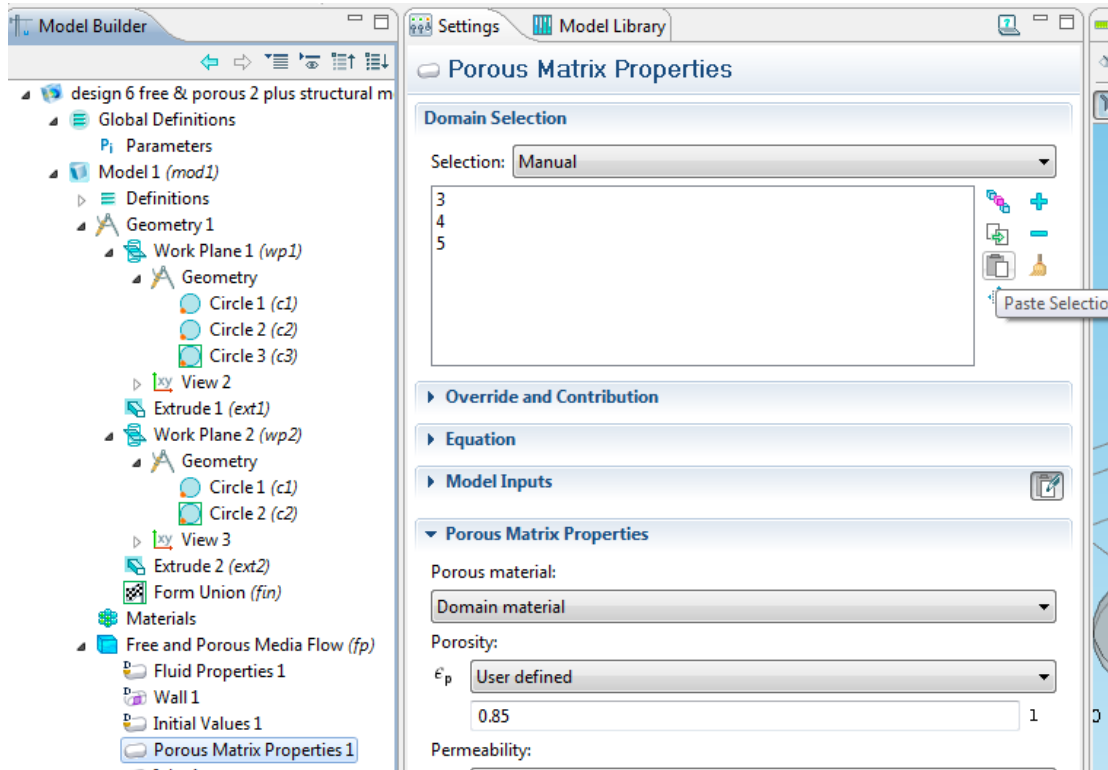
1. Under **Model Builder** window, click **Free and Porous Media Flow (fp)**.
2. Under **Model Builder** window, Click **Free and Porous Media Flow > Fluid Properties 1**, in **Fluids Properties** tab enter **Density**: rho and **Dynamic viscosity**: eta.

**Note:** Double click Free and Porous Media Flow to expand the tree.

3. Right click **Free and Porous Media Flow** and select **Porous Matrix Properties**.

**Note:** The current geometry is divided into 7 domains and 42 boundaries. Domains 3,4,5 are the porous scaffold region and the rest 1,2,6,7 are the free flow region. Domains can be either entered manually using the paste selection button or by clicking the domain in the Graphics window followed by clicking the add button in the Domain Selection tab.

- Click **Porous Matrix Properties**, in **Settings** window under **selection: Manual** click **paste selection** button and enter 3,4,5.



- Under **Porous Matrix Properties** enter **Porosity: 0.85** and **Permeability: k**.
- Right click **Free and Porous Media Flow** and select **inlet**.
- Click **inlet 1**, in **Settings** window under **selection: Manual** click **paste selection** button and enter 8.

**Note:** Boundary 8 is the topmost boundary on the inlet domain used for fluid inflow.

- In Boundary Condition tab, select **Boundary condition: Velocity**.
- Click **Velocity field**, enter  $\mathbf{u}_0: 0, 0, w_0$  (see parameters).

**Note:** Inlet velocity is calculated by dividing volumetric flow rate with inlet cross section area. Since the flow is entering the geometry in the z direction, velocities in x and y direction are zero.  $w_0$  corresponds to 1 ml/min.

10. Right click **Free and Porous Media Flow** and select **outlet**.
11. Click **outlet 1**, in **Settings** window under **selection: Manual** click **paste selection** button and enter 40.
12. In Boundary Condition tab, select **Boundary condition: Pressure, no viscous stress** and enter **Pressure: 0**.

**Note:** Boundary 40 is the topmost boundary in outlet domain. The outlet pressure is set to atmospheric; hence, the gauge pressure would be zero.

Step 5: Setting up **Solid Mechanics** physics

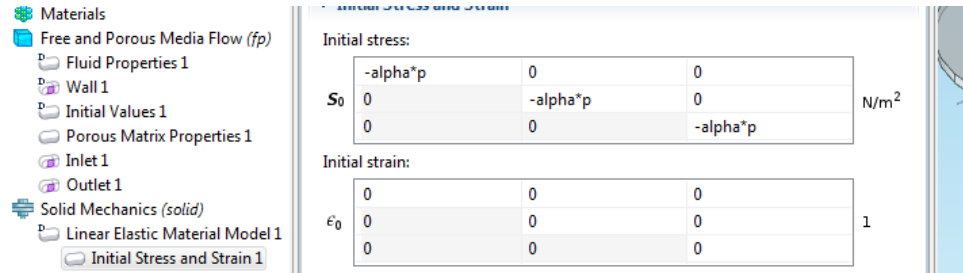
1. Under **Model Builder** window, click **Solid Mechanics (solid)**.
2. Under **Settings** window, in **Domains** tab select **1, 2, 6, 7** and click **Remove from Selection** button.

**Note:** Domains 1,2,6,7 are fluid domain and do not contain any porous media.

3. Under **Model Builder** window, Click **Solid Mechanics > Linear Elastic Material Model**.
4. Click **Linear Elastic Material Model**, in **Settings** window under **Linear Elastic Model** tab, select **Specify: Young's modulus and Poisson's ratio**. Enter **Young's modulus: 200000** and **Poisson's ratio: 0.3**.
5. Enter **Density: 313**.

**One-Way Coupling:** To study the effect of fluid pressure on porous media, the fluid pressure from the Free and Porous Media Flow physics is used as the initial stress on the porous media. The Biot-Wills coefficient ( $\alpha$ ) is multiplied to the pressure tensor (Step 7). Please refer to the Theory of Poroelasticity Interface in Subsurface flow documentation for more details. The fluid stress acting on the fluid-porous media interface (boundaries:12,13,30,33) is defined using the boundary load option (Step 12).

6. Right click **Linear Elastic Material Model** and select **Initial Stress and Strain**.
7. Click **Initial Stress and Strain 1**, in **Settings** window under **Initial Stress and Strain** **tab**, enter **Initial Stress:**  $(-\alpha*p, 0, 0; 0, -\alpha*p, 0; 0, 0, -\alpha*p)$ .



8. Right click **Solid Mechanics**, select **Symmetry**.

**Note:** Symmetry boundary condition represents symmetry in the geometry and load. It's used when the boundary is free in the place and fixed in the out-of- plane direction [1].

9. Click **Symmetry 1**, in **Settings** window under **selection: Manual** click **paste selection** button and enter 14,15,18,19,20,22,23,24,27,28.

**Note:** The above boundaries include the total surface of the porous domain except the fluid-porous media boundaries. The fluid-porous media boundaries are used for assigning boundary load on the porous media (Step 11).

10. Right click **Solid Mechanics**, select **Boundary load**.
11. Click **Boundary load 1**, in **Settings** window under **selection: Manual** click **paste selection** button and enter 12,13,30,33.
12. Under **Force** tab, select **Load type:** Load defined as force per unit area and enter Load:  
 $fp.T\_stressx*dvol\_spatial/dvol$ ,  $fp.T\_stressy*dvol\_spatial/dvol$ ,  
 $fp.T\_stressz*dvol\_spatial/dvol$

**Note:** The expression  $fp.T\_stressx$ , which is the fluid stress in the x direction, is multiplied with  $dvol\_spatial/dvol$  to account for the moving mesh in two-way coupling.

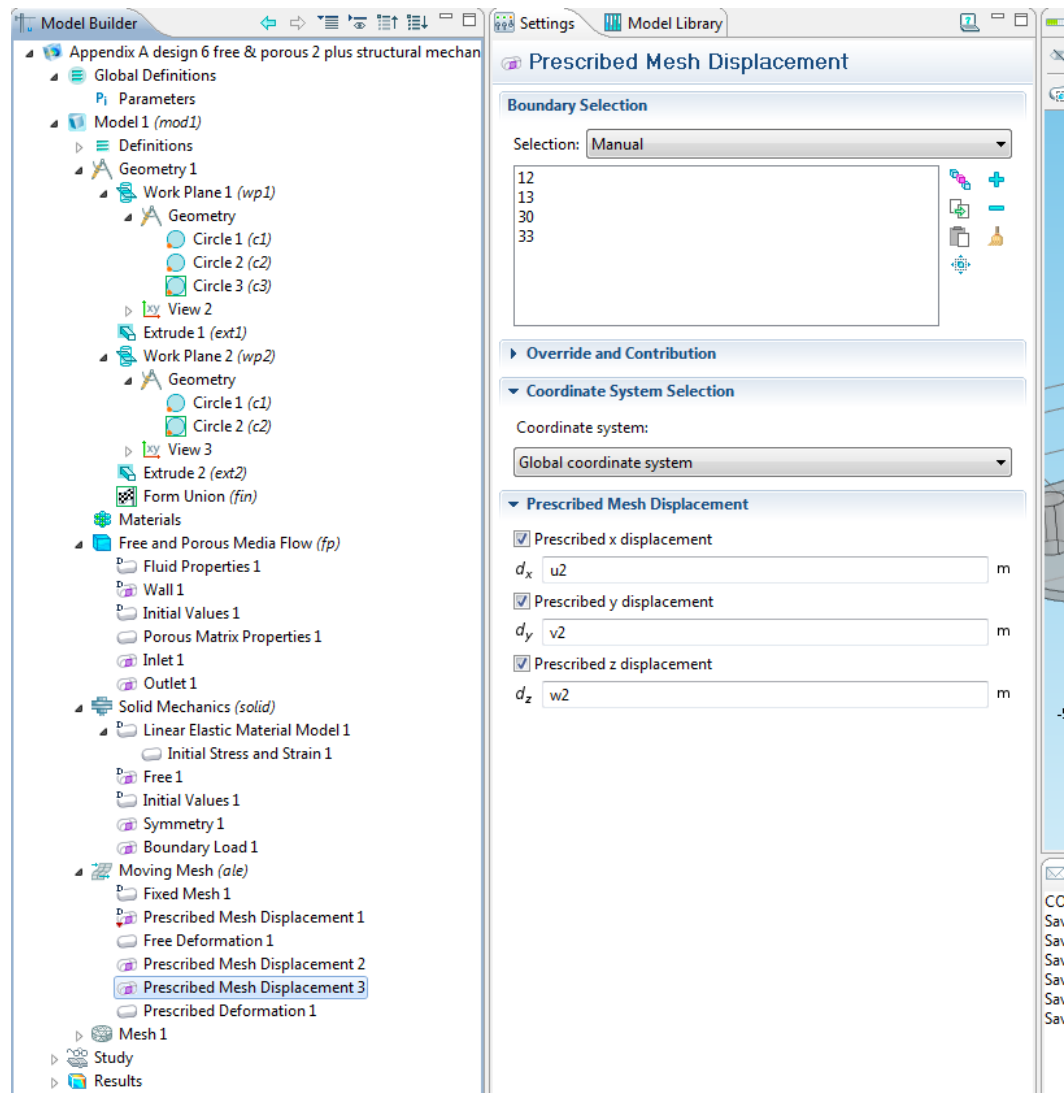
Step 6: Setting up **Moving Mesh** physics for Two-Way coupling

1. Under **Model Builder** window, click **Moving Mesh (ale)**.
2. Right click **Moving Mesh** and select **Free Deformation**.
3. Click **Free Deformation 1**, in **Settings** window under **selection: Manual** click **paste selection** button and enter 1,2,6,7.
4. Right click **Moving Mesh** and select **Prescribed Deformation**.
5. Click **Prescribed Deformation 1**, in **Settings** window under **selection: Manual** click **paste selection** button and enter 3,4,5.
6. Under **Prescribed Mesh Displacement** tab, check enter **dx**: u2, **dy**: v2 and **dz**: w2

**Note:** The porous domains 3,4,5 are set to deform based on the displacements field components from the Solid Mechanics Physics.

7. Right click **Moving Mesh** and select **Prescribed Mesh Displacement**.
8. Click **Prescribed Mesh Displacement 2**, in **Settings** window under **Selection: All Boundaries**.
9. Right click **Moving Mesh** and select **Prescribed Mesh Displacement**.
10. Click **Prescribed Mesh Displacement 3**, in **Settings** window under **Selection: Manual** click **paste selection** button and enter 12,13,30,33.
11. Under **Prescribed Mesh Displacement** tab, check **Prescribed x displacement** , **Prescribed y displacement**, **Prescribed z displacement** and enter **d<sub>x</sub>**: u2, **d<sub>y</sub>**: v2 and **d<sub>z</sub>**: w2

**Note:** The fluid-porous media interface boundaries are set to deform based on the displacements field components from the Solid Mechanics Physics.



**How Two-Way coupling works:** The initial mesh is deformed based on calculations from the Solid Mechanics physics. The new mesh is then used by free and porous media flow physics for calculating new set of results for variables such as pressure and velocity.

### Step 7: Creating a custom asymmetric Mesh

1. Under **Model Builder** window, right click **mesh** > **size**.
2. Right click **Mesh** and select **More Operations** > **Free Triangular**.
3. Click **Free Triangular 1**, in **Settings** window select **Geometric entity level:** Boundary and **Selection:** Manual. Click **Paste Selection** button and enter 8,40



**Note:** Boundaries 8, 40 are the topmost boundaries of the inlet and outlet. These boundaries are meshed first, such that the entire inlet and outlet domains (2 and 7) can then be swept downwards using the swept mesh option. (Step 7)

4. Right click **Free Triangular 1** and select **Distribution**.
5. Click **Distribution1**, in **Settings** window under **Selection:** Manual. Click **Paste Selection** button and enter 9,10,13,16,71,72,75,78

**Note:** Edges 9,10,13,16,71,72,75,78 are the used for meshing the inlet and outlet boundaries.

6. Under **Distribution** tab, select **Distribution properties:** Fixed number of elements. Enter **Number of elements:** 5.
7. Right click **Mesh** and select **Swept**.
8. Click **Swept 1**, in **Settings** window select **Geometric entity level:** Domain and **Selection:** Manual. Click **Paste Selection** button and enter 2,7
9. Under **Source Faces** tab, under **Selections:** Manual. Click **Paste Selection** button and enter 8,40.
10. Under **Destination Faces** tab, under **Selections:** Manual. Click **Paste Selection** button and enter 7,39.

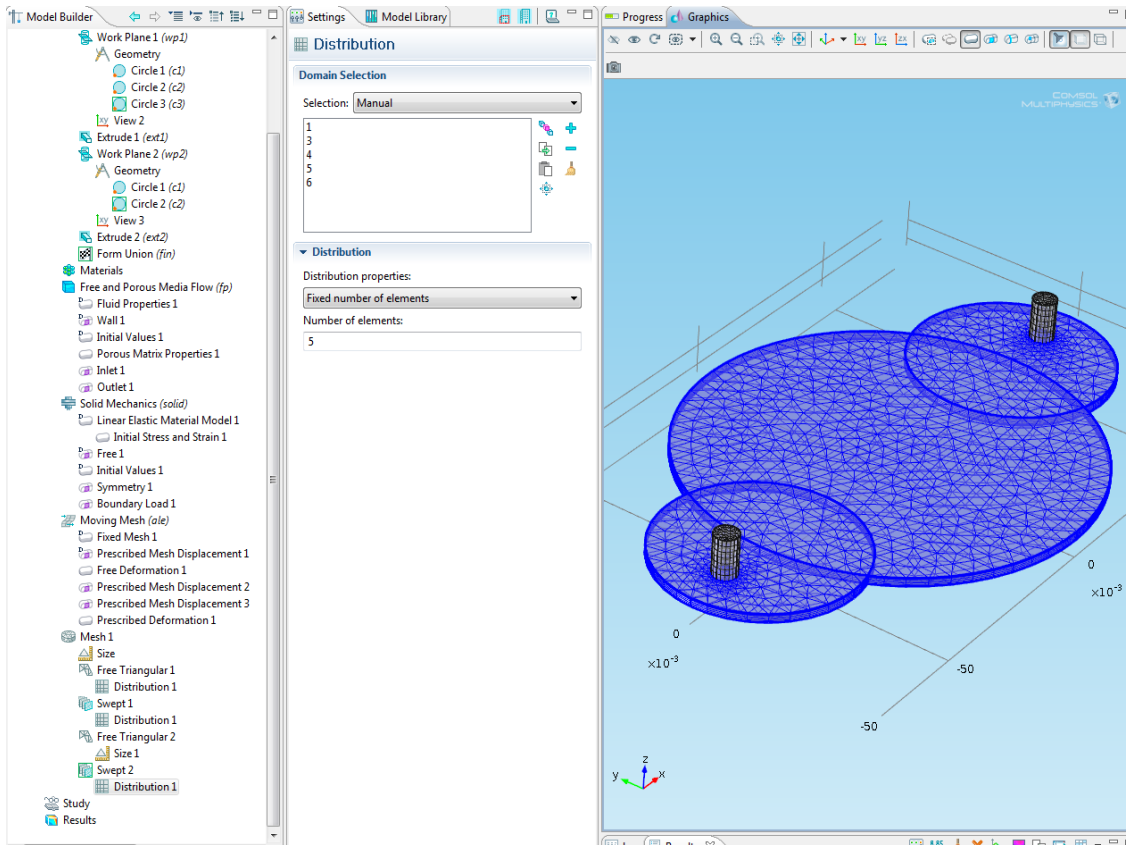
**Note:** The mesh will be swept between the Source Faces and destination Faces

11. Right click **Swept 1** and select **Distribution**.
12. Click **Distribution2**, in **Settings** window under **Selection:** Manual. Click **Paste Selection** button and enter 2,7
13. Under **Distribution** tab, select **Distribution properties:** Fixed number of elements. Enter **Number of elements:** 7.

**Note:** This step will distribute the mesh in 7 horizontal sections.

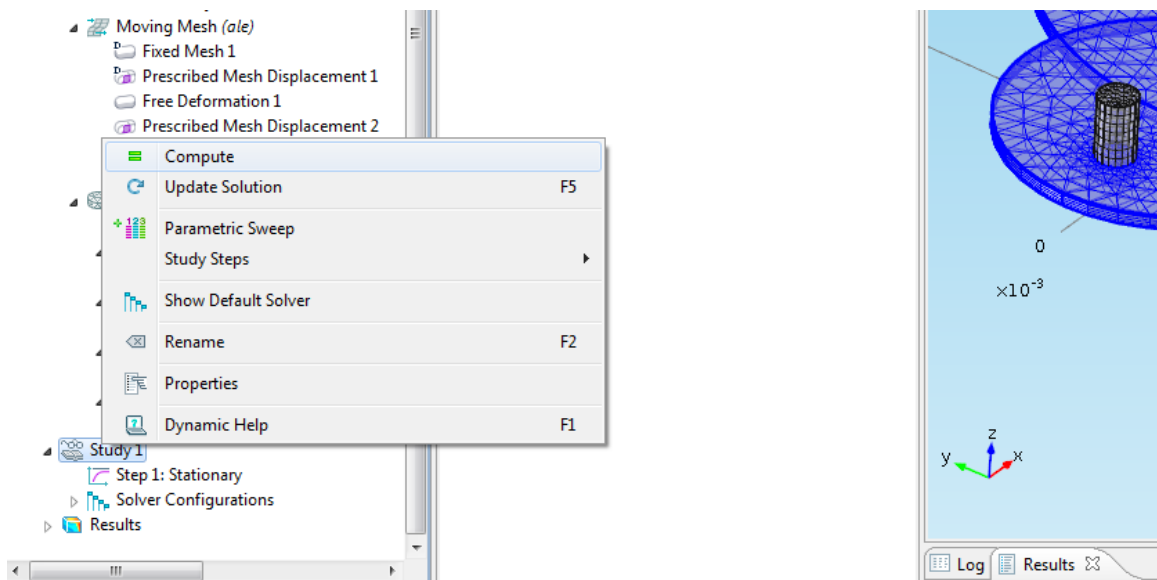
14. Right click **Mesh** and select **More Operations > Free Triangular**.

15. Click **Free Triangular 2**, in **Settings** window select **Geometric entity level**: Boundary and **Selection**: Manual. Click **Paste Selection** button and enter 4,15,20,28,32
16. Right click **Free Triangular 2** and select **Size**.
17. Click **Size 1**, in **Settings** window select **Geometric entity level**: Boundary and **Selection**: Manual. Click **Paste Selection** button and enter 4,15,20,28,32
18. Under **Element Size** tab, select **Calibrate for**: General physics. Select **Predefined**: Extra fine.
19. **Note**: The topmost boundaries of domain other than inlet and outlet are mesh with the extra fine option to produce more node points that regular auto meshing option.
20. Right click **Mesh** and select **Swept**.
21. Click **Swept 2**, in **Settings** window select **Geometric entity level**: Domain and **Selection**: Manual. Click **Paste Selection** button and enter 1,3,4,5,6
22. Under **Source Faces** tab, under **Selections**: Manual. Click **Paste Selection** button and enter 4,7,15,20,28,32,39.
23. Under **Destination Faces** tab, under **Selections**: Manual. Click **Paste Selection** button and enter 3,14,19,27,31.
24. Right click **Swept 2** and select **Distribution**.
25. Click **Distribution 1**, in **Settings** window under **Selection**: Manual. Click **Paste Selection** button and enter 1,3,4,5,6
26. Under **Distribution** tab, select **Distribution properties**: Fixed number of elements. Enter **Number of elements**: 5
27. Click **Build all** button on the **Settings** menu bar.



### Step 8: Setting up Solver and running the simulation using Study

1. Under **Model Builder** window, right click **Study** > **Show Default Solver**.
2. Right click **Study 1** > **Compute** as shown in the figure below.



## Step 9: Obtaining Results and Post Processing

1. Under **Model Builder** window, right click **Results** and select **3D Plot Group**.

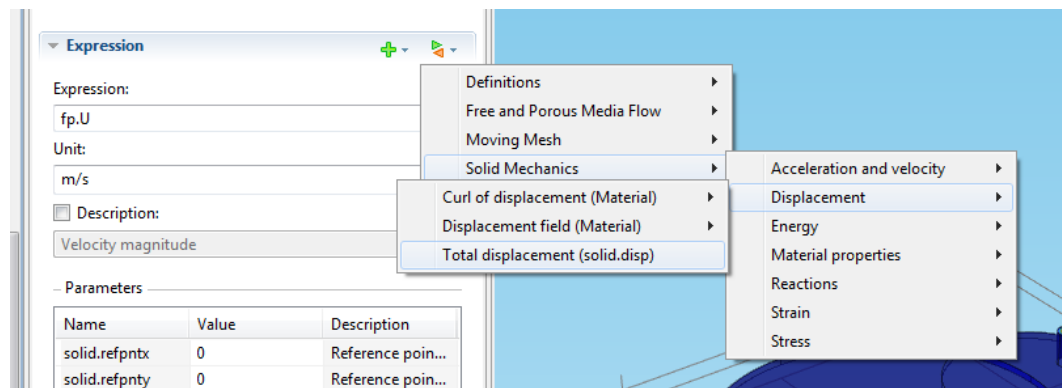
**Note:** Similarly, a 2D plot, line plot, point plot or polar plot can be obtained.

2. Right Click **3D Plot Group 1 > Volume**.

**Note:** Similarly, other plots such as surface, slice can also be obtained under the same or separate plot group. Please explore these options for better understanding.

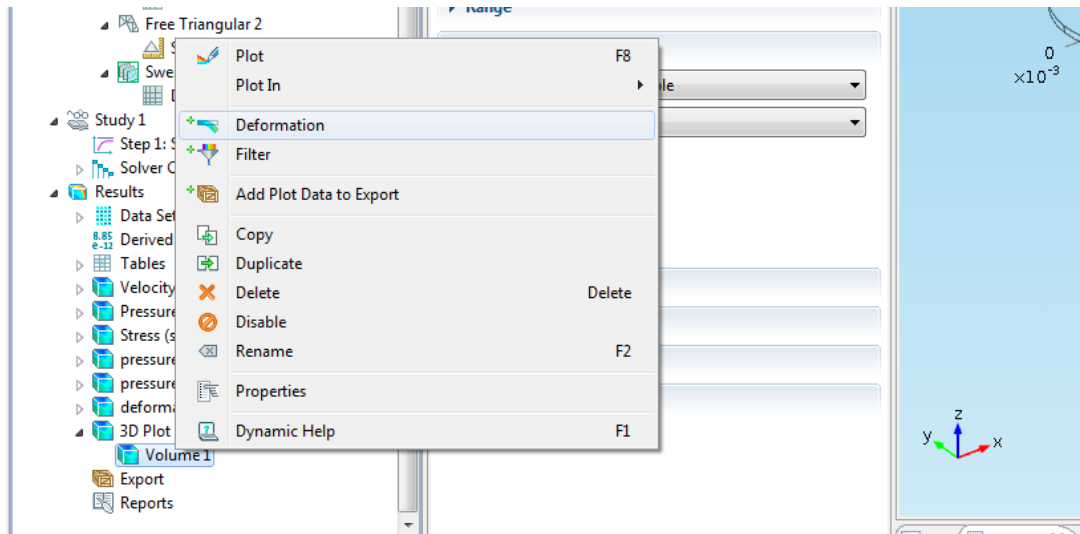
3. Click **Volume 1**, in **Settings** under **Expression** tab click **Replace expression** button >  
**Solid Mechanics > Displacement > Total displacement (solid.disp)**

**Note:** The fluid velocity and pressure expressions are available under the Free and Porous media section in the replace expression button.

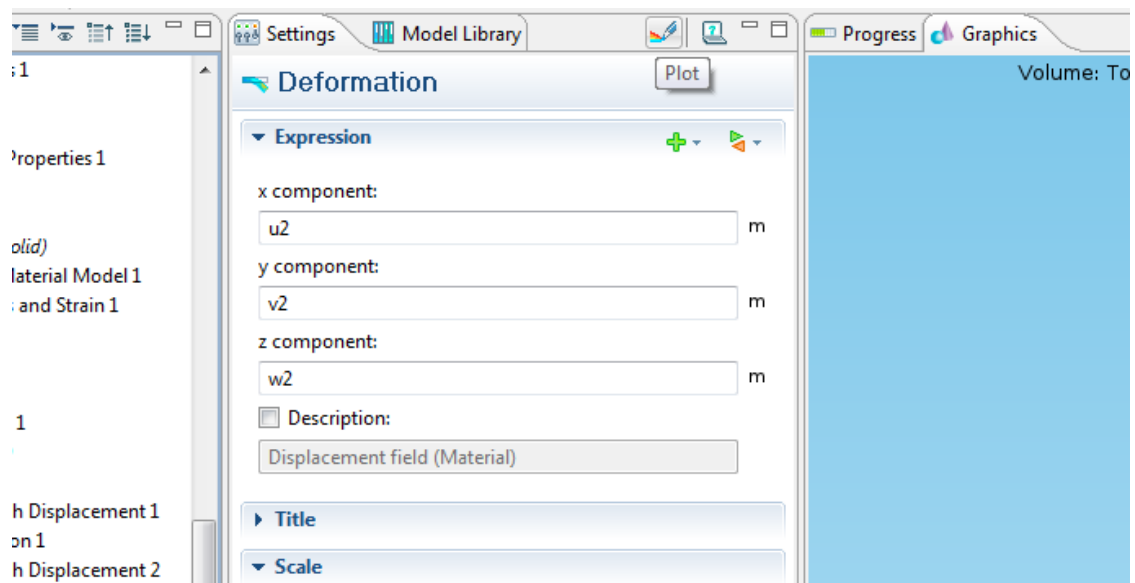


4. Enter **Units:** mm
5. Right **3D Plot Group 1 > Volume** and select **Deformation**.

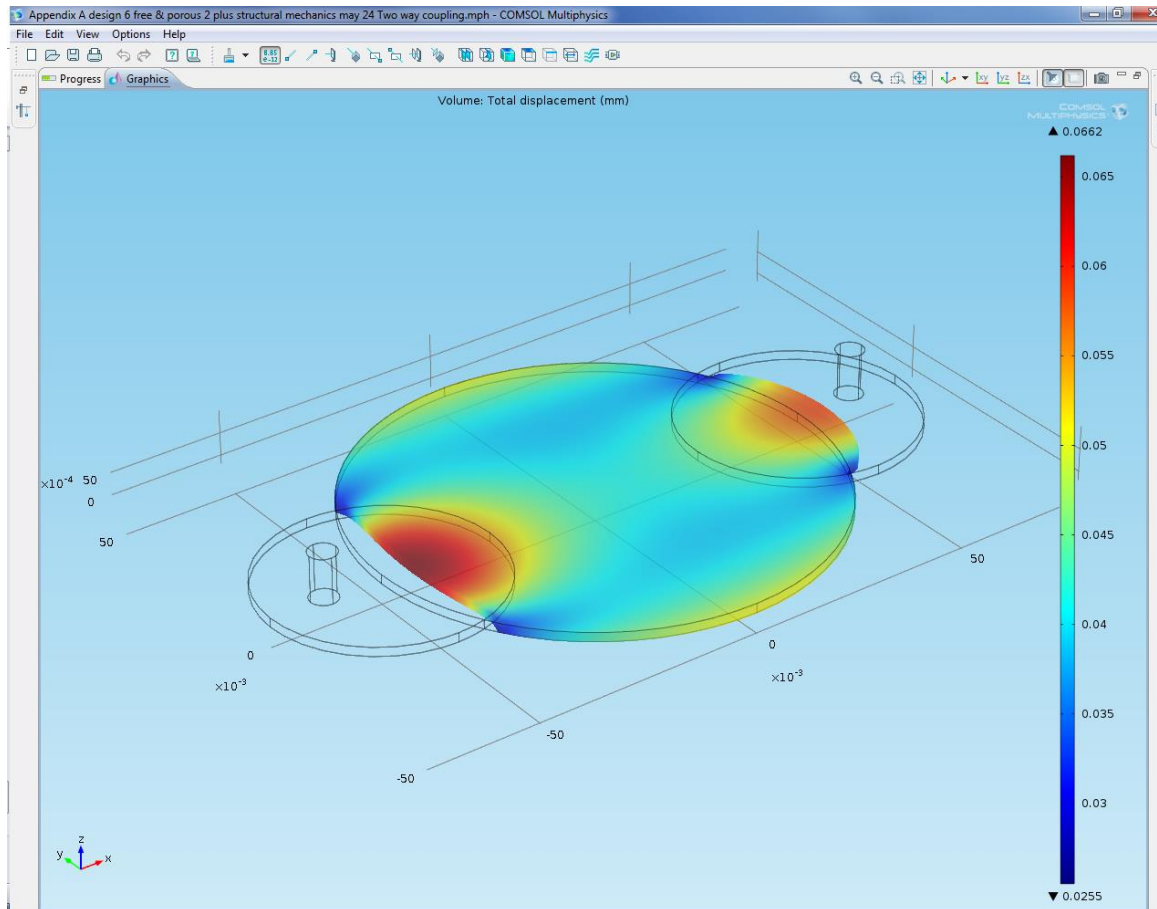
**Note:** This option will include the deformation of the porous domain in the 3D plot.



6. On **Settings** window, click **plot** button as shown in the following figure.



7. Double click **Graphics** tab to expand the **Total displacement (mm)** plot as shown below.



**Step 10: Exporting the plots using the **Export** option**

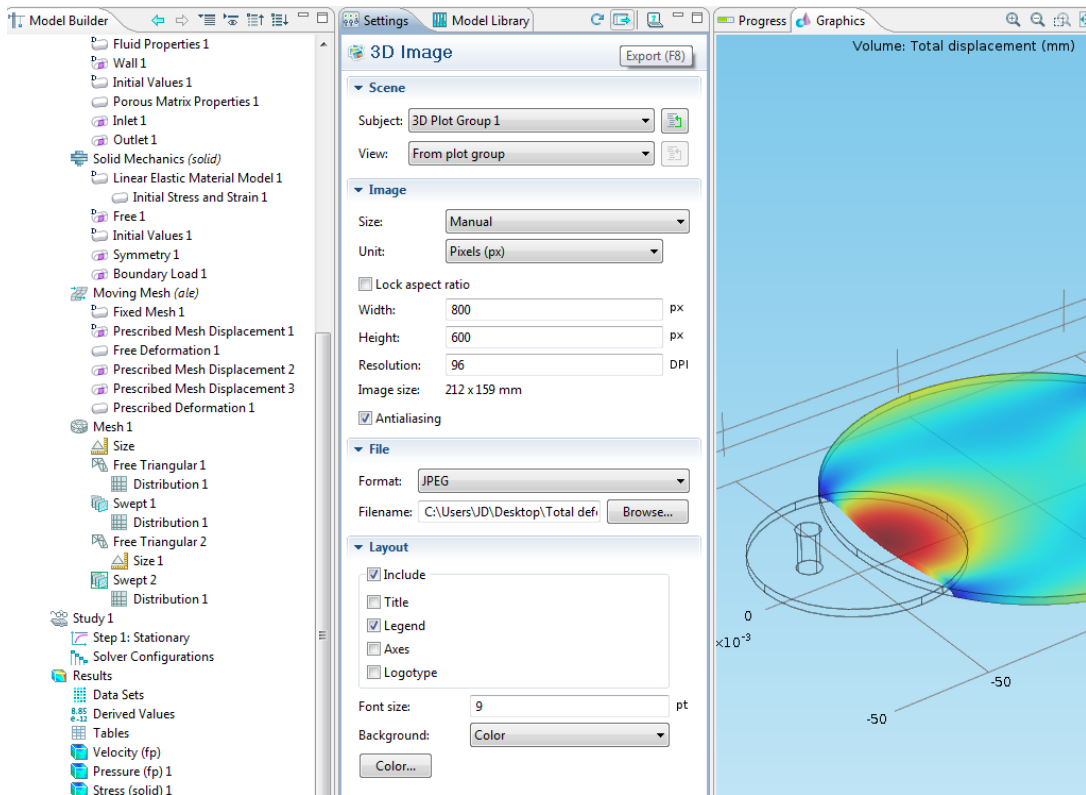
1. Under **Model Builder** window, right click **Results** and select **3D Image**.

Note: Similarly, a 2D or 1D image can be exported.

2. Click **3D Image 1**, in **Settings** window under **Scene** tab, select **Subject: 3D Plot Group**
  - 1.

**Note:** Subject: 3D Plot Group 1 corresponds to the total deformation plot group that was created earlier.

3. Under **File** tab, select **Format: JPEG** and click **Browse**. Enter filename and location.
4. Under **Layout** tab, check **Include** and **Legend**.
5. On **Settings** window, click **Export** button as shown in the figure below.



## References:

[1] COMSOL MULTIPHYSICS, 2011. *COMSOL Multiphysics User's Guide*. Stockholm,

## APPENDIX B

### PRESSURE TRANSDUCER CALIBRATION USING MLA1052 PRESSURE GAUGE AND ACCESSORIES

#### **Calibration of MLT844 Pressure Transducer**

1. In order to calibrate, simply attach the MLT844 Pressure Transducer to one of the valves and then connect the included syringe to the other valve.
2. With the pressure transducer attached to the Bridge Amp and PowerLab, start recording in LabChart.
3. Apply pressure with the syringe so that the pressure gauge reads a certain value, say 20 mmHg, and hold it there until you see a flat line for that signal in the LabChart Software. Record the corresponding voltage reading.
4. Apply pressure with the syringe so that the pressure gauge reads a second value, say 60 mmHg. Again hold the pressure until you see a flat line for that signal in LabChart. Record the corresponding voltage reading.

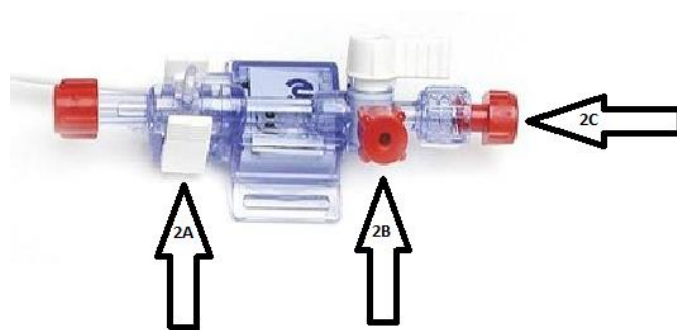
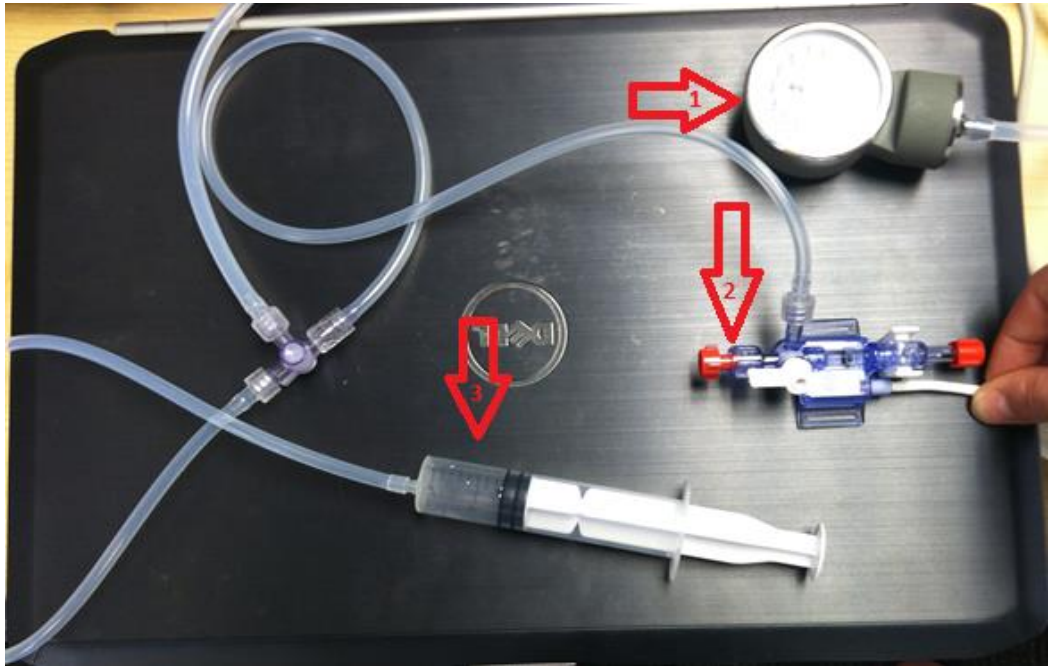
These will be your two values for the two point calibration. To see how the units conversion is setup within the LabChart Software, please see the following link:

[http://dl.dropbox.com/u/1753761/LCM\\_Calibrating\\_Data\\_Units\\_Conversion\\_MultiPoint\\_Calibration.mp4](http://dl.dropbox.com/u/1753761/LCM_Calibrating_Data_Units_Conversion_MultiPoint_Calibration.mp4)



## Calibration of Disposable Blood Pressure Transducers

Below are the transducer, pressure gauge and syringe. Ideally, the system should be calibrated with each use.



### Key:

1: Pressure Gauge

2. Pressure Transducer

2A: Tabs to be compressed to fill dome

2B: Port to connect pressure gauge and to connect the syringe to fill the dome.

2C: Port where PE tubing connects to create catheter for insertion into artery

3. Syringe with saline

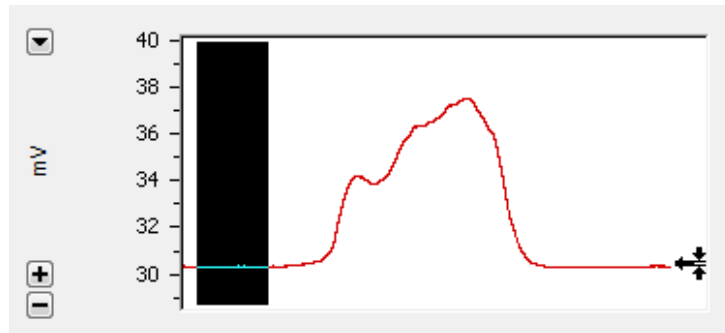
### Steps for Calibration

1. Fill the dome. In order for the pressure transducer to register a change and measure the pressure the fluid filled dome needs to be filled. Use the syringe to inject a small amount of saline into the transducer. Connect the syringe to 2B, compress the tabs (2A) and slowly inject saline until you start to see it pass between the tabs.
2. Replace the syringe at 2B with the tubing of the pressure gauge. Fill the syringe with air, and connect it to the other end of the tubing. Use the stop cock to open 2C to air and close 2B.
3. Open LabChart
4. Open the Amplifier setting through the channel menu and click Zero, and allow the amplifier to zero.
5. Open 2B and start recording in LabChart (this is your 0mmHg signal).
6. Slowly introduce air to the system and inject until the gauge reads the desired pressure (100, 150, 200mmHg) and hold that setting for 1-2 seconds.
7. Stop recording in LabChart.

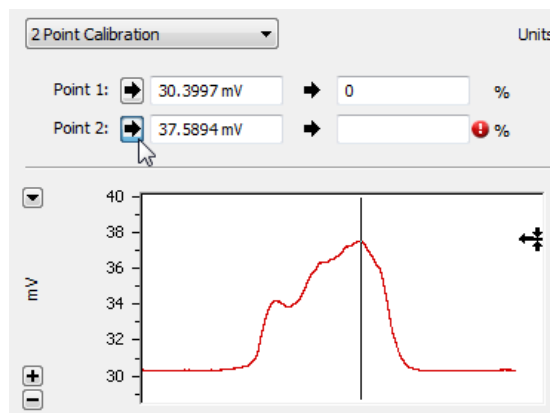
### **Units Conversion**

1. Highlight the data that contains both the zero and max pressure signals.

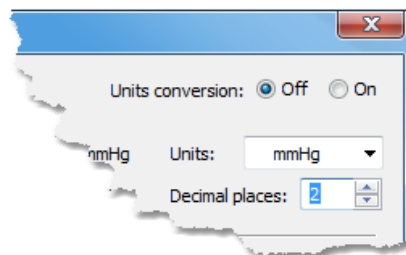
2. Open the channel menu and choose units conversion.
3. Select a region of the zero data, click the arrow for point one and assign this as 0.



4. Select a region of the max pressure data, click the arrow for point 2, and assign this as the max value.



5. Use the drop down menu to assign the unit of mmHg and choose your desired number of decimal places.



6. Click Apply and OK.

You are now ready to record, and your units will be displayed as mmHg.

## APPENDIX C

### 16-730 O<sub>2</sub> MICROELECTRODES CALIBRATION AND OPERATING INSTRUCTIONS

The 16-730 Electrode Kit contains the following:

1 Oxygen Electrode with membrane housing

6 Replaceable membrane housings

1 Bottle of electrolyte

1 Filling tip

1 Set of instructions

5 Polishing pads

#### **Electrode Assembly and Preparation**

1. Remove the acrylic housing from the Oxygen electrode by unscrewing it from the electrode body. This housing, with affixed Teflon membrane, does not contain the necessary oxygen electrolyte solution.
2. Add oxygen electrolyte solution to the acrylic housing. This is accomplished by attaching a filling tip to the bottle of electrolyte and adding the electrolyte to the housing to a minimum height of 6 mm. Gently place the bubble-free end of the filling tip against the Teflon membrane and release the electrolyte to the minimum height.
3. Insert the housing on to the Oxygen electrode, being careful not to trap any air bubbles near the electrode tip. The housing is screwed clockwise into the body of the electrode until it stops. Check the tip of the electrode for proper seating of the housing against the electrode. The electrode is properly seated if the electrode protrudes slightly beyond the end of the housing.

## **Calibration**

Calibration of the electrode requires the use of two standard gases with percent values that are close to the percent values of Oxygen to be measured. Common values used are 0% Oxygen for zeroing and 21% Oxygen (Ambient Air) for sloping or gain. To decrease calibration time, two separate calibration chambers can be used. One for the 0% gas and another for the sloping gas such as 21%. Unplugging the electrode can typically be good for a zero, but the best is to make a sulfite solution (Oxygen Zero Solution). Bubbling air through the water is good for a 21%. When setting up the calibration chambers initially, it will take up to 30 minutes to flush each chamber to obtain a steady state oxygen level and a constant temperature. Again the bubbling rate should be carefully regulated (3 - 6 bubbles per second) so that both calibrating liquids are at the same temperature.

Calibrating standards and samples must be at the same temperature for accurate Oxygen measurements.

1. Immerse the tip of the electrode into the 0% standard and adjust the zero of the meter after a stable reading is obtained.
2. Remove the electrode from the first standard and place it into the second standard. Adjust the calibration control to the value of the second standard (ex: 21%) Alternate between the two standards until you become confident of stability and reproducibility. The electrode is now ready to use.

## **Handling**

When necessary, the membrane of the electrode can be replaced by following the assembly procedure above. When removing and replacing a membrane as well as when calibrating or making measurements, be careful not to apply pressure against the internal electrode. Any excessive pressure against the internal electrode can cause the electrode to crack rendering it useless and unrepeatable.

### **Cleaning**

When using the electrode in solutions containing protein, the electrode should be soaked in an enzyme cleaning solution such as Terg-a-zyme (Alconox, Inc.) after each use for a couple of minutes to remove the protein from the membrane surface. This will prolong the useful life of the membrane.

### **Storage**

*Always clean the microelectrode before storing:*

**Long-term** (over 1 month): Remove the membrane housing from the electrode. Rinse the internal electrode with distilled water and pat dry. Place a new, unfilled membrane housing over the internal electrode and attach loosely (Do not seat completely). This membrane will serve to keep the dust off of the electrode tip.

**Short-term:** The electrode can be left in room air with membrane housing still attached.

### **Output Conversion**

Formula for conversion of percent oxygen to solubility in moles/liter:

$$S = (a/22.414) \times (760-p)/760 \times (r\%/100)$$

Where,

S = solubility of gas in moles per liter

a = absorption coefficient of gas at temperature

P = vapor pressure of water at temperature

r% = actual reading in percent Oxygen

**Temperature (T) vs. absorption coefficient (a) for oxygen in water:**

Degrees Celsius	Absorption Coefficient	Degrees Celsius	Absorption Coefficient
5	0.04287	19	0.03161
6	0.0418	20	0.03102
7	0.0408	21	0.03044
8	0.03983	22	0.02988
9	0.03891	23	0.02934
10	0.03802	24	0.02881
11	0.03718	25	0.02831
12	0.03637	26	0.02783
13	0.03559	27	0.02736
14	0.03486	28	0.02691
15	0.03415	29	0.02649
16	0.03348	30	0.02608
17	0.03283	35	0.0244
18	0.0322	40	0.02306

## VITA

Jagdeep Thribhuvan Podichetty

Candidate for the Degree of

Doctor of Philosophy

Thesis: ESTABLISHING GOVERNING EQUATIONS FOR 3D CELL CULTURE IN  
PERFUSION BIOREACTORS

Major Field: Chemical Engineering

Biographical:

Education:

Completed the requirements for the Doctor of Philosophy in Chemical Engineering at Oklahoma State University, Stillwater, Oklahoma in May, 2014.

Completed the requirements for the Master of Science in Chemical Engineering at Oklahoma State University, Stillwater, Oklahoma in July, 2011.

Completed the requirements for the Bachelor of Technology in Chemical Engineering at Jawaharlal Nehru Technological University, Anantapur, Andhra Pradesh, India in 2009.

Experience:

Research Associate, School of Chemical Engineering, Oklahoma State University, Stillwater, Oklahoma. 2009-2014

Teaching Associate, School of Chemical Engineering, Oklahoma State University, Stillwater, Oklahoma . 2009-2014

Co-founder & Operational Manager, OSU AppCenter, Stillwater, Oklahoma. 2012-2013

Professional Affiliations:

Omega Chi Epsilon Honorary Society

American Institute of Chemical Engineers (AIChE)

Indian Institute of Chemical Engineers (IChE)

Graduate and Professional Student Government Association (GPSGA)

Chemical Engineering Graduate Student Association (ChEGSA)